

Probing properties of dark matter with
Subaru imaging data of massive clusters and
Andromeda Galaxy

銀河団およびアンドロメダ銀河のすばる撮像データによる
ダークマターの性質の検証

Hiroko Niikura
Department of Physics, University of Tokyo

February 3, 2016

Abstract

The current standard model of structure formation, in which the universe is dominated by cold dark matter (CDM) – the so-called Λ CDM model, has been remarkably successful in reproducing various observations such as the cosmic microwave background anisotropies, galaxy clustering and weak gravitational lensing. However, this model assumes that cold dark matter consists about 85% of matter in the Universe, and the nature of dark matter is unknown. The property we know or require is that dark matter interact with ordinary matter only via its gravitational interaction, which plays a dominant role in the hierarchical structure formation. Although a viable candidate of dark matter is unknown, hypothetical elementary particle, the so-called weakly interacting massive particle (WIMP), which might exist beyond the standard model of particle physics, but it hasn't yet been found by any terrestrial experiments such as CDMS and LHC. Hence, revealing the nature and properties of dark matter with astronomical dataset is one of the most important problems in modern cosmology and particle physics.

This thesis shows two testes targeting on dark matter properties. The first part of this thesis focuses on a dark matter property around “Mpc” scales, studying mass profiles of massive galaxy clusters. The mass profile of galaxy clusters is a consequence of the hierarchical structure formation, and has been well studied by N-body simulations baed on Λ CDM model. One of the most important predictions of N-body simulations is that their mass profiles are well described by the so-called Navarro-Frenk-White(NFW) model. The NFW profile predicts “universality” of mass profiles for halos with different masses; the mass profiles of halos over a wide range of mass scales can be well fitted by the same functional form. In this study we proposed a novel method of testing the universality of cluster mass profiles based on the weak lensing measurements for almost volume-limited sample of 50 massive clusters. We combined weak lensing measurements from 50 massive clusters ($z \sim 0.23$) with X-ray mass data, and “scaled” every profiles. We succeeded to detect 4-6sigma detection of universality. In this thesis we summarize mass profile properties of clusters and discuss the implications of our results.

The latter part of this thesis discusses test of nature of dark matter on much smaller, star scales. By fully taking advantage of the wide field-of-view of Hyper Suprime-Cam, which allows us to cover the entire bulge and disk regions of Andromeda Galaxy (M31) with one point, we use the dense cadence data of M31 (about 190 images of 90sec exposure each over about 7 hours) in order to search for microlensing events of stars in M31 due to foreground primordial black holes (PBH). PBH is one of viable candidates of dark matter, and might dominate the dark matter in both the halo regions of Milky Way and M31. We aim at constraining the abundance of PBHs of mass scales, 10^{-9} - $10^{-7}M_{\odot}$, with the dense-cadence HSC data. However, the PBH search requires an exquisite data reduction technique, especially image difference technique in such a dense star region needed to find transient objects (stars). We have extensively used the HSC pipeline to make the data reduction and here report the current status of this project (the results of other transients and the PBH microlensing search).

Contents

Abstract	i
Contents	ii
List of figures	iv
List of tables	xv
1 Introduction	1
1.1 Λ CDM model	1
1.1.1 Basic description of the universe	1
1.1.2 Structure formation	4
1.1.3 Candidates for dark matter	6
1.2 Gravitational lensing	7
1.2.1 Basic properties	7
1.2.2 Observational characteristics	13
1.3 Objective of this thesis	13
2 Universal test of cluster dark matter halos with weak lensing	15
2.1 Introduction	15
2.1.1 Density profile of dark halos	15
2.1.2 Observational implication of clusters	16
2.1.3 Preview of our study	17
2.2 Methodology : stacked weak lensing with NFW scaling	18
2.2.1 Lensing of Navarro-Frenk-White halo	18
2.2.2 Stacked lensing without NFW scaling	20
2.2.3 Stacked lensing with NFW scaling	21
2.2.4 Testing the method with N -body simulations	22
2.3 Results	27
2.3.1 The cluster sample	27
2.3.2 The stacked lensing analysis of 50 clusters with and without NFW scaling	30
2.3.3 Discussion and Implications: Comparison with N-body simulations	37
2.3.4 The halo mass proxy relation of X-ray observables	39
2.3.5 The halo mass and concentration relation	41
2.3.6 The halo mass profile	42
2.3.7 Systematic uncertainty in the lensing measurements	43
2.4 Discussion and summary	43

3	Transient survey of M31	46
3.1	Introduction	46
3.1.1	Magnification property of point source-lens system	46
3.1.2	Preview of our study	49
3.2	Observation and analysis	49
3.2.1	Obsevation	49
3.2.2	Data reduction: single frame processing	51
3.2.3	Data process for transient survey	53
3.3	Results	57
3.3.1	Impacts of different data processing methods	58
3.3.2	Properties of secure candidates	62
3.4	Searching for microlensing events of PBH for cadence M31 observation	65
3.4.1	Basic properties of microlensing events from Massive Compact Halo Objects (MACHOs)	66
3.4.2	Current status: constraint of PBH abundance from HSC M31 data	71
3.4.3	Constraint on abundance of PBHs	79
3.5	Discussion and summary	80
4	Summary and Conclusion	82
	Appendix	84
A	Deflection angle in the spherically symmetric gravitational field	A–85
B	Effects from non-celestial moving bodies	B–88
C	Characteristics of unique events	C–90
C.1	Eclipsing binary stars: white - brown dwarf system	C–90
C.2	A star before nova	C–90
C.3	Appearing star or disappearing star	C–90
C.4	Eclipsing binary	C–92
C.5	Binary stars	C–93
C.6	Cepheid candidates	C–94
C.7	Flares	C–95
C.8	Fake events with common light curves	C–96
D	Other constraints on the abundance of primordial black hole (PBH)	D–97
D.1	Hawking radiation	D–97
D.2	Femtolensing	D–97
D.3	Star formation	D–97
D.4	Neutron stars in globular cluster	D–98
D.5	CMB (WMAP3, FIRAS)	D–98
D.6	Microlensing (MACHO, EROS, Kepler)	D–98

List of Figures

1.1	Gravitational lensing scheme. Orange line describes the light path from the source object (left) to the observer (right), bent around the gravitational field of the lens (middle).	8
1.2	Right figure describes ellipticity of a galaxy with gravitational lensing effect. The innermost circle is the original ellipticity of galaxy, the elongated one is affected by right shear and convergence, and the dashed circle represents the case only with convergence signal. Left figures describes the elongated patterns for different shear properties.	12
2.1	The distribution of NFW lensing profiles for 50 halos for each of which we took the X-ray inferred mass of 50 Subaru clusters (here the hydrostatic equilibrium mass in Table 2.1) and assumed the halo concentration based on the halo mass and concentration relation, $c = c(M_{500c})$, in Diemer & Kravtsov (2014, hereafter DK14). The blue curves are the lensing profiles without “NFW scaling”, and the red curves are the lensing profiles with “NFW scaling”. These profiles are normalized by the best-fit NFW profile to the stacked profile.	23
2.2	Comparison of the best-fit NFW parameters, halo mass and concentration, estimated by fitting the NFW model to the three-dimensional mass density profile (“3D NFW-fit”) or the two-dimensional lensing distortion profile (“2D NFW-fit”), respectively, for the 50 massive halos in N -body simulations of Λ CDM model, respectively	25
2.3	Simulated lensing profiles for 50 massive halos in the N -body simulation (see § 2.2.4 for details). <i>Upper-left panel:</i> The thin curves show the lensing profiles for each of the 50 halos, and the bold black curve is the stacked lensing profile without NFW scaling. The blue curve is the best-fit NFW profile to the stacked profile. We plot these profiles in dimension-less, so that the quantities in the x - and y -axes can be directly compared to other panels; the “scaled” amplitude, $\widehat{\Delta\Sigma}_+ / (2\rho_c r_s)^{\text{bf-NFW}}$, as a function of the “scaled” projected radius, $R/r_s^{\text{bf-NFW}}$, where we used the best-fit NFW parameters of the stacked profile (blue curve). The lower plot in each panel shows the fractional difference of each profile relative to the best-fit NFW profile. The other three panels show the lensing profiles for the same halos when implementing the NFW scaling for each halo or for the stacked analysis (Eq. 2.17). <i>Upper-right panel:</i> The lensing profile when using the NFW parameters of three-dimensional mass profile for each halo, $(M_{500c}^{3D \text{ NFW-fit}}, c_{500c}^{3D \text{ NFW-fit}})$, in the NFW scaling analysis. <i>Lower-left panel:</i> The results when using the NFW parameters of two-dimensional lensing distortion profile, $(M_{500c}^{2D \text{ NFW-fit}}, c_{500c}^{2D \text{ NFW-fit}})$. <i>Lower-right panel:</i> Similar to the upper-right panel, but using the best-fit halo mass of each halo and using the halo concentration inferred from the scaling relation, $c_\Delta = c_\Delta(M_\Delta; z)$ in DK14. In these three panels, the blue curve is not a fit, but the NFW prediction itself, $f^{\text{NFW}}(x)$ (Eq. 2.7). Note that, for all the results, we ignored effects of measurement errors such as intrinsic ellipticities of background galaxies.	26

- 2.4 The 50 clusters used in this work, in the cluster mass (M_{500c}) and redshift plane. The mass estimate of each cluster was taken from Martino et al. (2014) (see also Table 2.1), derived based on the *Chandra* and/or *XMM* X-ray data. The left panel is the mass estimate based on the hydrostatic equilibrium (HSE) assumption, while the right panel shows the results derived using the scaling relation of X-ray gas mass with halo mass (Eq. 2.24), respectively. The errorbars of each cluster are also taken from Martino et al. (2014) (for $M_{\text{gas},500}$ we propagated the errors of gas mass). Comparing the two panels reveals that the same cluster (symbols at the same x -axis value) generally has different mass estimates and errorbars. 28
- 2.5 *Upper panel:* The stacked distortion profile measured from 50 Subaru clusters, based on the standard stacked lensing analysis (Eq. 2.11). We employed the 32 logarithmically-spaced bins over a fixed range of radii, $0.14 \leq R/[h^{-1}\text{Mpc}] < 2.8$, for all the 50 clusters. The errorbar at each bin is computed from Eq. (2.15) assuming that the statistical noise is dominated by the intrinsic ellipticities of background galaxies. The solid curve is the best-fit NFW model, which is specified by the best-fit parameters $M_{500c} = (4.0 \pm 0.1) \times 10^{14} h^{-1} M_{\odot}$ and $c_{500c} = 2.8 \pm 0.3$. For the sake of comparison with the following figures, we plot the distortion profile relative to the best-fit NFW model, as a function of the radius relative to the scale radius of the best-fit NFW model. Note that the representative value of each radial bin is estimated from the average of radii of background galaxies that reside in the annulus (see Eq. 2.14). The reduced chi-square for the best-fit model is $\chi^2/\text{d.o.f} = 22.5/(32 - 2)$. *Lower panel:* Similar to the above panel, but for the 45° -rotated components of background galaxy ellipticities. 30
- 2.6 The expected, differential signal-to-noise ratio, $d(S/N)$, at each of the 8 logarithmically-spaced radial bins in the range $0.14 \leq R/[h^{-1}\text{Mpc}] \leq 2.8$, for each of 50 Subaru clusters. We computed the $d(S/N)$ value as follows. For the expected signal, we used an analytical NFW profile assuming the X-ray HSE mass and the halo concentration inferred from the $c - M$ relation in DK14. To compute the statistical noise in each bin, we used the real Subaru data of background galaxies (their distribution on the sky, the intrinsic shapes and the lensing weights) in each cluster region. This figure suggests that about 79% of 400 data points ($400 = 50 \times 8$), are expected to have the $d(S/N)$ values greater than unity. Note that the representative value of each radial bin is computed from Eq. (2.14) taking into account the radii and weights of background galaxies, which causes variations in the representative values especially for the small radii, even if we work on the fixed range of $0.14 \leq R/[h^{-1}\text{Mpc}] \leq 2.8$ 31
- 2.7 The stacked distortion profile of 50 clusters when implementing the NFW scaling analysis: we summed the “scaled” amplitudes of background galaxy ellipticities in each bin of the “scaled” radii according to the NFW parameters, halo mass and concentration, inferred for each cluster based on its X-ray observables. In the left or right panels, we employed the X-ray inferred mass of each cluster from the hydrostatic equilibrium assumption (HSE) or the gas mass, respectively, and then used the halo concentration inferred from the scaling relation $c = c(M; z)$ in DK14. Note that we used exactly the same background galaxies as those for the analysis without NFW scaling in Figure 2.5. The errorbar at each bin is computed based on Eq. (2.18). The solid curve in each panel is *not* a fit, but the NFW prediction (f^{NFW} given by Eq. 2.7) including a small correction due to reduced shear at the small radii (see below Eq. 2.17). The reduced chi-square is $\chi^2/\text{d.o.f} = 31.3/32$ or $30.7/32$ for the HSE or gas mass case, respectively. 32

- 2.8 The difference between the lensing distortion profiles of 50 clusters and the best-fit NFW profile ($\Delta\Sigma^{\text{best-fit}}(R)$) or the normalized NFW profile ($f^{\text{NFW}}(x)$) for the weak lensing analysis with or without NFW scaling implementation in the left or right panel, respectively. The right panel shows the result when using the gas mass to estimate the halo mass of each cluster. To make a comparison, we show the relative difference to the statistical error at each radial bin (see Eqs. 2.19 and 2.20). Since the lensing profile is noisy on individual cluster basis due to the fewer number of background galaxies, we employed the 8 logarithmically-spaced bins in the fixed range of $0.14 \leq R/[h^{-1}\text{Mpc}] \leq 2.8$ for all the clusters as in Figure 2.6. In addition, we used the same background galaxies in each radial bin before and after the NFW scaling transformation, $x = R/r_s$, for each cluster so that the differences become identical if we set the model NFW profile $\Delta\Sigma^{\text{bf-NFW}} = f^{\text{NFW}} = 0$ (see the procedure 2b in § 2.3.2 for details). Also note that, due to the NFW scaling, the fixed radial range in the left panel is transformed to the different range of the scaled radius for different clusters. The same-color curves in the two panels correspond to the same cluster, and the bold curve shows, as an example, the result for A781, which has the largest deviation from the NFW profile. The sum of squares of all the curves gives an estimate to quantify the scatters of 50 cluster lensing profiles relative to the NFW model – here we call the d^2 value. The NFW scaling yields $d^2 = 527.1$ or 504.6 for the HSE and gas mass cases, respectively, compared to $d^2 = 543.2$ for the case without NFW scaling (Figure 2.5). This corresponds to the improvement $\Delta d^2 = d^2 - d_{\text{w-scaling}}^2 = (4.0)^2$ or $(6.2)^2$, respectively. 33
- 2.9 A test of the performance of the NFW scaling analysis in Figure 2.7. We randomly assigned the X-ray inferred mass to each cluster, redid the scaling analysis, and then computed the d^2 difference (Eq. 2.25), where the d^2 -value quantifies the scatters of 50 cluster lensing profiles relative to the NFW profile as shown in Figure 2.8. The histogram shows the distribution of 200 random realizations, which can be compared to our main result shown by the vertical line for either the HSE mass or the gas mass case in the upper or lower panels, respectively. All the random realizations give a negative value of Δd^2 , and any of those does not reproduce the measurement value. Compared to the mean and variance of the random realizations, the measured Δd^2 value is away from the mean at 3.6 and 3.7σ for the HSE and gas mass cases, respectively. 34
- 2.10 As in the previous figure, but show effects of the statistical errors in X-ray inferred halo mass of each cluster on the Δd^2 value. Here, we added a random scatter to each halo mass by an amount of the quoted errorbar in Table 2.1 assuming the Gaussian distribution, redid the weak lensing analysis with NFW scaling, and then computed the Δd^2 value for each realization. 35
- 2.11 The change in Δd^2 (the vertical axis) when using the different range of radii (the horizontal axis) in the scaling analysis. The bold lines are the results for our fiducial choice: $0.14 \leq R/[h^{-1}\text{Mpc}] \leq 2.8$ and 8 logarithmically-spaced bins for all the 50 clusters. The other lines are the results when excluding the innermost or outermost bin from the analysis, respectively for the the HSE or gas mass proxy cases. 35

- 2.12 Comparison of the measurements and the simulation results for the d^2 -values. (Eqs. 2.19 and 2.20 for their definitions). The bigger-size circle and square symbols are the measurement results for the HSE and gas mass cases, respectively. The other symbols are the simulation results for 40 realizations, combining the N-body halo profiles and the effect of intrinsic ellipticities of background galaxies that are taken from actual Subaru data of each cluster region. The tilted triangle and hexagon symbols are the simulation results; triangles are cases with the best-fit NFW parameters of 3D mass profile for each halo, and the NFW parameters of 2D projected lensing profile. The hexagon symbols are intended to mimic what we did for the actual measurements, using the best-fit mass of 3D profile, and the concentration inferred from the scaling relation $c_\Delta = c_\Delta(M_\Delta; z)$, respectively. (see Figure 2.3 for details). We show the simulation results for 40 realizations of background galaxy ellipticities. Note that, for each realization, we computed the three simulation results; each of the triangle and hexagon symbols with same d^2 value in the horizontal axis, but different $d_{w\text{-scaling}}^2$ values in the vertical axis. For comparison, the orange-color star symbol denotes one particular realization that has a similar d^2 value to the measurement for no NFW scaling case (the vertical axis). The two star symbols in the left-lower corner are the results when using the same realization of background galaxies as in the orange-color star symbol, but using the analytical NFW profiles for the d^2 calculations. Note that the arrow in the lower-left corner denotes the simulation result that is below the plotted range. 38
- 2.13 d^2 plot with the effects of mass scatter of each halo on the simulation results. The hexagon symbols are the same as in Figure 2.12. For each realization of background galaxies, we added a random mass scatter to each halo, simulated the lensing analysis with NFW scaling by treating the shifted mass as the true mass, and then computed the $d_{w\text{-scaling}}^2$ value. Adding the halo mass scatters tends to degrade the NFW scaling results or preferentially causes an up-scatter of each simulation result in this two-dimensional space. *Left panel:* The simulation results when adding the Gaussian mass scatters by the fractional errors of $\sigma_{\ln M} = 0.1, 0.2$ or 0.3 , respectively. The arrows in the upper horizontal axis denote the case that the simulation results are outside the range shown in this plot. *Right panel:* The results when adding a random mass scatter to each simulated cluster assuming the fractional error proportional to the quoted error of the gas mass proxy relation; $\sigma_{\ln M_{(a)}} \equiv \sigma_{M_{(a)}}^X / M_{(a)}^X$ or a factor 2 or 3 bigger one. 39
- 2.14 Effects of variations in the halo mass proxy relation of X-ray gas mass on the NFW scaling results. We model the variations as $M_{500c} / [10^{14} M_\odot] = A \times 11.6 \times (M_{\text{gas}} / 10^{14} h^{-3/2} M_\odot)^\beta$, where $A = 1$ and $\beta = 1$ are our fiducial model corresponding to the self-similar scaling model. We estimated the best-fit parameters (the star symbol) by minimizing the d^2 value with varying the normalization and mass slope parameters. The two contours correspond to the regions satisfying the conditions $\Delta d^2 = d_{w\text{-scaling}}^2(A, \beta) - d_{w\text{-scaling}}^2(A^{\text{best-fit}}, \beta^{\text{best-fit}}) = 2.3$ or 6.17 , respectively. The triangle symbol with error-bar denotes the result when varying the normalization parameter A alone, with fixing $\beta = 1$ 40

2.15	Similar to the previous figure, but effects of variations in the halo mass and concentration relation on the NFW scaling results, for the HSE and gas mass cases, respectively. Here we parametrized the variations as $c(M) \propto M^\alpha$ (Eq. 2.28), and then minimized the d^2 -value with varying the normalization and mass slope parameters. The diamond symbol in each panel shows the parameters for our fiducial model DK14 at the mean redshift of clusters, $z = 0.23$, while the triangle symbol denotes the parameters of Duffy et al. (2008).	40
3.1	An illustration of gravitational lensing system. The light ray emitted from a source is bent by the gravitational field of a lens, and the source can be observed by multiple images due to the lensing. For a system where a star in M31 is a source object and a PBH of $10^{-7}M_\odot$ in either halo region of MW or M31 is a lensing object, the two images due to lensing are not resolved even by the Subaru data, because the angular separation between the two images is about 10^7 arcseconds compared to $O(0.1'')$, a typical angular resolution of the HSC/Subaru data.	47
3.2	Simulated light curves for microlensing events, taken from Fig. 2 of Paczyński (1986). Each light curve stands for different impact parameter u_{\min} at 0.1, 0.2, ..., 1.1, 1.2, and light curve with larger magnification amplitude corresponds to smaller u_{\min} parameter.	48
3.3	The total transmission curve for each broad-band filter of the Subaru/Hyper Suprime-Cam system. Each curve takes into accounts the transmission of each filter, quantum efficiency of fully depleted CCDs, transmittance of the dewar window, transmittance of the Primary Focus Unit of the HSC (POpt2), and reflectivity of the Primary Mirror.	50
3.4	Characteristics of our HSC M31 observation. Left panel shows the time-variation of altitude of target field (M31) during observation. Our observation started from 18:33:59 on November 24 2014, and ended at 1:35:34 when the altitude gets lower than 30 degrees. Right panel shows the seeing of each exposure. We conducted the “focusing” (determined the focus position of the camera) three times during the night, 19:50:33, 22:37:02, and 0:37:07.	51
3.5	An example of our exposure image of the M31 region. Left panel displays one raw image taken by Hyper Suprime-Cam. Each rectangle-shape sub region, enclosed by black-color gap, corresponds to a single CCD chip. Right panel shows one example of reduced image, the one later called as reference image in z-scale (The detail of this image is described in § 3.2.3). This figure is in a unit called “tract”, composed of sub-regions called “patches” (displayed as different-color rectangular regions in this figure).	53
3.6	An example of the image subtraction of the two images. Here we show the image taken from the 1/60 region of patch=2.6, which is in between the disk and halo regions; the size of image is $25''$ for the horizontal width. <i>Upper left</i> : one example of reduced image of single-visit frame. <i>Upper right</i> : the “reference image” generated by combining or coadding the 10 best-seeing exposures among the 194 exposures. <i>Lower left</i> : the difference image obtained by subtracting the target image, which is constructed by coadding the 5 time-sequential images, from the reference image. Almost all the stars, except for a saturated, bright stars, are cleanly subtracted. Our default analysis for transient search uses the target images of 5 time-sequential coadds for other patches. Photometry of transient candidate object is performed on the difference image. <i>Lower right</i> : for comparison, the difference image when subtracting the single exposure from the reference image. For this case, there are cosmic rays in the image.	55

3.7	<p>Summary of § 3.2.3, describing the image difference method in our survey. Upper panel shows the way reference image is constructed; simply by stacking the best-seeing 10 frames. Note that these frames are concentrated on the period around $\sim 11,000$ sec from the observation start; in other words, some of the 10 exposures are not time-sequential. Lower panel shows the way of generating target images to be compared with the reference image. We coadded 5 time-sequential exposures to generate each target image, where each object has an improved signal-to-noise ratio and cosmic rays are more cleanly removed.</p>	56
3.8	<p>Examples of transient candidates that are excluded by our conditions to select a point (PSF-like) source transient in the difference image. The 4 postage-stamp images in each panel show the reference image (the coadd image of the 10 best-seeing images), target image (the coadd image of 5 time-sequential images), the difference image and the residual image after subtracting the best-fit PSF image, from left to right, for each fake candidate. Upper panel shows a typical example of fake candidates that are excluded by the condition <code>maxSizeRatio</code> (the image looks smaller than the size of PSF at the image position). Upper right panel shows a typical example of fake candidates that are excluded by the condition <code>maxSizeRatio</code> (the image looks larger than the PSF size). Lower left panel displays an example of fake candidates that are excluded by the condition <code>limAxisRatio</code> (the shape of the image appears inconsistent with the PSF shape, although the size looks consistent with the PSF size). Lower right panel displays an example of fake candidates that are excluded by the condition <code>maxResidual</code> (the residual image looks too large).</p>	57
3.9	<p>An example of the light curve of a secure time-variable point source candidate. We made a photometry of the candidate in a dense star region, where multiple stars can be in a CCD pixel. We first find a secure candidate from the image difference comparing the reference image and the target image, as we described in Sec. 3.2.3. We then make the PSF photometry at the same WCS position of the found candidate in each of the 194 difference images. Note that the PSF counts in the difference image can be negative, if the candidate gets fainter compared to that in the reference image. Then we add the PSF magnitude counts to the PSF magnitude at the same WCS position in the reference image in order to estimate the total flux of the candidate at the time of the target image. Note that the reference image is mostly from the best-seeing exposures at $t \sim 10000$ sec. For comparison, the right panels shows the light curve of the candidate if we use the PSF magnitude at the same WCS position of the candidate using each of the target image, rather than using the difference image. The shape of the light curve appears similar to time variation of seeing size in Fig. 3.4, reflecting that the estimated PSF magnitude is overestimated for the image with larger PSF size due to contamination from the surrounding stars in the image.</p>	58

3.10	An schematic illustration of our photometry measurement of time-variable point-like source in the dense star region of M31. We made use of the difference image in the target image rather than using the original image. The left image is a postage-stamp image around a secure time-variable star candidate in the reference image. Then, the middle image shows the difference image for the target image. We make the PSF photometry on the difference image at the same WCS position of the candidate. The upper image show the case that the candidate in the target image appears fainter than that in the reference image, while the lower image shows the case that the candidate appears brighter than that in the reference image. By adding the PSF magnitudes in the reference image and the difference image of the target exposure, we estimate the PSF magnitude of the target image as given in the right panels.	58
3.11	Comparison of the two images reduced by using different background subtraction methods. Left panel shows an example of the difference image using the 6th order polynomial fitting for background estimation, as in the lower right panel of Fig. 3.6. Right figure shows an example of the difference image using the spline fitting method for the 64 meshes in each CCD chip (default method). This image shows a residual pattern of the background field, which causes an inaccuracy in the photometry of time-variable star candidates.	59
3.12	Distribution of variable star candidates across the M31 region covered by 104 CCD chips. The right panel shows the distribution of variable candidates obtained when using the spline fitting method for background subtraction in each CCD chips (the default method of HSC pipeline). For this case we found about 1500 candidates in total. The different color symbols are different types of variable candidates classified based on their light curves. Left panels displays the distribution of variable candidates obtained by using the 6 or 10-th order polynomial fitting method for each CCD chip (see text for details). For this case, we found about 11,000 candidates. For a particularly dense star region such as the bulge region or NGC205 region, our data processing method cannot properly work, and we cannot properly find candidates of variable stars in these regions. . . .	60
3.13	Effects of residual background uncertainty in the difference image on the PFS photometry of a time-variable candidate. The left and right panels show the postage-stamp image around the same time-variable candidate: from left to right in each panel, the reference image, the target image, the difference image and the residual image after subtracting the fitted PSF image from the difference image. In the right panel, we found a residual background counts in the difference image. Due to this residual background, the PSF photometry doesn't work, and the rightmost image shows a residual image after subtracting the fitted PSF image. Left panel shows that the PSF photometry can work if the median background in the 41×41 region around the candidate is subtracted before the PSF photometry.	61
3.14	A typical example of a fake candidate whose light curve (upper panel) has a clear correlation with the seeing variation (lower panel). The light curve has a sharp feature when the seeing size has a sudden change.	61

3.15	Examples of the light curves for different types of variable star candidates, as described in § 3.3.2. The panels in the left column, from top to bottom, show candidates of eclipse binary system, Cepheid variable star, moving object in the Solar system, and deflection spikes. Similarly, the panels in the right column show candidates of binary star system, star flare, a star near to CCD chip edge, and RR-Lyrae variable star. Left column shows candidates of eclipsing binary stars, Cepheid variable star, moving object in the Solar System, and magnification due to mirroring spikes; while right column displays candidates of binary star, flare star, star close to CCD edge, and candidate of RR-Lyrae variable star, from top to bottom. More details and examples are described in Appendix Band C.	63
3.16	Event classification from color and magnitude implications. <i>Upper panels:</i> candidates categorized by $g-r$ color conditions; each star-type category is calculated by combining HSC filter model as displayed in Fig. 3.3 and stellar spectrum of Kurucz air model (here we adopt solar type stars of Kurucz 1993). Note that we only take into account temperature information for stellar-type classifications. Left panel shows all candidates, and right panel excludes stars with low temperature. <i>Lower panels:</i> candidate distribution classified by r -band magnitude in the reference image. Left panel shows all candidates, and right panel shows only those brighter than 23 magnitude.	66
3.17	The systems describing gravitational microlensing effect. Left figure shows a case when a source star enters the Einstein radius of a lens star. Right figure describes the simplified system of Fig. 3.1; light from source object are bent to form multiple images, but their separation is too small to be resolved for us.	67
3.18	Left panel: Mass density profile as a function of distance from the Earth (an observer) in the direction to M31. We assume that the Earth is at 8.5 kpc from the MW center. We assume NFW profiles for the mass density profiles either of which is consistent with the observed rotation curve of MW or M31 as proposed in Klypin et al. (2002). The mass density profile is given by a superposition of the two NFW profiles. Right panel: The differential optical depth of microlensing due to PBH of mass $10^{-7}M_{\odot}$ at the distance $x D_S$ [kpc] ($D_S = 770$ [kpc], $0 < x < 1$) from an observer, for a star in M31. Here we assumed that the mass in the MW and M31 halo regions is fully composed of PBH.	68
3.19	The differential event rate of microlensing due to PBHs, per unit observation time (hour), per a single star in M31, and per unit time scale of microlensing (hour). The x-axis is the timescale of microlensing. Here the mass distribution of MW or M31 halo region is given by the NFW profile, all the dark matter is made of PBHs, and we considered PBHs with mass $10^{-9}, 10^{-8}$ or $10^{-7}M_{\odot}$, respectively. The lighter PBH has a shorter microlensing time scale. Right panel shows the relative contribution to the microlensing rate due to PBHs in either MW or M31 halo region.	70
3.20	An estimation of noise variance in the difference image. Here we show the results for the difference image of patch=2,6 as an example. We randomly select 1000 points in a blank region of the difference image (as shown in the right panel), measure the PSF magnitude of each point and then estimate the variance of PSF magnitude. The left panels shows the noise variance, 1, 3 or 5sigma, as a function of observation time. The square symbols show the results when using the coadd images of 5 time-sequential exposures for the difference image. The circle symbols, connected by the line, are the results for each exposure. The difference in the upper and lower plots, in the left panel, is with or without the median background subtraction of the difference image.	72

3.21	Uncertainty of star flux in our data. Left panel shows PSF magnitude errors of each star. The star samples are constructed from the star catalog of the targeting field (the detail of catalog property is described in § 3.4.2). Right panel displays the PSF flux error in the unit of ADU for the same star samples of 90 sec exposure. The red line corresponds to the border line that flux error is above or under 0.34 times of PSF flux, which indicates that stars with PSF flux larger than the line can overcome the magnification condition: $A > 1.34$. The error distribution indicates that stars with PSF flux $\sim 0.6[\text{ADU}]$ at 90 sec exposure, corresponding to stars brighter than 25.8 mag can barely probe $A > 1.34$ magnification.	73
3.22	One example of simulated light curve of a microlensing event in the difference image. Red points indicates the simulated light curve, taking into account the flux noise at an assume position in the difference image at a given time. Smooth blue points is the fitting curve of the simulated light curve, and faint blue lines in the background represents the 3σ noise threshold.	74
3.23	The detection efficiency estimated from light curve simulations taking into account the noise field in each difference image of 194 target images we used for the analysis (see text for details). Here we generated Monte Carlo simulations of microlensing events randomly varying the two parameters: the impact parameter (or maximum lensing magnification) and the FWHM time scale parameter, for source stars of a fixed magnitude as indicated by legend. The x-axis is the microlensing time scale. The detection efficiency for each source magnitude is estimated from 1,000 realizations.	74
3.24	The distribution of microlensing parameters for source stars with 24 magnitude. Each point is derived by the fitting of a simulated light curve. We tested 400 events for every event with different time scale. Here we perform the fitting with two parameters; impact parameter β and timescale parameter t_{FWHM} , and the maximum time of the event t_{max} is fixed at the time of maximum flux.	75
3.25	Comparison of detection efficiency from different tests, focusing on the results from stars with 22 and 24 magnitude (All the error-bars come from Poisson noise). Small circles show the results from light curve simulations (the same as shown in Fig. 3.23), and large marks represent the results from fake image simulations, where we inject fake point source in the real image and performed the same analysis of microlensing search.	76
3.26	The number counts of stars in some patch regions of M31. Here we employ 0.1 mag for the magnitude binning, and considered two different catalogs of stars. The blue histogram shows the number counts for stars that are identified by the HSC pipeline based on the imposed conditions. The green histogram shows the number counts for "peaks" that are identified from local peaks in the flux field in each image. Left panel is from M31-halo region (patch=1,5), middle panel is from halo-disk region corresponding to the targeting field in this section (patch=2,6), and right panel is from bulge region (patch=4,4).	77

3.27	Flux and peak number counts distributions of HSC-M31 region. The rectangles in each map show analyzed regions: blue rectangle is M31-halo region (patch=1,5), cyan one is halo-disk region corresponding to the targeting field in this section (patch=2,6), green one is disk region (patch=3,8), and red one is from bulge region (patch=4,4). Both panels are plotted with linear color scales; white side of the bottom color bars means larger and black means smaller. Left panel shows the distribution of the average flux counts in the unit of patch, suggesting the existence of very bright patches around M31 bulge and NGC205. Right panel shows the distribution of the number density of peaks. The number counts of peaks is smaller for disk and bulge regions, which is inconsistent with higher pixel counts compared to halo region.	77
3.28	Color-magnitude diagram for three regions constructed from star catalog: halo region (patch=1,5), targeting region in-between halo and disk (patch=2,6), and bulge region (patch=4,4) from left to right. Red giants in M31 are expected to show up around $g_0 \sim 25\text{mag}$ and $(g - r) \sim 1.0$ region (corresponding to yellow box; red giants in MW is expected in blue-box region). However, we cannot study the expected clumpy property due to the failure in the debrending process of <i>multiband.py</i> program, which prevent the statistical study of the stars.	78
3.29	Expected number of microlensing events for source stars in the patch=2,6 region, as a function of PBH mass in the horizontal axis. The right panel shows an upper limit on the abundance of PBHs assuming we don't have any secure candidate of PBH microlensing (no detection). To convert no detection to the upper limit, we assumed that some portion of dark matter in the halos regions of MW and M31 is made of PBHs, parameterized by $\Omega_{\text{PBH}}/\Omega_{\text{DM}}$ in the vertical axis.	79
3.30	Summary of upper bound on the abundance of PBH, as its contribution to dark matter, in comparison with other constraints (Capela et al. 2013a). The orange line is the upper limit obtained from this thesis work using the 4 patch fields as used in Fig. 3.27. The red dashed line is the constraint if using all the data of M31 (very preliminary) and assuming no detection of PBH microlensing.	80
A.1	A simple schematic representation of gravitational lensing effect describing the deflection of light path around massive object.	A-86
B.1	The effect from diffraction spikes. Left panel shows one part of difference image containing spike patterns. Spikes are often seen in brighter stars, and the patterns turn clockwise during the observation. Right panel displays an example of light curve affected by spikes of a nearby star. Peak around $\sim 13000\text{sec}$ is caused by a spike.	B-89
B.2	Examples of moving candidates; Left panel shows an example of CCD-edge move during HSC-M31 observation. The green region corresponds to region outside a CCD chip, and red circle draws the trace of the edge. Middle panel displays one example of light curve affected by CCD defects. Peak around $\sim 9000\text{sec}$ is caused by the defect part. Right panel shows one example of moving candidate of celestial object. Unlike the other two images this object draws a straight motion path.	B-89
C.1	Eclipsing binary stars consisted of a white dwarf (WD) and a brown dwarf (BD). Left panel displays pictures of WD-BD system; showing time variation from left to right. Right panel gives the light curve of the same eclipsing-binary system, containing very deep dips with length around 10 minutes.	C-91

C.2	Left figure shows the light curve of nova candidate which contains very faint magnification. For comparison, right figure shows a typical example of light curve for a star without magnification.	C-91
C.3	Light curves for appearing and disappearing stars.	C-91
C.4	Light curves of eclipsing binary-star candidates.	C-92
C.5	Light curves of binary-star candidates.	C-93
C.6	Light curves of cepheid variable-star candidates.	C-94
C.7	Light curves of flare-star candidates.	C-95
C.8	Light curves of fake candidates which might contain RR-Lyrae variables.	C-96

List of Tables

2.1	X-ray and Lensing Observables of 50 Clusters	45
3.1	Properties of flux count and star number counts for sub-regions of HSC-M31 . . .	78

Chapter 1

Introduction

1.1 Λ CDM model

1.1.1 Basic description of the universe

Recent development of cosmological observation and numerical simulations supports the picture that the universe is hierarchically formed. The matter distribution in the universe is homogeneous and isotropic. This assumption is called as cosmological principal. In this section, we briefly review basic equations of the expanding universe and structure formation.

(1) Friedmann equation

We start with the spacial properties of the universe assuming the cosmological principal. Here the dynamics of the universe in space-time dimensions follows the Robertson-Walker metric (Robertson 1935; Walker 1936):

$$ds^2 = -c^2 dt^2 + a^2(t) \left\{ \frac{dr^2}{1 - Kr^2} + r^2(d\theta^2 + \sin^2\theta d\phi^2) \right\}, \quad (1.1)$$

where K is spatial curvature, and $a(t)$ is scale factor. Scale factor is an indicator of cosmological distance, and closely related to another conventional description of the distance; the redshift. The redshift is a distance estimator described by the observed wavelength λ_0 and the original wavelength λ_s as $z = (\lambda_0 - \lambda_s)/\lambda_s$. The connection in-between the redshift and scale factor is $a = 1/(1 + z)$, where the current scale factor is defined as $a_0 = 1$.

Photons that are emitted from a source at redshift z_s and are observed by an observer at the coordinate origin propagate along the geodesic specified by $ds^2 = 0$ with $d\theta = d\phi = 0$. Then we can introduce the distance to $x_c(z)$ as comoving distance:

$$\int_0^{x_c(z)} \frac{dr}{\sqrt{1 - Kr^2}} = \int_{t(z)}^{t_0} \frac{cdt}{a(t)} \quad (1.2)$$

where $t(z)$ denotes the time when the light is emitted, and t_0 is the present time. Thus the radial distance is given as:

$$r(\chi) = \begin{cases} \sinh(\sqrt{K}\chi)/\sqrt{K} & K > 0 \\ \chi & K = 0 \\ \sinh(\sqrt{-K}\chi)/\sqrt{-K} & K < 0 \end{cases} \quad (1.3)$$

Therefore spatial curvature represents the shape of the universe; $K > 0$ is open, $K = 0$ is flat, and $K < 0$ is closed universe respectively.

Another set of equations that are essential for the dynamics description is Einstein equation. Einstein equations of the FRW metric describes how the universe expands as a function of time and how the expansion rate is related to the matter-energy contents.

$$G_{\mu\nu} = R_{\mu\nu} - \left(\frac{1}{2}R - \Lambda\right)g_{\mu\nu} = \frac{8\pi G}{c^4}T_{\mu\nu} \quad (1.4)$$

In the case with perfect fluid under with the Robertson-Walker metric, the energy-momentum tensor in the right hand side of Eq. (1.4) is given by:

$$T_{\mu\nu} = (\rho + p)u_\mu u_\nu + pg_{\mu\nu} \quad (1.5)$$

where $u_{\mu\nu} = (1, 0, 0, 0)$ stands for the velocity components, ρ for the density, and p for the pressure of the universe, respectively. With Eq. (1.1) and Eq. (1.5), we can derive the time-time component and the space-space component as:

$$\left(\frac{\dot{a}}{a}\right)^2 + \frac{c^2 K}{a^2} = \frac{8\pi G}{3c^2}\rho + \frac{c^2 \Lambda}{3} \quad (1.6)$$

$$\frac{\ddot{a}}{a} = -\frac{4\pi G}{3c^2}(\rho + 3p) + \frac{c^2 \Lambda}{3} \quad (1.7)$$

where the dot notation denotes the time derivative, and ρ and p denote the total energy density and pressure, respectively. Combining these Friedmann equations with the following equation of state:

$$p = wp \quad (1.8)$$

characterizes the time evolution of the energy density. The w parameter takes specific values for different components; $1/3$ for relativistic component, whereas $w = 0$ for non-relativistic particles such as dark matter. Therefore Eq. (1.6), Eq. (1.7), and Eq. (1.8) describe:

$$\rho \propto \exp\left(-3 \int \frac{da'}{a'}(1+w)\right) \quad (1.9)$$

Note that Eq. (1.9) gives the time evolution of density components; $\rho_m \propto a^{-3}$ and $\rho_\gamma \propto a^{-4}$, for example.

In modern cosmology the density evolution of the universe is often characterized by cosmological parameters as follows:

$$H \equiv \dot{a}/a \quad : \text{Hubble parameter}, \quad (1.10)$$

$$\Omega \equiv \rho/\rho_{\text{crit}} \equiv 8\pi G\rho/3H^2 \quad : \text{density parameter}, \quad (1.11)$$

$$\Omega_K \equiv c^2 K/a^2 H^2 \quad : \text{curvature parameter}, \quad (1.12)$$

$$\Omega_\Lambda \equiv c^2 \Lambda/3H^2 \quad : \text{dimensionless cosmological constant}, \quad (1.13)$$

With these quantities the density evolution in Eq. (1.6) can be characterized as:

$$H^2(a) = H_0^2 \left[\frac{\Omega_{m0}}{a^3} + \frac{\Omega_{\gamma 0}}{a^4} - \frac{\Omega_{K0}}{a^2} + \Omega_{\Lambda 0} \exp\left\{-3 \int \frac{da'}{a'}(1+w_{\text{DE}}(a'))\right\} \right] \quad (1.14)$$

where $w_{\text{DE}} = p_\Lambda/\rho_\Lambda$, and parameters with index 0 in the right hand side of Eq. (1.14) represent current density contents.

(2) The observational review of cosmological component

As mentioned in previous section, the density evolution in the Robertson-Walker metric universe can be characterized by the density component of the universe. Thus observational constraint on the density component plays a key role to probe the evolution of the universe. In this subsection we briefly summarize some properties that support Λ CDM model.

a) *Baryonic component*

Baryonic component has began to be formed a few minutes after Big Bang. At the beginning particles stay in very hot period and stay in equilibrium. When the expansion timescale become shorter than the nuclear interaction timescale, the abundance experiences “freeze out”, and elements are begun to form. By comparing the primordial abundance for the light element from simulation and observation, we can know about the baryonic component. Especially the measurement of primordial deuterium abundance pins down extremely accurately. For O’Meara et al. (2001) provides $D/H = 3.0 \pm 0.4 \times 10^{-5}$, corresponding to $\Omega_b h^2 = 0.0205 \pm 0.0018$.

b) *Flatness*

The cosmic microwave blackbody (CMB) radiation offers the universe when photons last scattered off electrons at $z \sim 1100$. The temperature spectrum is isotropic, corresponding to blackbody spectrum around $T = 2.728\text{K}$ (Penzias & Wilson 1965). Despite the isotropy there exists small anisotropy which represents tiny density of order 10^{-5} (Smoot et al. 1992). This temperature fluctuation pattern of CMB is characterized by the angular power spectrum C_l defined as:

$$\frac{\Delta T}{T} = \sum_{lm} a_{lm} Y_l^m, \quad (1.15)$$

$$C_l \equiv \langle |a_{lm}^2| \rangle \quad (1.16)$$

where C_l is the ensemble average of the coefficient of the multipole expansion of the temperature fluctuations. CMB observation such as Planck collaboration strongly constrains the spatial curvature of the universe, indicating that the universe is almost flat, $\Omega_M + \Omega_\Lambda \sim 1$.

c) *Acceleration*

The cosmic expansion history can be investigated from distance indicators. One popular indicator is Type-Ia supernova, which has constant peak luminosity in absolute magnitude. Thus we can derive the relation between the luminosity distance to test whether the universe is decelerating or accelerating. Observation of type-Ia supernova, combined with CMB observations, strongly indicate the universe with $\Omega_M \sim 0.3$ and $\Omega_\Lambda \sim 0.7$. This result supports that the universe is accelerating (Riess et al. 1998; Perlmutter et al. 1999).

Another popular distance indicator is baryonic acoustic oscillation (BAO), which is acoustic peak probed in the galaxy correlation function on redshift dependence. BAO is precisely measured in several redshifts such as in the galaxy survey of Sloan Digital Sky Survey (SDSS)¹. Combined results from Type-Ia supernovae and BAO strongly limit the abundance of cosmic density components.

¹<http://www.sdss.org>

1.1.2 Structure formation

The universe with Robertson-Walker metric describes the properties of isotropic and homogeneous expansion. On the other hand, current universe contains various structures such as galaxies, clusters of galaxies, super clusters, filaments and voids, whose formation need other scenario of structure evolution. These structures are now believed to arise from gravitational amplification of tiny seed density fluctuations as observed in the CMB anisotropies. In this section we describe the fluctuation evolution in the Λ CDM universe.

(1) Density evolution in Linear perturbation theory

Here we consider the mass fluctuations at scale larger than a few Mpc, where the amplitude can be approximated as $\delta \ll 1$. This approximation is called as “linear” fluctuations, where the Newtonian approximation plays a roll. Then matter density of fluid ρ meets the following fluid equations and the Poisson equation:

$$\frac{\partial \rho}{\partial t} + \vec{\nabla} \cdot (\rho \vec{u}) = 0 \quad , \quad : \text{Continuity equation}, \quad (1.17)$$

$$\Delta \phi = 4\pi G \rho \quad , \quad : \text{Poisson equation}, \quad (1.18)$$

$$\frac{\partial \rho}{\partial t} + (\vec{u} \cdot \vec{\nabla}) \rho = -\frac{1}{\rho} \vec{\nabla} p - \vec{\nabla} \phi \quad , \quad : \text{Euler equation} \quad (1.19)$$

where ϕ is gravitational potential. We can rewrite these quantities using the Robertson-Walker metric: $\vec{x} = \vec{r}/a(t)$, $\vec{v} = a(t)\dot{\vec{x}}$, $\Phi = \phi(\vec{x}, t) + \frac{1}{2}a(t)\ddot{a}(t)x^2$. Also we can characterize fluctuation by taking $\bar{\rho}$ as homogeneous part

$$\delta(\vec{x}, t) = \frac{\rho(\vec{x}, t) - \bar{\rho}}{\bar{\rho}} \quad (1.20)$$

then Eq. (1.17) to Eq. (1.19) can be converted to:

$$\frac{\partial \delta}{\partial t} + \frac{1}{a} \vec{\nabla} \cdot \vec{v} = 0 \quad , \quad (1.21)$$

$$\Delta \Phi = 4\pi G \bar{\rho} \delta a^2 \quad , \quad (1.22)$$

$$\frac{\partial \vec{v}}{\partial t} + \frac{\dot{a}}{a} \vec{v} = -\frac{c_s^2}{a} \vec{\nabla} \delta - \frac{1}{a} \vec{\nabla} \Phi \quad , \quad (1.23)$$

where c_s^2 is the sound velocity defined as $c_s^2 = \sqrt{\partial p / \partial \rho}$. Note that we apply linear approximation and neglect terms larger than second order. Thus for matter component with $p = 0$, the evolution equation of the density fluctuation in linear approximation can be described as:

$$\ddot{\delta} + 2\frac{\dot{a}}{a}\dot{\delta} - 4\pi G\bar{\rho}\delta = 0 \quad (1.24)$$

The solution is composed by growing mode $D_1(t)$ and decaying mode $D_2(t)$, and described as:

$$\delta(t) = C_1 D_1(t) + C_2 D_2(t) \quad (1.25)$$

Here we look into the properties for the Λ CDM universe. In this model, Hubble parameter H is given by:

$$H(a) = H_0 \sqrt{\Omega_{m0} a^{-3} + \Omega_{\Lambda 0}} \quad (1.26)$$

here we neglect the radiation density $\Omega_{\gamma 0}$ and curvature K , and $w_{\text{DE}} = -1$. As $H(a)$ is a specific solution of Eq. (1.24), the linear growth of matter density is derived by $D(a) = H(a)f(a)$ as:

$$D_1(a) = H(a) \int_0^a \frac{da'}{(a'H(a'))^3}, \quad (1.27)$$

$$D_2(a) = H(a), \quad (1.28)$$

(2) Density evolution for cosmic structures : non-linear regime

Next we focus on the density evolution for $\delta \gg 1$ case, where the effect of the non-linear terms overcome the Hubble expansion in the evolution of over density. Even though the evolution of non-linear growth is difficult to describe analytically, the simplified model, the top-hat spherical collapse model, allows us to analytically solve the evolution of nonlinear density perturbations.

Here we summarize the characteristic dynamics for the spherical collapse model. For simplicity, we consider a positively curved matter-dominated universe, where the Friedmann equations have the parametric form

$$r = A(1 - \cos \theta), \quad (1.29)$$

$$t = B(\theta - \sin \theta), \quad (1.30)$$

where the parameter A, B for the matter dominated universe: $A = \Omega_{\text{m}0}/[2(\Omega_{\text{m}0} - 1)]$, $B = \Omega_{\text{m}0}/[2H_0(\Omega_{\text{m}0} - 1)^{3/2}]$. This solution gives the same evolutionary picture for the shell at radius r with the inner mass M , with the equation of motion : $d^2r/dt^2 = -GM/r^2$. These models characterize the shell behavior: the shell first expands from $\theta = 0$ to $\theta = \pi$, then contract from $\theta = \pi$ to form singularity at $\theta = 2\pi$. These two phases corresponds to turn around phase and virialization in structure formation.

– turn around

The solution of Eq. (1.29) and Eq. (1.30) shows that the spherical region reaches the maximum radius at $\theta = \pi$, where the radius $r_{\text{max}} = 2A$, and $t_{\text{max}} = \pi B$. Then the density of spherical region at the turn around phase is characterized as:

$$\frac{\rho}{\rho_0} = \frac{\Omega_{\text{m}0}\rho_{\text{c}0}/r_{\text{max}}^3}{\rho_{\text{c}0}/a^3} = \frac{9\pi^2}{16} \sim 5.55, \quad (1.31)$$

$$\delta = \frac{3(6\pi)^{2/3}}{20} \sim 1.06 \quad (1.32)$$

where $a = (\frac{3}{2}H_0t)^{2/3}$. Therefore the characteristic overdensity does not depend on the shell mass M .

– virialization

Eq. (1.29) and Eq. (1.30) indicate that the mass density collapse to singularity at $\theta = 2\pi$. In reality, however, the mass distribution reach virtualized first and the singularity is never formed. The potential energy satisfies $E_k = -E_p(r_{\text{max}}/2)/2$, where $E_p(r_{\text{max}}) = -3GM^2/5r_{\text{max}}$ at r_{max} and $E_p(r_{\text{max}}/2) = -6GM^2/5r_{\text{max}}$ at $r = r_{\text{max}}/2$. Thus the contractions of each shell forms objects with a finite size of $r_{\text{vir}} = r_{\text{max}}/2$, and

t_{vir} can be characterized as $t_{\text{vir}} = 2r_{\text{max}}$ (or the case of $\theta = 3\pi/2$ as $t_{\text{vir}} = (\frac{3}{2} + \frac{1}{\pi})t_{\text{max}} \sim 1.81t_{\text{max}}$). Hence the typical overdensity follows;

$$\frac{\rho}{\rho_0} = \nabla_{\text{vir}} = \frac{9\pi^2}{16} \times 8 \times \left(\frac{t_{\text{vir}}}{t_{\text{max}}}\right)^2 \sim 178 \quad (1.33)$$

$$\delta = \frac{3}{20} \left(6\pi \frac{t_{\text{vir}}}{t_{\text{max}}}\right)^{2/3} \sim 1.69, \quad (1.34)$$

1.1.3 Candidates for dark matter

Several observations, such as mass-luminosity relation of clusters and the rotation curve of spiral galaxies shows discrepancy between the observed matter abundance and that of known components (Zwicky 1937). For example, the observation of Type-Ia supernovae and cosmic microwave background suggests that the mass density of matter $\Omega_{\text{M}} \sim 0.3$ (see the detail in § 1.1.1). On the other hand, Big Bang Nucleosynthesis (BBN) theory implies that the baryonic component in the universe is constrained to $0.01 \leq \Omega_b \leq 0.06$. Thus we cannot explain the full quantity of matter component with known matter, which strongly supports the existence of dark matter.

In galactic scale, there is a possibility of existing certain amount of baryonic dark matter in the galactic halo. Neutral hydrogen gas is one candidate, for they are too hot to collapse gravitationally. Also there exists dark candidates so-called massive compact halo object (MACHO), such as stellar remnant, neutron star, stellar black hole (BH), and brown dwarf. Previous microlensing surveys towards Large Magellanic Cloud conclude that MACHOs can contribute up to 20% of the mass of Galactic halo (Alcock et al. 2000).

Not only baryonic components, but non-baryonic candidates beyond the standard model is suggested as feasible dark matter candidate. They are called as the hot dark matter (HDM) and the cold dark matter (CDM). Neutrino is feasible candidate for HDM. HDM has so large energy that they can stay relativistic for long, fluctuations whose scale is smaller than the horizon disappear, thus can hardly form clumpy structure. Therefore HDM is ruled out by the current cosmology model.

On the other hand, cold dark matter (CDM) is a type of dark matter which is free from collisionless damping. In the picture of Λ CDM model, small structures are created first from gravitational instability of initial perturbations. As CDM does not reduce perturbation during structure formation compared with HDM, these small structures gather gravitationally, and merged many times to form larger structures. This kind of structure formation mechanism is called "bottom-up" structure formation. The Λ CDM model, assuming the existence of CDM and dark energy, succeeds to describe the current structures in the universe, and now becomes the cosmological standard model. As for CDM, possible cold dark matter candidates are weakly interacting massive particles (WIMPs) or super-symmetry particles such as axion. However, none of CDM candidates have been detected by the current experiments.

One alternative candidate for non-baryonic candidate is MACHO consisted of primordial black hole (PBH). PBHs are proposed to be generated by primordial perturbation at inflation epoch (Hawking 1974). As they were built before BBN, they are not count for the baryon budget afterwards. Therefore there is no limit on the amount of PBHs from BBN, and can construct whole dark matter in the universe.

1.2 Gravitational lensing

As mentioned in previous chapter, the evolution of overdensity in cosmic density field creates cosmic structures such as galaxy clusters. Around these massive structures one can observe some unique characteristics; distortion and magnification of background objects. These features are caused by distorted light path in the foreground gravitational field, originally predicted by general relativity, and called as gravitational lensing effect. In the following we describe basic property and the summary of observational characteristics.

1.2.1 Basic properties

General relativity describes the distortion of light path in the gravitational field. In the following we briefly mention the behavior of light path in perturbed metric (The simple case in unperturbed metric is described in appendix A).

(1) Lens equation

Here we consider a case where gravitational potential Φ is small. In this case, the metric of inhomogeneously expanding universe can be described as:

$$ds^2 = - \left(1 + \frac{2\Phi}{c^2}\right) c^2 dt^2 + a^2(t) \left(1 - \frac{2\Phi}{c^2}\right) [d\chi^2 + r^2(\chi)d\theta^2], \quad (1.35)$$

where $d\chi = dr^2/1 - Kr^2$, and $d\theta^2 \simeq (d\theta^1)^2 + (d\theta^2)^2$ for distant galaxies. Considering a light path at $x^i = (\theta^1, \theta^2, \chi)$, then the derivative of affine parameter can be described as:

$$\frac{d}{d\lambda} = \frac{d\chi}{dx^0} \frac{dx^0}{d\lambda} \frac{d}{d\chi} = -\frac{P^0}{a} \frac{d}{d\chi} \quad (1.36)$$

where $P^0 = dx^0/d\lambda$. Thus perturbed part of geodetic equation $dk^\mu/d\lambda + \Gamma_{\alpha\beta}^\mu k^\alpha k^\beta = 0$ for $k^\mu = k_{(b)}^\mu + \delta k^\mu$ can be reduced to the first order of θ^1, θ^2 and Φ/c^2 in Taylor expansion (e.g. Schneider et al. 1992):

$$\frac{d^2(r\theta^i)}{d\chi^2} + Kr\theta^i = -\frac{2}{c^2} \frac{\partial\Phi}{\partial(r\theta^i)} \quad (1.37)$$

Therefore the solution is described as:

$$\theta_S^i = \theta^i - \hat{\alpha}^i, \quad (1.38)$$

$$\hat{\alpha}^i = \frac{2}{c^2} \int_0^\chi d\chi' \partial_i \Phi(\chi') \frac{r(\chi - \chi')}{r(\chi)}, \quad (1.39)$$

where θ_S^i represents the position of the source image without lensing effect as in Fig. 1.1, and χ is the position of the source. This is a general expression of the lens equation, and $\hat{\alpha}$ is the deflection angle. In the following we adopt some approximation to describe the basic properties.

- Thin lens approximation

Here we adopt so-called thin-lens approximation; the case where the light deflects

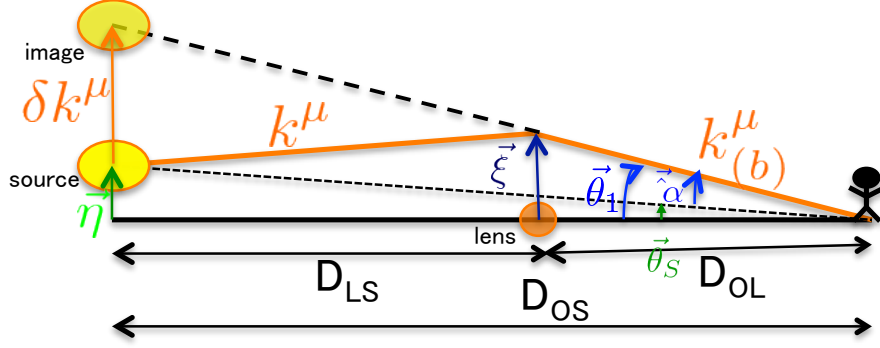


Figure 1.1: Gravitational lensing scheme. Orange line describes the light path from the source object (left) to the observer (right), bent around the gravitational field of the lens (middle).

within a sufficient small region compared to the distance between the source and the observer. In this approximation the deflection angle $\hat{\alpha}$ can be described as:

$$\begin{aligned}
\hat{\alpha}^i &\simeq \frac{2}{c^2} \frac{r(\chi - \chi')}{r(\chi)} \int_0^\chi d\chi' \partial_i \Phi(\chi') \\
&\simeq -\frac{2G}{c^2} \frac{r(\chi - \chi')}{r(\chi)} \int_{-\infty}^{\infty} dz \partial_i \int d\xi' dz' \frac{\rho(\vec{x})}{\sqrt{|\vec{\xi} - \vec{\xi}'|^2 + |z - z'|^2}} \\
&\simeq \frac{4G}{c^2} \frac{r(\chi - \chi')}{r(\chi)} \int d^2\xi' \frac{\vec{\xi} - \vec{\xi}'}{|\vec{\xi} - \vec{\xi}'|^2} \Sigma(\vec{\xi}'), \tag{1.40}
\end{aligned}$$

where we rewrite the gravitational potential as:

$$\Phi(\vec{x}) = -G\bar{\rho} \int d^3x' \frac{\vec{x} - \vec{x}'}{|\vec{x} - \vec{x}'|^2} \delta(\vec{x}). \tag{1.41}$$

and the surface mass density as $\Sigma(\vec{\xi}) = \int_{-\infty}^{\infty} dz \rho(\vec{x})$. In this description we assume $\rho(\vec{x}) \gg \bar{\rho}$, and χ and χ' are the position of the source and lens respectively. Then according to Fig. 1.1, we can substitute the angular diameter distance D_A for $r(\chi)$ and $\vec{\xi} = D_{OL}\vec{\theta}$. Hence, $\vec{\alpha}$ can be described as:

$$\begin{aligned}
\vec{\alpha} &= \frac{4G}{c^2} \frac{D_{OL}D_{LS}}{D_{OS}} \int d^2\theta' \frac{\vec{\theta} - \vec{\theta}'}{|\vec{\theta} - \vec{\theta}'|^2} \Sigma(D_{OL}\vec{\theta}') \\
&= \frac{1}{\pi} \int d^2\theta' \frac{\vec{\theta} - \vec{\theta}'}{|\vec{\theta} - \vec{\theta}'|^2} \hat{\kappa}(D_{OL}\vec{\theta}') \Sigma(D_{OL}\vec{\theta}') \tag{1.42}
\end{aligned}$$

In the second equality we conventionally adopt the following description of the critical surface mass density Σ_{cr} and the dimensionless surface mass density $\hat{\kappa}(D_{OL}\vec{\theta})$:

$$\Sigma_{cr} = \frac{c^2}{4\pi G} \frac{D_{OS}}{D_{OL}D_{LS}}, \tag{1.43}$$

$$\hat{\kappa}(D_{OL}\vec{\theta}) = \frac{\Sigma(D_{OL}\vec{\theta})}{\Sigma_{cr}}. \tag{1.44}$$

Furthermore we transfer the lens equation into dimensionless form. The lens equation can be described with quantities featured in Fig. 1.1:

$$\frac{D_{\text{OL}}}{D_{\text{OS}}}\vec{\eta} = \vec{\xi} - D_{\text{OL}}\vec{\alpha}(\vec{\xi}/D_{\text{OL}}) \quad (1.45)$$

Also we define the characteristic length ξ_0 , $\eta_0 = \xi_0 D_{\text{OS}}/D_{\text{OL}}$ in the source plane. In this case the dimensionless lens equation can be converted with the dimensionless vector $\vec{x} = \vec{\xi}/\xi_0$, $\vec{y} = \vec{\eta}/\eta_0$ as:

$$\vec{y} = \vec{x} - \vec{\alpha}(\vec{x}), \quad (1.46)$$

$$\vec{\alpha}(\vec{x}) = \frac{1}{\pi} \int d^2x' \kappa(\vec{x}') \frac{\vec{x} - \vec{x}'}{|\vec{x} - \vec{x}'|^2}, \quad (1.47)$$

$$\kappa(\vec{x}) \equiv \hat{\kappa}(\vec{\xi}) = \frac{\Sigma(\xi_0\vec{x})}{\Sigma_{\text{cr}}} = \frac{1}{\Sigma_{\text{cr}}} \int_{-\infty}^{\infty} \rho(\vec{r}) dz. \quad (1.48)$$

– Axially symmetric lens

Here we focus on the case where lens are axially symmetric, and derive the expressions of basic lensing formulae. As for the axially symmetric mass distribution, we can rewrite $\kappa(\vec{x}) = \kappa(x)$, where $|\vec{x}| = x$. In this situation, the lens potential of the general form is described as:

$$\Phi(\vec{x}) \equiv \frac{1}{\pi} \int d^2x' \kappa(x') \ln|\vec{x} - \vec{x}'| \quad (1.49)$$

where the scaled deflection angle $\alpha(x)$ is calculated using Eq. (1.20) as :

$$\vec{\alpha}(\vec{x}) = \vec{\nabla}\Phi(x) = 2\frac{\vec{x}}{x} \int_0^x dx' x' \kappa(x') \equiv \alpha(x) \frac{\vec{x}}{x} \quad (1.50)$$

Then the integral form of Eq. (1.49) is described using (4.22) and (4.14) of Gradshteyn & Ryzhik (1994):

$$\begin{aligned} \Phi(\vec{x}) &= \frac{1}{\pi} \int dx' \int d\phi x' \kappa(x') \ln \sqrt{x^2 + x'^2 - 2xx' \cos\phi} \\ &= 2 \ln x \int_0^x dx' x' \kappa(x') + 2 \int_x^{\text{inf}} dx' x' \kappa(x') \ln x' \\ &= 2 \int_0^x dx' x' \kappa(x') \ln \left(\frac{x}{x'} \right) + \text{const.} \end{aligned} \quad (1.51)$$

Therefore the lens equation is reduced to a scalar equation under the condition of $\vec{\alpha} \propto \vec{x}$:

$$y = x - \alpha(x) = x - \frac{d}{dx} \Phi(x) \quad (1.52)$$

and also the Laplacian of Ψ in Eq. (1.49) can be reduced as:

$$\Delta\Phi(\vec{x}) = 2\kappa(\vec{x}) \quad (1.53)$$

(2) Magnification, convergence and shear

In the following we discuss the basic properties of gravitational lensing: magnification and

distortion. Using Eq. (1.53), the distortion of source image can be represented by the following Jacobian matrix:

$$A_{ij} = \frac{\partial \theta_S^i}{\partial \theta^j} \equiv \begin{pmatrix} 1 - \kappa - \gamma_1 & -\gamma_2 \\ -\gamma_2 & 1 - \kappa + \gamma_1 \end{pmatrix} = \begin{pmatrix} 1 - \kappa & 0 \\ 0 & 1 - \kappa \end{pmatrix} + \begin{pmatrix} -\gamma_1 & -\gamma_2 \\ -\gamma_2 & +\gamma_1 \end{pmatrix} \quad (1.54)$$

where κ is convergence and γ is shear; $\gamma_1 = \frac{1}{2}(\Phi_{,11} - \Phi_{,22})$, and $\gamma_2 = \Phi_{,12}$. The former component in the right hand side of Eq. (1.54) contributes to magnification effect of the size of a source image, and the latter one is for anisotropic-stretching effect of the image. The distortion can also be reduced with Eq. (1.40) as following:

$$A_{ij} = \delta_{ij} - \Phi_{,ij}, \quad (1.55)$$

$$\Phi = \frac{2}{c^2} \int_0^\chi d\chi' g(\chi, \chi') \partial_i \partial_j \Phi(\chi') \quad (1.56)$$

where $g(\chi, \chi') = r(\chi - \chi')r(\chi')/r(\chi)$, and we consider up to the second order. Note that the magnification of the image brightness can be described as:

$$\mu = |\mu(\vec{x})| = \left| \frac{1}{\det A(\vec{x})} \right|. \quad (1.57)$$

As Eq. (1.55) indicates that $2\kappa = \Phi_{,11} + \Phi_{,22}$ holds, κ can be described as the integral of matter density perturbation along the line of sight, combined with Eqs. (1.54) and (1.55) as:

$$\kappa = \frac{1}{c^2} \int_0^\chi d\chi' g(\chi, \chi') [\Delta - \partial_\chi^2] \Phi \quad (1.58)$$

$$\begin{aligned} &= \frac{3}{2} \left(\frac{H_0}{c} \right)^2 \Omega_{m0} \int_0^\chi d\chi' g(\chi, \chi') \frac{\delta}{a} - \frac{1}{c^2} \int_0^\chi d\chi' g(\chi, \chi') \partial_\chi^2 \Phi \\ &\simeq \frac{3}{2} \left(\frac{H_0}{c} \right)^2 \Omega_{m0} \int_0^\chi d\chi' g(\chi, \chi') \frac{\delta}{a} \end{aligned} \quad (1.59)$$

where we neglect the second derivative of gravitational potential, and combined the following Poisson equation: $\Delta \Phi = \frac{3}{2} H_0^2 \Omega_{m0} \delta / a$.

On the other hand, convergence and shear in Fourier space are given by:

$$\tilde{\gamma}(\vec{k}) = \tilde{\gamma}_1(\vec{k}) + i\tilde{\gamma}_2(\vec{k}) \quad (1.60)$$

$$\tilde{\kappa}(\vec{k}) = \tilde{\gamma}_1(\vec{k}) \cos 2\phi_{\vec{k}} + \tilde{\gamma}_2(\vec{k}) \sin 2\phi_{\vec{k}} \quad (1.61)$$

$$\therefore \tilde{\gamma}(\vec{k}) = \frac{k_1^2 + k_2^2 + ik_1 k_2}{k^2} \tilde{\kappa}(\vec{k}) \quad (1.62)$$

where $\vec{k} = (k_1, k_2) = k(\cos \phi_{\vec{k}}, \sin \phi_{\vec{k}})$. Therefore the inverse transform of Eq. (1.60) is given as (Seitz & Schneider 1996):

$$\kappa(\vec{k}) = -\frac{1}{\pi} \int d^2\theta' \text{Re}[D^*(\vec{\theta} - \vec{\theta}') \gamma(\vec{k})], \quad (1.63)$$

where $D(z) = (z_1^2 - z_2^2 + 2iz_1 z_2) / z^4$.

Also Eq. 1.55 in polar coordinate provides the following relations:

$$\kappa = \frac{1}{2} \left(\Phi_{\theta\theta} + \frac{1}{\theta} \Phi_{\theta} + \frac{1}{\theta^2} \Phi_{\phi\phi} \right) \quad (1.64)$$

$$\gamma_+ = \tilde{\gamma}_1(\vec{k}) \cos 2\phi_{\vec{k}} + \tilde{\gamma}_2(\vec{k}) \sin 2\phi_{\vec{k}} \quad (1.65)$$

$$\gamma_{\times} = \frac{k_1^2 + k_2^2 + ik_1k_2}{k^2} \tilde{\kappa}(\vec{k}) \quad (1.66)$$

where $(\theta_1, \theta_2) = (\theta \cos \phi, \theta \sin \phi)$, taking origin at the center of gravitational source. Furthermore γ_+ and γ_{\times} are tangential shear and cross component of shear defined as:

$$\gamma_+ = -\gamma_1 \cos 2\phi - \gamma_2 \sin 2\phi \quad (1.67)$$

$$\gamma_{\times} = \gamma_1 \sin 2\phi - \gamma_2 \cos 2\phi \quad (1.68)$$

The averaged description of these quantities in the range of $[\theta, \theta + d\theta]$ is:

$$\langle \kappa \rangle(\theta) = \frac{1}{2} \left(\langle \Phi_{\theta\theta} \rangle + \frac{1}{\theta} \langle \Phi_{\theta} \rangle \right), \quad (1.69)$$

$$\langle \gamma_+ \rangle(\theta) = -\frac{1}{2} \left(\langle \Phi_{\theta\theta} \rangle - \frac{1}{\theta} \langle \Phi_{\theta} \rangle \right), \quad (1.70)$$

$$\langle \gamma_{\times} \rangle(\theta) = 0. \quad (1.71)$$

The property of Eq. (1.71), $\langle \gamma_{\times} \rangle$ is often adopted as the indicator of systematic uncertainty in the observation. Therefore the averaged tangential component is given by:

$$\langle \gamma_+ \rangle(\theta) = -\langle \kappa \rangle(\theta) + \bar{\kappa}(\theta) \quad (1.72)$$

where $\bar{\kappa}(\theta)$ is the circle average of convergence given by:

$$\bar{\kappa}(\theta) = \frac{1}{\pi\theta^2} \int_0^{\theta} 2\pi d\theta' \theta' \langle \kappa \rangle(\theta') = \frac{1}{\theta^2} \int_0^{\theta} 2\pi d\theta' \partial_{\theta'} (\theta' \Phi_{\theta'}) = \frac{1}{\theta} \langle \Phi_{\theta} \rangle. \quad (1.73)$$

(3) Lensing distortion effect

In the following we describe the relation between the shear quantity and observables. As discussed in previous section, the distortion of source image is given by Eq. (1.54). However, κ cannot be measured directly without the knowledge about the original size of the image. What we can only measure is the reduced shear, which is given by taking a factor of $(1 - \kappa)$ out front of Eq. (1.54):

$$g(\vec{\theta}) = \frac{\gamma(\vec{\theta})}{1 - \kappa(\vec{\theta})} \quad (1.74)$$

Fig. 1.2 summarizes the the shape distortion of image due to gravitational light deflection. The ellipticity of galaxies affected by gravitational lensing effect has major axis $a = 1/(1 - \kappa - |\gamma|)$, and minor axis $b = 1/(1 - \kappa + |\gamma|)$. Thus by utilizing ellipticity of galaxies we can reconstruct the shear information.

In order to characterize the system in detail, here we define ellipticity as:

$$\epsilon = \frac{a - b}{a + b} \quad (1.75)$$

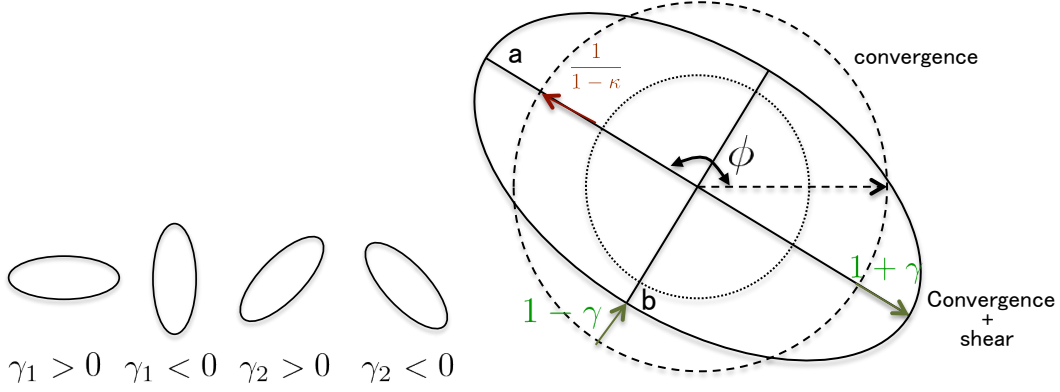


Figure 1.2: Right figure describes ellipticity of a galaxy with gravitational lensing effect. The innermost circle is the original ellipticity of galaxy, the elongated one is affected by right shear and convergence, and the dashed circle represents the case only with convergence signal. Left figures describes the elongated patterns for different shear properties.

The definition of ellipticity can be related to the shear quantity by considering the second order surface brightness moments of a galaxies image (see Bartelmann & Schneider 2001). Suppose that the observed surface brightness of galaxies $I(\theta)$, the center of the image θ is given for all angular separations as:

$$\bar{\theta} \equiv \frac{\int d^2\theta w[I(\theta)]\vec{\theta}}{\int d^2\theta w[I(\theta)]} \quad (1.76)$$

where $w[I(\theta)]$ is weight function. Then the tensor component of the second moment of surface brightness can be described as:

$$Q_{ij} = \frac{\int d^2\theta w[I(\theta)](\theta_i - \bar{\theta}_i)(\theta_j - \bar{\theta}_j)}{\int d^2\theta w[I(\theta)]} \quad (1.77)$$

where $Q_{11} = Q_{22}$ and $Q_{12} = Q_{21} = 0$ for a circular image. Also by the definition of Q_{ij} , we can describe the original ellipticity of galaxy as (Schneider 1996):

$$\epsilon = \epsilon_1 + i\epsilon_2 = \frac{Q_{11} - Q_{22} + 2iQ_{12}}{Q_{11} + Q_{22} + 2(1(Q_{11}Q_{22} - Q_{12}^2))^{1/2}} \quad (1.78)$$

where $\epsilon_1 = \epsilon_2 = 0$ for a circular image. Under these conditions we can calculate the original ellipticity of galaxy as:

$$\epsilon^{\text{int}} = \begin{cases} \frac{\epsilon - g}{1 - g^*\epsilon}, & (\text{for } |g| \leq 1) \\ \frac{1 - g\epsilon^*}{\epsilon^* - g^*}, & (\text{for } |g| > 1) \end{cases} \quad (1.79)$$

where $\epsilon \sim \epsilon^{\text{int}} + g$. Note that the signal from shear is usually overwhelmed by large uncertainty from the measurement of ellipticity of galaxy. Therefore the statistical analysis of ellipticity plays a key role. As there is no reason for preferred orientation of galactic shear, the average intrinsic ellipticity would be canceled if we stack the ellipticities from multiple galaxies. Also from Fig. 1.2, the average additional ellipticity is represented by

the reduced shear in the weak lensing regime. Hence $\langle g \rangle + 0 = \langle \epsilon \rangle$, and we can construct the estimator for the shear as:

$$\gamma \sim g \sim \langle g \rangle = \langle \epsilon \rangle \quad (1.80)$$

This stacking method is valid for the small sky survey where the gravitational field can be taken as uniform.

1.2.2 Observational characteristics

The main characteristics of gravitational lensing is distortion and magnification. These properties provide useful information to probe cosmic properties. Here we briefly summarize the characteristics following a conventional classification.

- Strong lensing
When foreground object is massive enough like in the galaxy of clusters, multiple images of background object can show up. This phenomenon is first observed for quasar system (Walsh et al. 1979). One unique point is that different image has different timing of maximum magnification. Thus one can know about Hubble constant by tracing the time delay of QSO between different images and compare with theory. Also sometimes structure called arcs or Einstein ring can show up.
- Weak lensing
In the system of strong gravitational field like in clusters, the image of background galaxies are distorted in the gravitational field. This shear property can be extracted even for weak gravitational field by statistical analysis of multiple signals. If enough statistics can be achieved, we can reconstruct the mass distribution in a wide range up to a few Mpc.
- Microlensing
Another important feature of gravitational lensing is magnification the surface brightness of background objects. This magnification can be detected even when two images are too close to be separated. Magnification effect plays an important role in searching dark undetected object such as exoplanets.

1.3 Objective of this thesis

The existence of dark matter is strongly supported by several observations by the discrepancy in the amount of baryon (4%) and total matter component (24%). Previous studies suggest that dark matter with “cold” property is consistent with bottom-up structure formation scenario, which can produce structures like galaxies and clusters of galaxies currently observed in the universe. However, feasible candidate such as weakly interacting massive particles (WIMPs) and massive compact halo objects (MACHOs) is not detected, and properties such as particle mass is also unknown.

This thesis presents two kinds of tests for dark matter study, aiming to develop methods to investigate new property at ongoing and future wide field survey including Subaru Hyper Suprime-Cam (HSC)². Part I proposes a new method to investigate mass distribution of galaxy clusters. Currently weak lensing effect combined with popular method called stacked analysis

²http://www.naoj.org/Projects/HSC/j_index.html

is a powerful method to probe the mass distribution in the universe. However, stacking analysis cannot trace the individual property of clusters. Therefore we construct a new method to extract small features hidden in dark matter profiles. The structure of Part I is as follows. In § 1 we briefly review the property of dark halo profile. In § 2.2, after briefly reviewing the lensing observables of NFW halo, we will derive an estimator of the lensing distortion profile measurement with NFW scaling. Then we study the feasibility of this method using analytical NFW models and N -body simulations. In § 2.3.1 we briefly describe the Subaru weak lensing catalog and the X-ray observables for the sample of massive clusters we use in this paper. We will show the main results of Part I in § 2.3, and § 2.4 is devoted to summary and discussion.

Part II of this thesis presents another approach to investigate dark matter; microlensing study to search for dark matter candidate called primordial black hole (PBH). Dark matter search by microlensing effect is performed on several projects. Owing to the survey for years they succeed to detect Sun-scale dark stars such as brown dwarfs. However no plausible candidate of PBH is ever discovered so far, and current constraint still remains the possibility of PBH abundance as much as baryonic component for Moon-scale objects. In this study we propose a transient search at M31 dense-star region, using Hyper Suprime-Cam at Subaru telescope. Our survey expects higher event rate of PBH microlensing than previous search, owing to highly-resolved imaging data. One difficulty is that software reductions also need some careful treatments, because no previous transient search exists for such a dense field with highly resolved wide field camera. Thus we develop the method to optimize the transient analysis. The structure of Part II is as follows. In § 3.1 we briefly review the property of microlensing study. In § 3.2 we describe our observational method and the data process in detail. Observational implication we acquired from our dataset in § 3.3. In § 3.4 we describe the method to constrain the event rate of primordial black hole. We also report the current status about the PBH microlensing search.

Chapter 2

Universal test of cluster dark matter halos with weak lensing

2.1 Introduction

This work has been published in Niikura et al.(2015)

2.1.1 Density profile of dark halos

As mentioned in the introduction part of § 1.1.2, cosmic structure formation theory suggests that massive structures such as halos are formed by non-linear density evolution. In fact, there exist some properties of halo structure beyond prediction of spherical collapse model, such as concentrated mass distribution in the central region and the slope of mass density profile. In order to probe such complicated properties, halo-profile model is expected to be a good indicator; especially the following two models of inner halo profile play key roles:

- Singular Isothermal Sphere(SIS) model

SIS model is a simple model; one assumes thermal equilibrium state in isothermal sphere, where the distribution function in the sphere follows the Maxwell-Boltzmann model:

$$f(\mathcal{E}) = \frac{\rho_1}{(2\pi\sigma^2)^{3/2}} \exp\left(\frac{\Phi - v^2/2}{\sigma^2}\right) \quad (2.1)$$

Therefore the density field can be described as $\rho = \rho_1 \exp(\Phi/\sigma^2)$. By inserting this result Poisson equation gives:

$$\frac{1}{r^2} \frac{d}{dr} \left(r^2 \frac{d \log \rho}{dr} \right) = -4\pi G \sigma^2 \rho \quad (2.2)$$

This equation has special solution: $\rho = \sigma^2/2\pi G r^2$, which gives flat rotation curves, a common characteristic often observed for spiral galaxies.

- Navarro-Frenck-White(NFW) model

One of the most important predictions in N -body simulations of Λ -dominated, cold dark matter structure formation model (Λ CDM) is the emergence of universal mass density profile in dark matter halos. These mass density profile can be well fitted by a “universal”

two-parameter family of the model profile over a wide range of halo masses, first proposed in Navarro et al. (1996, 1997, hereafter NFW). The NFW profile predicts a monotonically steepened profile with increasing radius, with logarithmic slopes shallower than an isothermal sphere interior to the characteristic “scale” radius $r < r_s$, but steeper at larger radius, approaching to r^{-3} at the virial radius, $r \rightarrow r_{\text{vir}}$.

Note that one sometimes adopts corrections in addition to the simple inner density profile of halos (Miyatake et al. 2015). For example, one need to take into account the surrounding mass distribution, especially at larger radius around $R \simeq 10\text{Mpc}/h$ where the the mass distribution can be suffered from that of neighboring galaxies. One can include this effect as two-halo term, by taking advantage of the two-point correlation function between the clusters and the surrounding mass distribution. For more precise modeling, one can also consider the effect from stellar mass contribution and miss-centering effect (Takada & Jain 2002; Oguri & Hamana 2011).

2.1.2 Observational implication of clusters

As mentioned in previous section, halo profiles are well described by N-body simulations and several models such as NFW profile are proposed. These models can be good indicators to test the observational property with predictions from ΛCDM model. In the following we describe several ways to construct cluster mass distribution from observational data.

- a) Mass distribution from Gravitational lensing effect
Gravitational lensing is a powerful tool to construct the mass distribution. We can probe the mass distribution using the information of convergence and shear as mentioned in § 1.2. As for cluster mass distribution, one can probe up to a few Mpc from the center by stacking the signals of weak lensing measurements. On the other hand, strong lens can probe inner profile, which can probe mass distribution up to a few kpc from the center.
- b) Mass indication from Richness
Richness is a simple concept; the number of member galaxies in a cluster. Owing to the empirical correlation relation with weak lensing analysis one can provide the information of cluster mass from richness data.
- c) Mass indication from X-ray surface brightness
X-ray observation can probe photons emitted due to thermal Bremsstrahlung. Owing to high signal-to-noise ratio of surface brightness compared to optical observation, X-ray observation can be a clue to detect clusters. By assuming hydrostatic equilibrium state or isothermal- β model, the surface brightness data can probe inner mass profile up to the region within $\Delta = 2500$ or 500 of overdensity.
- d) Mass distribution from Sunyaev-Zel’dovich effect
One can also make use of the inverse-Compton scattering, caused when photons from CMB radiation interact with a few-keV electrons in clusters. Furthermore, the movement of electrons in the line of sight can produce another deviation from the background temperature map, which features the mass distribution of clusters.

2.1.3 Preview of our study

Clusters of galaxies are the largest, gravitationally bound objects in the universe, and the formation and evolution processes are dominated by gravitational effects mainly due to dark matter. Hence clusters provide us with a useful laboratory of studying the nature of dark matter (Clowe et al. 2006). Especially the NFW model, one of the most important prediction from the hierarchical Λ CDM model, is powerful property to test. the physical origin is Dalal et al. (2010), for example. Further, the ratio of the characteristic scale radius to the virial radius, which characterizes the degrees of central concentration of the mass distribution – the so-called halo concentration c , tends to be lower for more massive halos. In addition the halo concentration of a fixed halo mass displays intrinsic scatters typically given by $\sigma_{\ln c} \sim 0.2$, originating from details of the mass accretion or assembly history of each halo in the hierarchical structure formation (Bullock et al. 2001; Wechsler et al. 2002; Zhao et al. 2003; Duffy et al. 2008; Zhao et al. 2009; Bhattacharya et al. 2013; Diemer & Kravtsov 2014). Thus these properties of dark matter halos are important predictions of Λ CDM model, and need to be carefully tested by comparing with measurements.

Gravitational lensing is a unique, powerful method enabling one to probe the matter distribution in galaxy clusters irrespective of their physical and dynamical states (Schneider 2006). Among the methods to investigate the mass density profile, the stacked weak lensing analysis combining multiple clusters has been proven to be a robust, powerful method of probing the average mass distribution of the sampled clusters (Johnstone et al. 2007; Okabe et al. 2010a; Oguri et al. 2012; Okabe et al. 2013; Umetsu et al. 2014). These works have shown that the average mass profile measured from the stacked lensing is in remarkably nice agreement with a prediction from N-body simulation, so-called “the NFW prediction”. Another advantage of the stacked lensing is it allows one to probe the mass distribution even for less massive halos, such as galaxy-scale halos, as long as a sufficient number of sampled halos are used in the analysis (Mandelbaum et al. 2005; Leauthaud et al. 2010; Miyatake et al. 2013). However, a downside of the stacked lensing method is a loss of the lensing information of individual clusters. Hence a knowledge of the distribution of the underlying halo parameters in the sampled clusters such as their halo masses is of critical importance in order not to have any bias in the NFW parameters inferred from the stacked lensing signals (Oguri & Takada 2011). This is equivalent to the importance of exploring a well-calibrated proxy relation of halo parameters with cluster observables (Rozo et al. 2009; Zhang et al. 2010; Okabe et al. 2010b; Zhang et al. 2011; Mahdavi et al. 2013; von der Linden et al. 2014; Martino et al. 2014; Okabe et al. 2014).

We develop a method of measuring the lensing distortion profiles of clusters, motivated by the NFW prediction. We propose the “NFW scaling” analysis for the lensing measurements, which is done by averaging the “scaled” amplitudes of background galaxy ellipticities in each bin of the “scaled” radii according to the NFW prediction of individual cluster. With this NFW scaling method, we can address whether clusters in the universe display the universality of their lensing profiles as seen in simulations. First, to demonstrate the feasibility of the NFW scaling analysis, we will use simulations of cluster lensing observables based on a suite of high-resolution N -body simulations. Then, as a proof of concept of this method, we will apply this method to the Subaru weak lensing data¹ for a volume-limited sample of 50 massive clusters that are taken from the published results (Okabe et al. 2010a, 2013; Martino et al. 2014), which comprises *all* clusters from the *ROSAT* All Sky Survey catalogs (Ebeling et al. 1998, 2000; Bohringer et al.

¹Based in part on data collected at Subaru Telescope and obtained from the SMOKA, which is operated by the Astronomy Data Center, National Astronomical Observatory of Japan.

2004) in the redshift range $0.15 \leq z \leq 0.3$. To estimate the NFW scaling of each cluster, we will use the halo mass estimate in Martino et al. (2014) based on the *XMM* and/or *Chandra* X-ray observables, and use the halo concentration inferred from the model scaling relation between halo mass and concentration in Diemer & Kravtsov (2014). Then by comparing the scatters of 50 cluster lensing profiles relative to the NFW predictions for two cases with and without the NFW scaling, we test the performance of this method as well as the universality of the cluster mass distribution. Unless stated otherwise, we will adopt a flat Λ CDM cosmology with $\Omega_m = 0.27$, $\Omega_\Lambda = 0.73$, and the Hubble parameter $h = H_0/(100 \text{ km s}^{-1} \text{ Mpc}^{-1}) = 0.70$.

2.2 Methodology : stacked weak lensing with NFW scaling

2.2.1 Lensing of Navarro-Frenk-White halo

The Navarro-Frenk-White (1997; hereafter NFW) mass density profile for a halo is parametrized by two parameters as

$$\rho_{\text{NFW}}(r) = \frac{\rho_c}{(r/r_s)(1+r/r_s)^2}, \quad (2.3)$$

where r_s is the scale radius and ρ_c is the central density parameter. The parameter ρ_c is specified by imposing that the mass enclosed within a sphere of a given overdensity Δ is equal to the halo mass M_Δ ,

$$\rho_c = \frac{\Delta \rho_{\text{cr}}(z) c_\Delta^3}{3 m_{\text{NFW}}(c_\Delta)} = \frac{M_\Delta}{4\pi r_s^3 m_{\text{NFW}}(c_\Delta)}, \quad (2.4)$$

where $m_{\text{NFW}}(c_\Delta) \equiv \int_0^{c_\Delta} dx x/(1+x)^2 = \ln(1+c_\Delta) - c_\Delta/(1+c_\Delta)$, $c_\Delta \equiv r_\Delta/r_s$, a concentration parameter, and $\Delta(z)$ is a nonlinear overdensity introduced to define the interior mass for each halo. Note that throughout this paper we employ halo mass definition with respect to the critical density, not the mean mass density: $M_\Delta \equiv (4\pi/3)r_\Delta^3 \rho_{\text{cr}}(z)\Delta$.

Several works have shown a scaling relation of the halo concentration with halo mass, using numerical simulations or based on analytical arguments (Bullock et al. 2001; Wechsler et al. 2002; Zhao et al. 2003; Duffy et al. 2008). As for our fiducial model, we adopt the publicly-available code provided by B. Diemer to compute the halo mass and concentration relation in Diemer & Kravtsov (2014, hereafter DK14 and see references therein). Note that we used the ‘‘median’’ relation, rather than the mean, for our default choice as recommended in DK14. The mass estimates from the X-ray observables are not M_{200c} , and rather the interior mass of a greater overdensity such as M_{500c} . Assuming that a halo exactly follows the NFW profile, we can convert the scaling relation calibrated for M_{200c} to the c_{500c} - M_{500c} relation, based on the method in Hu & Kravtsov (2003). The public code of DK14 allows us to compute the halo concentration for an input overdensity based on this method.

For an NFW profile, we can derive an analytical expression for the lensing convergence and shear profiles (Bartelmann 1996; Golse & Kneib 2002):

$$\begin{aligned} \kappa^{\text{NFW}}(R) &\equiv \frac{\Sigma^{\text{NFW}}(R)}{\Sigma_{\text{cr}}(z_1, z_s)} = 2\rho_c r_s \frac{g^{\text{NFW}}(R/r_s)}{\Sigma_{\text{crit}}(z_1, z_s)}, \\ \gamma_+^{\text{NFW}}(R) &\equiv \frac{\Delta \Sigma^{\text{NFW}}(R)}{\Sigma_{\text{cr}}(z_1, z_s)} = 2\rho_c r_s \frac{f^{\text{NFW}}(R/r_s)}{\Sigma_{\text{crit}}(z_1, z_s)}, \end{aligned} \quad (2.5)$$

where R is the projected comoving radius from halo center, and the functions $f^{\text{NFW}}(x)$ and $g^{\text{NFW}}(x)$ are given by

$$g^{\text{NFW}}(x) = \begin{cases} \frac{1}{x^2 - 1} \left(1 - \frac{1}{\sqrt{1 - x^2}} \cosh^{-1} \frac{1}{x} \right), & (x < 1) \\ \frac{1}{3}, & (x = 1) \\ \frac{1}{x^2 - 1} \left(1 - \frac{1}{\sqrt{x^2 - 1}} \cos^{-1} \frac{1}{x} \right), & (x > 1) \end{cases} \quad (2.6)$$

and

$$f^{\text{NFW}}(x) = \begin{cases} \frac{2}{x^2} \ln \frac{x}{2} + \frac{1}{1 - x^2} \left(1 + \frac{2 - 3x^2}{x^2 \sqrt{1 - x^2}} \cosh^{-1} \frac{1}{x} \right), & (x < 1) \\ \frac{5}{3} - 2 \ln 2, & (x = 1) \\ \frac{2}{x^2} \ln \frac{x}{2} - \frac{1}{x^2 - 1} \left(1 + \frac{2 - 3x^2}{x^2 \sqrt{x^2 - 1}} \cos^{-1} \frac{1}{x} \right), & (x > 1). \end{cases} \quad (2.7)$$

The critical surface mass density Σ_{crit} for a given system of lens cluster and source at redshifts z_1 and z_s , respectively, is given as

$$\Sigma_{\text{crit}}(z_1, z_s) = \frac{c^2}{4\pi G} \frac{D_A(z_s)}{D_A(z_1) D_A(z_1, z_s) (1 + z_1)^2}, \quad (2.8)$$

where $D_A(z)$ is the angular diameter distance and the factor $(1 + z_1)^2$ is from our use of the comoving scale. From Eqs. (2.4) and (2.5), we can find that the lensing amplitudes of an NFW halo scale with the NFW parameters (M_Δ, c_Δ) as

$$\begin{aligned} \kappa^{\text{NFW}}, \gamma_+^{\text{NFW}} &\propto 2\rho_c r_s \propto M_\Delta / (r_s^2 m_{\text{NFW}}(c_\Delta)) \\ &\propto M_\Delta^{1/3} c_\Delta^2 / m_{\text{NFW}}(c_\Delta). \end{aligned} \quad (2.9)$$

If we employ the c_Δ - M_Δ scaling relation given as $c_\Delta(M_\Delta) \propto M^{-\alpha}$, the lensing amplitudes roughly scale with halo mass as $\gamma_+^{\text{NFW}} \propto M^{1/3-2\alpha}$ as the function $m(c_\Delta)$ has a weak dependence on halo mass. Note that, since the cluster sample is among the most massive clusters, we have checked that the 2-halo term is much smaller than the above 1-halo term, by a factor of 100, over a range of the radii we consider (e.g., see Oguri & Takada 2011; Takada & Spergel 2014). Therefore we ignore the 2-halo term for the following analysis.

An actual lensing observable estimated from ellipticities of background galaxies for an NFW lens is the lensing ‘‘distortion’’ profile or reduced shear profile:

$$\langle e_+ \rangle(R) \rightarrow \frac{\gamma_+^{\text{NFW}}(R)}{1 - \kappa^{\text{NFW}}(R)}, \quad (2.10)$$

where e_+ is the tangential component of the ellipticities with respect to cluster center. The reduced shear correction is not negligible at the inner radii, and we need to take into account the correction.

2.2.2 Stacked lensing without NFW scaling

For the standard method to estimate the stacked lensing profile for N_c clusters, we follow the method in Johnstone et al. (2007) and Mandelbaum et al. (2013):

$$\langle \widehat{\Delta\Sigma} \rangle(R) = \frac{1}{N} \sum_{a=1}^{N_c} \sum_{i_a; |\mathbf{R}_{(a)i_a}| \in R} w_{(a,i_a)} \Sigma_{\text{cr}(a)} e_{(i_a)+}(\mathbf{R}_{i_a}), \quad (2.11)$$

where $e_{(i_a)+}$ is the tangential ellipticity of the i_a -th background galaxy in the a -th cluster region, and N is the normalization factor defined as

$$N = \sum_{a=1}^{N_c} \sum_{i_a} w_{(a,i_a)}. \quad (2.12)$$

The summation \sum_a runs over the sampled clusters, from $a = 1$ to $N_c = 50$ in our study, and the summation $\sum_{i_a; |\mathbf{R}_{(a)i_a}| \in R}$ runs over all the background galaxies that reside in the annulus of radius R from the a -th cluster center to within the bin width. We employ the weight given as

$$w_{(a,i_a)} = \frac{1}{\Sigma_{\text{cr}}(z_a, z_{i_a})^2 (e_{(i_a)}^2 + \sigma_{(i_a)e}^2 + \alpha^2)}, \quad (2.13)$$

where z_{i_a} is the redshift of the i_a -th background galaxy, $e_{(i_a)}$ is the ellipticity amplitude, $\sigma_{(i_a)e}$ is the measurement error and α is the constant factor to regularize the weight for which we adopt $\alpha = 0.4$ (Okabe et al. 2010a).

Since we need to employ a finite number of the radial bins to study the “shape” of lensing distortion profile, which binning scheme to use is not so clear. As for the representative value of a given radial bin, we use the average of radii of background galaxies that reside in the annulus taking into account their weights:

$$R \equiv \frac{\sum_{a=1}^{N_c} \sum_{i_a; |\mathbf{R}_{(a)i_a}| \in R} w_{(a,i_a)} R_{(a)i_a}}{\sum_{a=1}^{N_c} \sum_{i_a; |\mathbf{R}_{(a)i_a}| \in R} w_{(a,i_a)}}. \quad (2.14)$$

In the literature the area-weighted value of each radial bin is often used. We have checked that, using an analytical NFW profile and taking the actual distribution of background galaxies in the Subaru data, the above radial binning is more accurate in a sense that the distortion profile is in better agreement with the model NFW profile amplitude inferred by the representative value of the radial bin, less than 1% in the fractional difference for most cases.

The statistical uncertainty of the stacked lensing at each radial bin can be estimated as

$$\sigma_{\langle \Delta\Sigma \rangle}(R)^2 = \frac{1}{2N^2} \sum_a \sum_{i_a; |\mathbf{R}_{(a)i_a}| \in R} w_{(a,i_a)}^2 \Sigma_{\text{cr}(a)}(z_a, z_{i_a})^2 e_{(i_a)}^2. \quad (2.15)$$

In this thesis we consider the intrinsic ellipticities as a source of the statistical errors in the lensing measurement, and ignore the cosmic shear contribution that arises from different mass distribution along the same line of sight to the cluster. For our study this is practically a good approximation, because the mean number density of background galaxies is small, about 5 arcmin^{-2} , after a secure selection of background “red” galaxies as we will discuss in § 2.3.1

When comparing the measured lensing profile to an NFW model, we need to account for the contribution of reduce shear. In this paper, assuming that all the clusters follow a single NFW

profile in average sense, we model the the stacked lensing profile, according to Eqs. (2.5) and (2.10) as

$$\begin{aligned} \langle \widehat{\Delta\Sigma} \rangle (R) &\iff \frac{\Delta\Sigma^{\text{NFW}}(R)}{1 - \kappa^{\text{NFW}}(R)} \\ &\simeq \Delta\Sigma^{\text{NFW}}(R) \left[1 + \left\langle \frac{1}{\Sigma_{\text{cr}}} \right\rangle \Sigma^{\text{NFW}}(\langle R \rangle) \right], \end{aligned} \quad (2.16)$$

where the notation “ \iff ” is meant to denote the comparison between the measurement (left-hand side) and the model profile (right-hand side). The notation $\langle \ \rangle$ on the right-hand side denotes the average taking into account the weights of background galaxies in each cluster region as in Eq. (2.14). We will use the above equation to estimate the halo mass and concentration parameter, M_Δ and c_Δ , from the measured lensing profile.

2.2.3 Stacked lensing with NFW scaling

Now we consider the stacked lensing analysis with “NFW scaling”. To implement this method we combine the weak lensing measurement and X-ray observables, where the X-ray observables are needed to estimate halo mass of each cluster independently of the lensing observables. Assuming that each of the 50 clusters follows an NFW profile specified by their respective parameters, $M_{(a)}$ and $c_{(a)}$, we can define an estimator of the *normalized* NFW lensing profile from the measured ellipticities of background galaxies, as motivated by Eq. (2.5):

$$\langle \widehat{f^{\text{NFW}}} \rangle (x) = \frac{1}{N} \sum_{a=1}^{N_c} \sum_{i_a; |\mathbf{x}_{(a)i_a}| \in x} \frac{w_{(a,i_a)} \Sigma_{\text{cr}(a)} e_{(i_a)} + (\mathbf{x}_{i_a})}{2\rho_c \left(M_{(a)}^X, c_{(a)}^X \right) r_s \left(M_{(a)}^X, c_{(a)}^X \right)}. \quad (2.17)$$

Here $M_{(a)}^X$ and $c_{(a)}^X$ are the halo mass and concentration for the a -th cluster, estimated from the X-ray observables (see below for details). The *scaled* radius in the above equation, x , is defined for the a -cluster as $\mathbf{x}_{(a)i_a} \equiv \mathbf{R}_{(a)i_a} / r_s(M_{(a)}^X, c_{(a)}^X)$, where r_s is the scale radius of NFW profile, $r_s = r_\Delta / c_\Delta$. We use the representative value of each radial bin, defined in a similar manner to Eq. (2.14). The central density parameter of NFW profile, ρ_c , can be estimated from $M_{(a)}^X$ and $c_{(a)}^X$ for the a -th cluster, from Eq. (2.4). Note that the profile $\langle \widehat{f^{\text{NFW}}} \rangle$ and the radius x are dimension-less. With the above NFW scaling, weak lensing signals due to less massive halos than the mean mass in the sampled clusters are up-weighted, while the signals of more massive halos are down-weighted. In the following, when comparing the lensing profiles with and without NFW scaling, we use exactly the same background galaxies in the 50 cluster regions.

Similarly, the measurement errors of the stacked profile at each radial bin are estimated as

$$\sigma_{\langle \widehat{f^{\text{NFW}}} \rangle} (x)^2 = \frac{1}{2N^2} \sum_a \sum_{i_a; |\mathbf{x}_{(a)i_a}| \in x} \frac{w_{(a,i_a)}^2 \Sigma_{\text{cr}(a)}^2 (z_a, z_{i_a})^2 e_{(i_a)}^2}{4\rho_c \left(M_{(a)}^X, c_{(a)}^X \right)^2 r_s \left(M_{(a)}^X, c_{(a)}^X \right)^2}. \quad (2.18)$$

To test an improvement in the stacked lensing analysis of NFW scaling compared to the standard stacked lensing, we compare the scatters of lensing distortion profiles of 50 clusters relative to the NFW prediction. We quantify the scatters by

$$d^2 \equiv \sum_{a=1}^{50} \sum_i \frac{\left[\widehat{\Delta\Sigma}_{(a)}(R_{(a)i}) - \Delta\Sigma^{\text{bf-NFW}}(R_{(a)i}; M_{\text{bf}}, c_{\text{bf}}) \right]^2}{\sigma_{\Delta\Sigma_{(a)}}(R_{(a)i})^2} \quad (2.19)$$

or

$$d_{w\text{-scaling}}^2 \equiv \sum_{a=1}^{50} \sum_i \frac{\left[\widehat{f_{(a)}^{\text{NFW}}}(x_{(a)i}) - f^{\text{NFW}}(x_{(a)i}) \right]^2}{\sigma_{f^{\text{NFW}(a)}}(x_{(a)i})^2}. \quad (2.20)$$

Here $\widehat{\Delta\Sigma_{(a)}}$ and $\widehat{f_{(a)}^{\text{NFW}}}$ are the measured distortion profile without and with NFW scaling for the a -th cluster, which are estimated in the similar manner to Eqs. (2.11) and (2.17), and $\sigma_{\Delta\Sigma_{(a)}}$ and $\sigma_{f^{\text{NFW}(a)}}$ are the errors at each radial bin, estimated similarly to Eqs. (2.15) and (2.18), respectively. $\Delta\Sigma^{\text{bf-NFW}}(R)$ is the best-fit NFW profile of the stacked lensing profile (Eq. 2.16). For the NFW scaling case, we similarly include the reduced shear correction: we multiply the function $f^{\text{NFW}}(x)$ (Eq. 2.7) by the function, $1 + \langle 1/\Sigma_{\text{cr}} \rangle_{w(a,i_a)} \Sigma^{\text{NFW}}(x)$ as in Eq. (2.16), where we used the best-fit NFW model of the stacked lensing profile without NFW scaling in order to compute $\Sigma^{\text{NFW}}(x)$. The above d^2 and $d_{w\text{-scaling}}^2$ are equivalent to the log-likelihood functions of 50 lensing distortion profiles assuming that the statistical errors are given by the intrinsic ellipticities. The radial bin $R_{(a)i}$ or $x_{(a)i}$ for the a -th cluster is similarly computed by Eq. (2.14) from the background galaxies that reside in the annulus of the cluster. We carefully employ the radial binning scheme so as to preserve the same background galaxies in the i -th radial bins for both the two cases. With this binning scheme, the relation $d^2 = d_{w\text{-scaling}}^2$ holds if setting the model profiles to $\Delta\Sigma^{\text{bf-NFW}} = f^{\text{NFW}} = 0$ ². If the lensing distortion profiles of 50 clusters are similar in their shapes and amplitudes, following the NFW profile, the value of d^2 is expected to become smaller: $d_{w\text{-scaling}}^2 < d^2$.

2.2.4 Testing the method with N -body simulations

In this section, before going to the Subaru data, we test our method using analytical NFW model and high-resolution N -body simulations.

First we consider an ideal case, albeit unrealistic, that each of 50 clusters *exactly* follows an NFW profile. Figure 2.1 shows the lensing profiles with or without the NFW scaling for 50 halos. To take into account variations in halo masses that resemble the 50 clusters, we assign one-by-one the X-ray inferred masses of 50 cluster to NFW halos³. Note that we use the c - M scaling relation in DK14 to compute the halo concentration for each NFW halo. The different blue curves show each NFW distortion profile relative to the best-fit NFW model of the stacked distortion profile, as a function of the radius relative to the scale radius of the best-fit NFW model. Here we consider the same range of radii, $0.14 \leq R/[h^{-1}\text{Mpc}] \leq 2.8$ for all the halos as we will do for actual analysis of Subaru data. For the range of cluster masses, the lensing distortion amplitudes differ from each other by up to a factor of 2.

On the other hand, the red curves in Figure 2.1 show the profiles after the NFW scaling implementation, assuming that the true mass and concentration of each cluster are *a priori* known, i.e. an ideal case. Each curve is the fractional profile relative to the NFW distortion profile including the reduced shear correction, $f^{\text{NFW}}(x)$ (Eq. 2.7 and see below Eq. 2.17). The deviation from unity is due to an imperfect correction of the reduced shear: the nonlinear correction becomes non-negligible at small radii, and breaks the universality of the NFW lensing profile. The horizontal axis is in the units of the “scaled” radius, R/r_s , where r_s is the NFW scale radius

²If we set $\Delta\Sigma^{\text{bf-NFW}} = f^{\text{NFW}} = 0$ in Eqs. (2.19) and (2.20), the values of d^2 give the cumulative signal-to-noise ratio of the lensing distortion measurements for the 50 clusters.

³We here employed the hydrostatic equilibrium mass in Martino et al. (2014), which was estimated from the X-ray observables of each cluster.

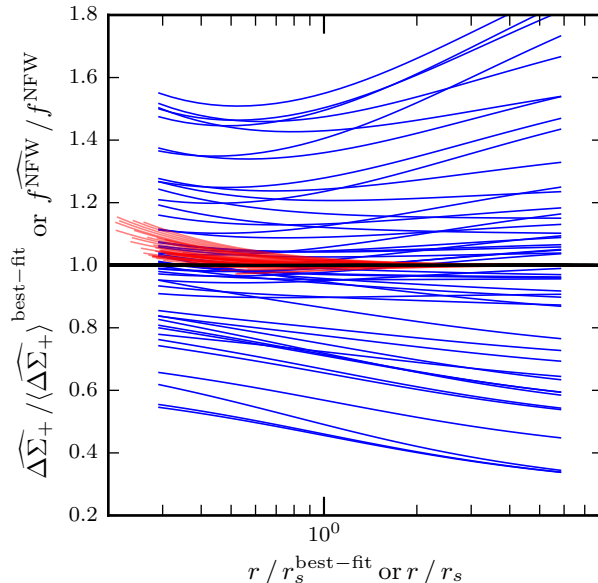


Figure 2.1: The distribution of NFW lensing profiles for 50 halos for each of which we took the X-ray inferred mass of 50 Subaru clusters (here the hydrostatic equilibrium mass in Table 2.1) and assumed the halo concentration based on the halo mass and concentration relation, $c = c(M_{500c})$, in Diemer & Kravtsov (2014, hereafter DK14). The blue curves are the lensing profiles without “NFW scaling”, and the red curves are the lensing profiles with “NFW scaling”. These profiles are normalized by the best-fit NFW profile to the stacked profile.

of each halo. Due to the radial transformation from the original fixed range of R , the range of the scaled radius x , covered by each halo, differ from each other. The figure shows that the NFW scaling significantly reduces the scatters of lensing profiles, making the differences within 20% over a range of radii we consider.

Obviously actual clusters have much more complicated mass distribution than an analytical NFW model: intrinsic scatters of halo concentration, aspherical mass distribution, substructures and so on. To study these effects we use simulated halos of cluster scales, generated from a high-resolution N -body simulation in Takahashi et al. (2012). In brief the N -body simulation was ran with the publicly-available *Gadget-2 code* (Springel et al. 2001; Springel 2005) assuming the WMAP cosmology. The simulation employed 1024^3 particles in a box of $320 h^{-1}\text{Mpc}$ on a side. The mass resolution (the particle mass) is $2.3 \times 10^9 h^{-1}M_\odot$, so is sufficient to resolve cluster-scale halos.

To construct a catalog of cluster-scale halos from the N -body simulation output at $z = 0$, we used the friends-of-friends (FoF) group finder (e.g. Davis et al. 1985) with a linking length of 0.2 in units of the mean interparticle spacing. For each halo we determined the halo center using an iterative technique in which the center of mass of particles within a shrinking sphere is computed recursively until a few particles are left inside (e.g. Power et al. 2003; Masaki et al. 2013). Then the halo mass is defined by a spherical overdensity method – summing all the particles within a sphere of a given overdensity Δ around the halo center. We constructed a catalog that consists of most massive 50 halos from the two simulation realizations. Besides the mass threshold, we did not employ any other selection criteria such as sphericity or the degree of mass distribution complexity. The mean mass of the selected halos is similar to the average mass estimated from the lensing measurements of 50 Subaru clusters. Exactly speaking, although the simulated halos

are not the *same* in detail as the Subaru clusters, other effects such as the intrinsic ellipticities of background galaxies cause much larger variations in the lensing profiles as we will show later. Hence we believe that the catalog of simulated halos is suitable enough for our purpose.

To test our method as well as to simulate the lensing observables from the above N -body simulations, we use the following procedures:

- *3D mass density profile* – We first computed the spherically-average mass profile for each simulated halo, $\rho(r)$, where r is the three-dimensional radius from the halo center. Then we estimated the NFW parameters, M_Δ and c_Δ for $\Delta = 500$, by fitting the model NFW profile (Eq. 2.3) to the mass profile, where we weighted the simulated mass density profile at a given radial bin by the volume of the spherical shell. We stored the best-fit parameters ($M_{500c}^{3D \text{ fit}}, c_{500c}^{3D \text{ fit}}$) for each of the 50 halos.
- *2D lensing profiles* – To simulate the lensing profiles due to a simulated halo, we use the dark matter (N -body) particles inside or surrounding the halo in the simulation output. We estimated the shear profile of each halo by projecting the N -body particles along the line-of-sight direction:

$$\Delta\Sigma(R) = \langle\Sigma\rangle(<R) - \bar{\Sigma}(R). \quad (2.21)$$

Here we chose the z -direction of simulation realization for the projection, and R is the projected radius from the halo center in the xy -plane (the plane perpendicular to the projection direction). $\langle\Sigma\rangle(<R)$ is the averaged surface mass density within a circle of radius R , and $\bar{\Sigma}(R)$ is the averaged surface mass density over the annulus of radius R . In this projection calculation, we used a cubic region containing the halo at the center, whose side length is $20 h^{-1}\text{Mpc}$. Since the shear field arises from the tidal field around a halo, the constant mass density field or the mass density field beyond the cubic region causes a negligible contribution to distortion of background galaxies. We checked that the cubic box is large enough for the range of radii we consider. We included the reduced shear correction to compute the distortion profile of the halo, which is a direct lensing observable:

$$\widehat{\Delta\Sigma}(R) = \frac{\Delta\Sigma(R)}{1 - \Sigma(R)/\Sigma_{\text{cr}}(z_1, z_s)}, \quad (2.22)$$

where $\Sigma_{\text{cr}}(z_1, z_s)$ is the lensing efficiency. In doing so we assign the source and cluster redshifts of each of the 50 Subaru clusters to each simulated halo one by one in descending order of halo masses, where we used the hydrostatic equilibrium mass of X-ray observables in this matching. The assignment of Σ_{cr} becomes relevant when we will include the effect of background shape noise in the Subaru data on the simulated lensing signals of N -body halos. We estimated the NFW profile parameters, $(M_{500c}^{2D}, c_{500c}^{2D})$, by fitting the NFW lensing profile (Eq. 2.16) to the above simulated profile. In this fitting we weighted the lensing profile at each radial bin by the area of radial annulus. We stored the distortion profile, the lensing efficiency function, $\Sigma_{\text{cr}}(z_1, z_s)$, and the best-fit NFW parameters ($M_{500c}^{2D \text{ fit}}, c_{500c}^{2D \text{ fit}}$) for each of the 50 simulated halos.

Figure ?? compares the best-fit NFW parameters, M_{500c} and c_{500c} , estimated by fitting the NFW model to the three-dimensional mass density profile or the two-dimensional lensing distortion profile for each of the 50 simulated halos. The mean halo mass and the range of their halo masses of simulated halos are similar to those of 50 Subaru clusters. Even if we did not include any effect of measurement errors, the NFW parameters inferred from the 3D or 2D fitting generally differ on individual halo basis. For some halos the 2D fitting halo mass is larger than

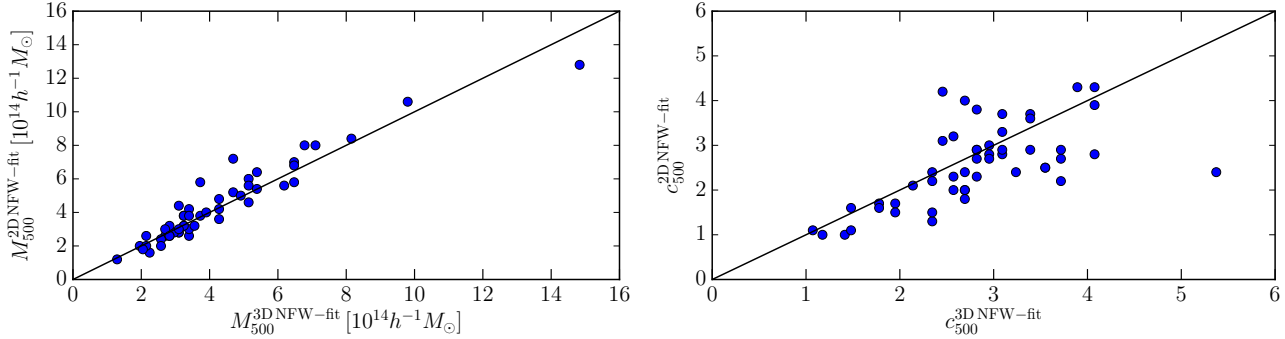


Figure 2.2: Comparison of the best-fit NFW parameters, halo mass and concentration, estimated by fitting the NFW model to the three-dimensional mass density profile (“3D NFW-fit”) or the two-dimensional lensing distortion profile (“2D NFW-fit”), respectively, for the 50 massive halos in N -body simulations of Λ CDM model, respectively

the 3D fitting mass, while the 2D concentration is smaller than the 3D one. These over- or under-estimation would be due to the c - M degeneracy in the NFW fitting.

In Figure 2.3 we performed a hypothetical experiment of the stacked lensing analyses with and without NFW scaling, using the 50 simulated halos. Note that we here ignored shape noise contribution for simplicity. First, the upper-left panel shows the stacked lensing profile as well as the lensing profiles of individual halos, without NFW scaling, i.e. based on the standard method. Again note that we used a fixed range of radial bins, $0.14 \leq R/[h^{-1}\text{Mpc}] \leq 2.8$ as we will do for the real data. The scatters of individual lensing profiles are significant over a range of the radii. Each profile shows various features due to the aspherical mass distribution, in contrast to an analytical, spherical NFW profile. Interestingly, however, the figure shows that the average profile after stacking appears to remarkably well match the NFW profile; the stacked profile and the best-fit NFW profile are almost indistinguishable, on top of each other. For the sake of comparison we plot the amplitudes and the radius relative to the best-fit NFW model of the stacked profile as in Figure 2.1: the best-fit parameters are $M_{500c}^{\text{bf}} \simeq 4 \times 10^{14} h^{-1} M_{\odot}$ and $c_{500c}^{\text{bf}} \simeq 2.50$. These numbers are compared to the averages of their underlying true values: $\langle M_{500c}^{\text{3D fit}} \rangle \simeq 4.38 \times 10^{14} h^{-1} M_{\odot}$, $\langle c_{500c}^{\text{3D fit}} \rangle \simeq 2.76$ or $\langle M_{500c}^{\text{2D fit}} \rangle \simeq 4.56 \times 10^{14} h^{-1} M_{\odot}$ and $c_{500c} \simeq 2.57$. Thus the stacked lensing tends to underestimate the true mass, confirming the claims in the previous work (Mandelbaum et al. 2005; Meneghetti et al. 2010; Becker & Kravtsov 2011; van den Bosch et al. 2013; Meneghetti et al. 2014).

The other three panels show the results with NFW scaling implementation. The lensing profiles of individual halos or the stacked lensing profile are estimated by summing the “scaled” amplitude of lensing distortion in each of the “scaled” radial bin relative to the NFW predictions of each halo (see Eq. 2.17). The different panels are the results when using the best-fit NFW parameters of 3D mass density profile for each halo, the NFW parameters of 2D lensing profile, or the halo mass of 3D profile, but using the concentration parameter inferred from the scaling relation, $c_{500c} = c(M_{500c})$ in DR14, respectively⁴. The lower-right panel is closest to our main results using the Subaru and X-ray data. All the three panels clearly show that the NFW scaling significantly reduces the scatters of individual lensing profiles relative to the NFW prediction,

⁴For the measurement we used the X-ray observables to infer the halo mass of each cluster. Here we assumed that the X-ray observables are sensitive to the inner region of each cluster or relatively less sensitive to the projection effect than in weak lensing. Hence we assume that the X-ray observables gives a proxy of the halo mass via the 3D profile.

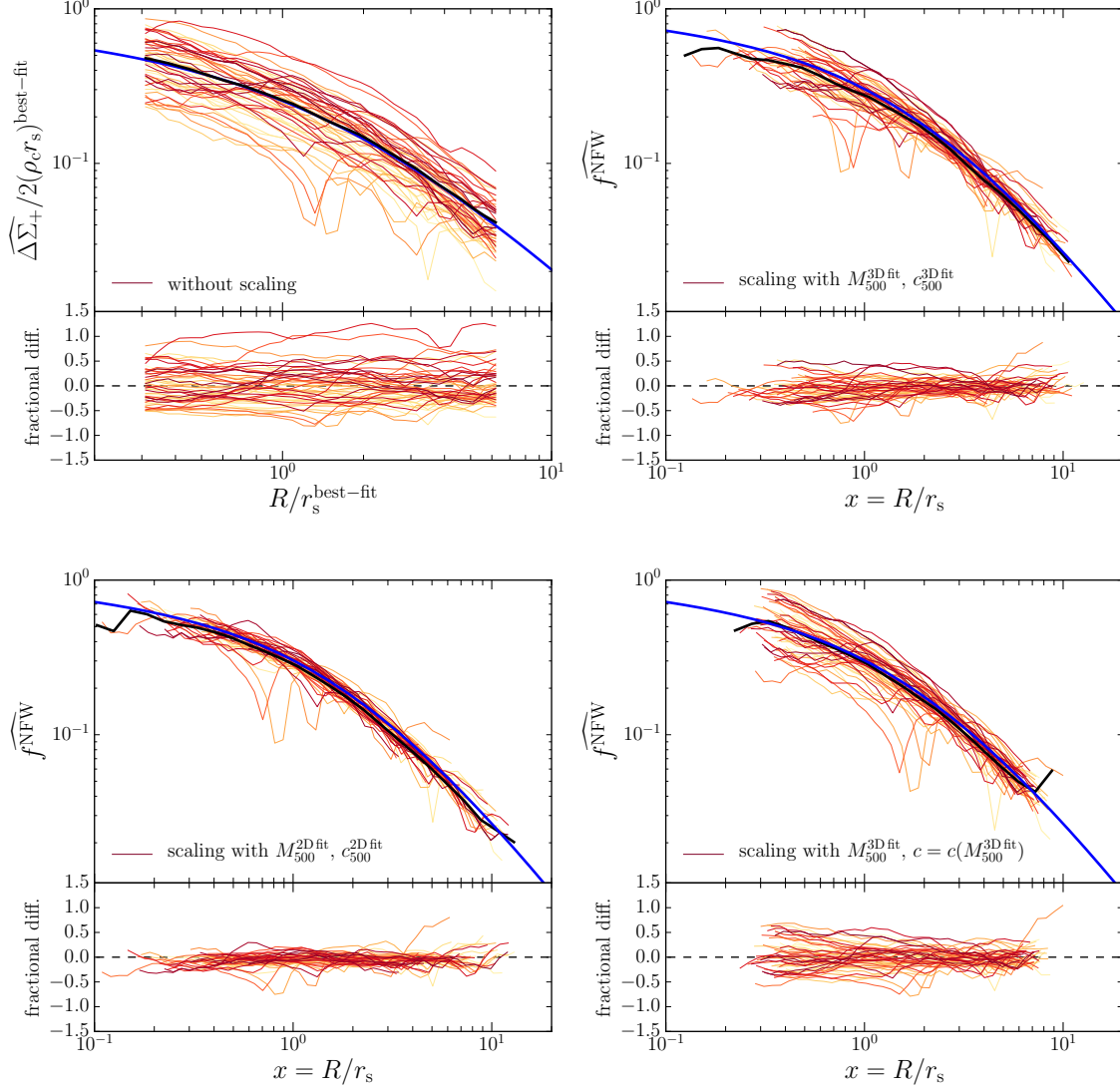


Figure 2.3: Simulated lensing profiles for 50 massive halos in the N -body simulation (see § 2.2.4 for details). *Upper-left panel:* The thin curves show the lensing profiles for each of the 50 halos, and the bold black curve is the stacked lensing profile without NFW scaling. The blue curve is the best-fit NFW profile to the stacked profile. We plot these profiles in dimension-less, so that the quantities in the x - and y -axes can be directly compared to other panels; the “scaled” amplitude, $\widehat{\Delta\Sigma}_+ / (2\rho_c r_s)^{\text{bf-NFW}}$, as a function of the “scaled” projected radius, $R/r_s^{\text{bf-NFW}}$, where we used the best-fit NFW parameters of the stacked profile (blue curve). The lower plot in each panel shows the fractional difference of each profile relative to the best-fit NFW profile. The other three panels show the lensing profiles for the same halos when implementing the NFW scaling for each halo or for the stacked analysis (Eq. 2.17). *Upper-right panel:* The lensing profile when using the NFW parameters of three-dimensional mass profile for each halo, $(M_{500c}^{3D \text{ NFW-fit}}, c_{500c}^{3D \text{ NFW-fit}})$, in the NFW scaling analysis. *Lower-left panel:* The results when using the NFW parameters of two-dimensional lensing distortion profile, $(M_{500c}^{2D \text{ NFW-fit}}, c_{500c}^{2D \text{ NFW-fit}})$. *Lower-right panel:* Similar to the upper-right panel, but using the best-fit halo mass of each halo and using the halo concentration inferred from the scaling relation, $c_\Delta = c_\Delta(M_\Delta; z)$ in DK14. In these three panels, the blue curve is not a fit, but the NFW prediction itself, $f^{\text{NFW}}(x)$ (Eq. 2.7). Note that, for all the results, we ignored effects of measurement errors such as intrinsic ellipticities of background galaxies.

compared to the standard lensing analysis (the upper-left panel). The scatters appear to be smallest when using the best-fit NFW parameters of the 2D lensing profile. Comparing the upper-right and lower-right panels clarifies how the scatters are enlarged due to the lack of halo concentration knowledge on individual halo or shows the degradation by ignoring the intrinsic scatters of halo concentration in different halos. Encouragingly the figure shows that, even without knowledge on the concentration of each halo, the NFW scaling can reduce the scatters compared to the upper-left panel. However it should be noted that the stacked lensing profile shows a sizable deviation from the NFW profile (the blue solid curve), compared to the upper-left panel. In summary these results justify our approach of using the scatters of individual lensing profiles in order to test the universality of mass density profile in 50 clusters.

2.3 Results

2.3.1 The cluster sample

(1) Subaru weak lensing data

To apply the method, described up to the preceding section, to real data, we use the shape catalog of galaxies for 50 massive clusters, used in the work of Okabe et al. (2013). This is the older version of shape catalog, derived as a part of the LoCuSS collaboration (see Okabe et al. 2010a; Martino et al. 2014, for details)⁵. In brief, the 50 cluster sample comprises *all* clusters from the *ROSAT* All Sky Survey catalogs (Ebeling et al. 1998, 2000; Bohringer et al. 2004) that satisfy the criteria given as $L_X[0.1 - 2.4\text{keV}]/E(z)^{2.7} \geq 4.2 \times 10^{44} \text{ erg s}^{-1}$, $0.15 \leq z \leq 0.30$, $n_H < 7 \times 10^{20} \text{ cm}^{-2}$, and $-25^\circ < \delta < +65^\circ$, where $E(z) \equiv H(z)/H_0$ is the normalized Hubble expansion rate. The criteria on the redshift range and the declination are adopted in order to have a sufficiently high elevation of these clusters from the Subaru telescope and to have an entire coverage of the virial region of these clusters with the field of view of the Subaru Suprime-Cam camera (Miyazaki et al. 2002). The cluster sample is complete with respect to this selection function, and thus includes all clusters regardless of their internal structure, thermodynamics, and galaxy populations.

All the clusters were observed by Subaru, with two passbands at least: *i* or I_C data, which is used for the weak lensing analysis, and the bluer-passband data, *V* or *g* data. For this paper we take the position of brightest cluster galaxy in each cluster as the cluster center. Okabe et al. (2010a) carefully studied a possible miscentering effect by comparing the lensing signals of various center proxies such as the X-ray peak, and concluded that the miscentering, even if exists, should be well within 100 kpc in radius (more exactly, within about 50 kpc in our estimate), which is inside the minimum radius used in this paper.

A more problematic uncertainty than the shape measurement error is a possible residual uncertainty in estimation of source galaxy redshifts, mainly limited by the two passband data alone. Okabe et al. (2010a) (also see Okabe et al. 2013) developed a method of making a secure sample of background galaxies, which is selecting galaxies with color sufficiently redder than the red-sequence of early-type galaxies in each cluster region. In other words, they found that it is very difficult to select “blue” background galaxies from the two passband data alone or such blue galaxies always appear to be contaminated by foreground or member (therefore unlensed) galaxies. However, this selection is conservative and leaves only a small number of galaxies in the sample so as to ensure less than 1%

⁵<http://www.sr.bham.ac.uk/locuss/>

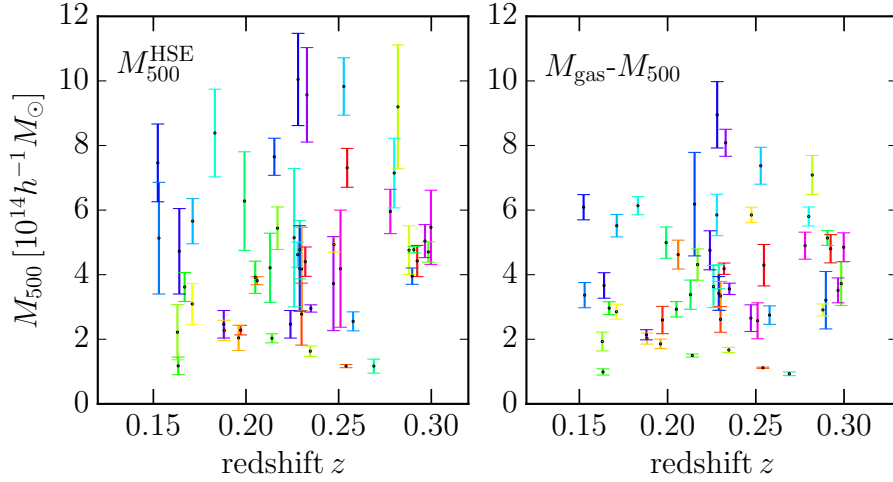


Figure 2.4: The 50 clusters used in this work, in the cluster mass (M_{500c}) and redshift plane. The mass estimate of each cluster was taken from Martino et al. (2014) (see also Table 2.1), derived based on the *Chandra* and/or *XMM* X-ray data. The left panel is the mass estimate based on the hydrostatic equilibrium (HSE) assumption, while the right panel shows the results derived using the scaling relation of X-ray gas mass with halo mass (Eq. 2.24), respectively. The errorbars of each cluster are also taken from Martino et al. (2014) (for $M_{\text{gas},500}$ we propagated the errors of gas mass). Comparing the two panels reveals that the same cluster (symbols at the same x -axis value) generally has different mass estimates and errorbars.

contamination or dilution effect on the lensing signal, even if exists: the mean number density of galaxies is about 5 arcmin^{-2} , a factor 4 or 5 smaller than the number density of all the galaxies usable of weak lensing analysis in the original i - or I_c -band catalog. Hence the measurement errors of weak lensing signals are dominated by the shape noise, which justifies that we ignore the error contribution of projection effects due to different structures along the same line-of-sight to the cluster. The mean redshift of background galaxies in each cluster was estimated by matching color of the selected background galaxies to the COSMOS catalog. Since all the clusters are at low redshift $z \sim 0.2$ and the deep Subaru data typically probe galaxies at $z \sim 0.8$, the lensing efficiency has a weak dependence on source redshift and a possible residual uncertainty in the source redshift would not be large and should be less than a 10% change in the lensing amplitude even if exists (see § 5.7.2 in Okabe et al. 2010a). We should also keep in mind an additional uncertainty in source redshift estimation due to the sample variance in COSMOS calibration catalog, which refers a possible difference in the populations of source galaxies in between the COSMOS and cluster regions.

(2) **X-ray observables : hydrostatic equilibrium mass, gas mass and gas temperature**

All the 50 clusters were observed by the X-ray satellites, *XMM-Newton* or/and *Chandra* (Zhang et al. 2010; Martino et al. 2014). In this thesis, we use the X-ray observables in Martino et al. (2014) to infer the halo mass for each of the 50 clusters, which was estimated based on either or both of the *XMM* and/or *Chandra* data. In the following we will use two mass estimates: the mass estimated based on the hydrostatic equilibrium assumption

(hereafter HSE for simplicity) and the self-similar scaling relation of gas mass (M_{gas}) with the halo mass:

- a) *Hydrostatic equilibrium (HSE) mass* – Martino et al. (2014) carefully developed a method of estimating the HSE mass of each cluster by combining the surface brightness and temperature profiles, measured from the *Chandra* and/or *XMM* data:

$$M(< r) = -\frac{kT_g(r)r}{G\mu m_p} \left[\frac{d \ln \rho_g(r)}{d \ln r} + \frac{d \ln T_g(r)}{d \ln r} \right], \quad (2.23)$$

where $T_g(r)$ and $\rho_g(r)$ are the three-dimensional radial profiles of gas temperature and density, respectively. We will use the halo mass estimate for $\Delta = 500$ overdensity, M_{500c} , in Table 2 of Martino et al. (2014). For some of the clusters, the mass estimates were derived for both the *Chandra* and *XMM* data. If the two mass estimates are available, we use the *XMM*-derived mass because the mass accuracy is better than that of the *Chandra*-based estimate. Note that the two estimates are consistent with each other within the errorbars, We use the *XMM*-based mass for 32 clusters, and use the *Chandra*-based mass for the remaining 18 clusters.

- b) M_{gas} *derived mass* – The direct X-ray observables are the gas mass and temperature. If non-gravitational processes are not significant for cluster evolution, the mass, temperature, size and other properties of galaxy cluster follow self-similar scaling relations (Kaiser 1986). The ratio of the total matter and gas masses in a cluster region is expected to follow the scaling relation: $M_{\Delta}(< r) \propto M_{\text{gas},\Delta}(< r)$. For the interior gas mass, we will use the $M_{\text{gas},500}$ value in Table 3 of Martino et al. (2014) for each cluster. For the normalization factor, we here simply employ the cosmic mean value that is inferred from the latest Planck result (Planck Collaboration et al. 2015):

$$\begin{aligned} \frac{M_{500c}}{10^{14} M_{\odot}} &= \frac{\Omega_{m0}}{\Omega_{b0}} \frac{M_{\text{gas},500}}{10^{14} M_{\odot}} \\ &\simeq 11.6 \times \left(\frac{M_{\text{gas},500}}{10^{14} h^{-3/2} M_{\odot}} \right), \end{aligned} \quad (2.24)$$

where we took the best-fit values of $\Omega_{b0}h^2$, $\Omega_{m0}h^2$ and h in Table 3 of Planck Collaboration et al. (2015) to compute the normalization constant. The unit $h^{-3/2}$ of gas mass is from the fact that the gas mass estimate from X-ray observables has the h -dependence. Note that the overdensity radius r_{500c} used for the interior mass definition is from the total mass profile derived from the HSE assumption, Eq. (2.23). In this sense, exactly speaking, this treatment is not self-consistent. Comparing the above normalization constant with Fig. 2 in Okabe et al. (2014) shows that our model is within a range of the normalization constants implied from observations. However, a precise determination of the normalization constant is not our primary purpose, and the above choice is a working example. We will below study how variations in the above scaling relation change the weak lensing measurements with NFW scaling.

Table 2.1 gives a summary of the above X-ray observables: the HSE mass and the gas mass for each. Figure 2.4 shows the distribution of 50 clusters in the plane of halo mass and redshift. The two proxies give a different estimate of halo mass on individual cluster basis and the error bars quoted are also different. The mean mass of 50 clusters (without

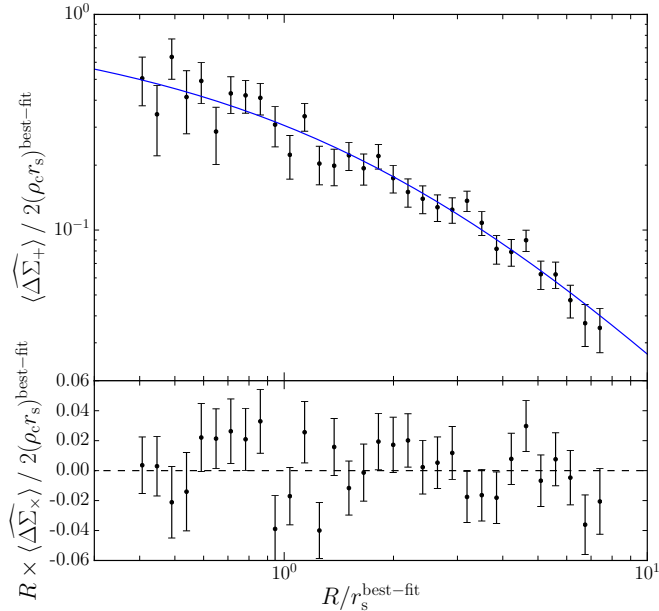


Figure 2.5: *Upper panel:* The stacked distortion profile measured from 50 Subaru clusters, based on the standard stacked lensing analysis (Eq. 2.11). We employed the 32 logarithmically-spaced bins over a fixed range of radii, $0.14 \leq R/[h^{-1}\text{Mpc}] < 2.8$, for all the 50 clusters. The errorbar at each bin is computed from Eq. (2.15) assuming that the statistical noise is dominated by the intrinsic ellipticities of background galaxies. The solid curve is the best-fit NFW model, which is specified by the best-fit parameters $M_{500c} = (4.0 \pm 0.1) \times 10^{14} h^{-1} M_\odot$ and $c_{500c} = 2.8 \pm 0.3$. For the sake of comparison with the following figures, we plot the distortion profile relative to the best-fit NFW model, as a function of the radius relative to the scale radius of the best-fit NFW model. Note that the representative value of each radial bin is estimated from the average of radii of background galaxies that reside in the annulus (see Eq. 2.14). The reduced chi-square for the best-fit model is $\chi^2/\text{d.o.f} = 22.5/(32 - 2)$. *Lower panel:* Similar to the above panel, but for the 45° -rotated components of background galaxy ellipticities.

lensing weights), $\langle M_{500c} \rangle / [10^{14} h^{-1} M_\odot] = 4.42$ or 3.82 for the HSE or gas mass proxy, respectively. Note that we will later discuss how possible intrinsic scatters of the mass and X-ray observable relation affect our results.

2.3.2 The stacked lensing analysis of 50 clusters with and without NFW scaling

First of all, in Figure 2.5, we show the stacked lensing profile of 50 clusters, without NFW scaling, for the sake of comparison with the following results. This result reproduces Figure 3 in Okabe et al. (2013). We employed 32 logarithmically-spaced bins over the radial range of $0.14 \leq R/[h^{-1}\text{Mpc}] \leq 2.8$. As given by Eq. (2.14), we estimated the representative value of each radial bin by averaging the centric-radii of background galaxies in the annulus, and therefore the neighboring bins are, exactly speaking, not equally spaced, although the difference is very small after the average of 50 clusters. The cumulative signal-to-noise ratio is significant: $S/N \simeq 34.5$. From the fitting to an NFW profile, we find the best-fit parameters, $M_{500c} = (4.0 \pm 0.1) \times 10^{14} h^{-1} M_\odot$ and $c_{500c} = 2.8 \pm 0.3$, respectively. The reduced chi-square is $\chi^2/\text{d.o.f} = 22.5/(32 - 2)$. Thus the results show that, even if the range of the X-ray inferred masses span over more than a factor 10, the stacked profile is so remarkably well fitted by the NFW model. This appears to

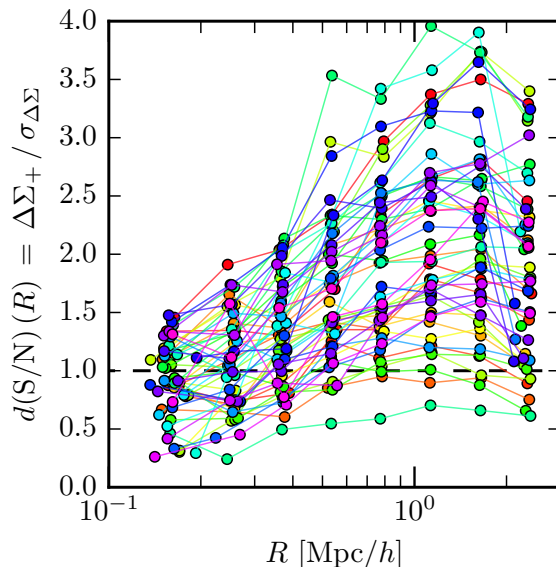


Figure 2.6: The expected, differential signal-to-noise ratio, $d(S/N)$, at each of the 8 logarithmically-spaced radial bins in the range $0.14 \leq R/[h^{-1}\text{Mpc}] \leq 2.8$, for each of 50 Subaru clusters. We computed the $d(S/N)$ value as follows. For the expected signal, we used an analytical NFW profile assuming the X-ray HSE mass and the halo concentration inferred from the $c - M$ relation in DK14. To compute the statistical noise in each bin, we used the real Subaru data of background galaxies (their distribution on the sky, the intrinsic shapes and the lensing weights) in each cluster region. This figure suggests that about 79% of 400 data points ($400 = 50 \times 8$), are expected to have the $d(S/N)$ values greater than unity. Note that the representative value of each radial bin is computed from Eq. (2.14) taking into account the radii and weights of background galaxies, which causes variations in the representative values especially for the small radii, even if we work on the fixed range of $0.14 \leq R/[h^{-1}\text{Mpc}] \leq 2.8$.

be consistent with what we found from the test using the simulated halos in Figure 2.3.

Next we employ the following procedures to implement the NFW scaling analysis of weak lensing measurements:

- (1) *NFW scaling of galaxy ellipticities and radial bins* – First, we employ, for the a -th cluster ($a = 1, 2, \dots, 50$), the halo mass inferred from the X-ray observables, either HSE or gas mass (see § 2.3.1). We then use the c - M relation in DK14 to infer the halo concentration for the cluster. Using the X-ray inferred parameters, $M_{500(a)}^X$ and $c_{500(a)}^X$, we compute the expected lensing amplitude and the NFW scale-radius, $2[\rho_c r_s]_{(a)}$ and $r_{s(a)}$, respectively, in order to “scale” the amplitude of galaxy ellipticities as well as the radius for each i_a -th background galaxy in the a -th cluster region: $e_{+(i_a)} \rightarrow e_{+(i_a)}/[2\rho_c r_s]_{(a)}$ and $R_{(a)i_a} \rightarrow x = R_{(a)i_a}/r_{s(a)}$. Thus, even if we use the same background galaxies over a fixed range of radii, $0.14 \leq R/[h^{-1}\text{Mpc}] \leq 2.8$, this NFW scaling leads to different ranges of the scaled radii, x , for different clusters. The different amount of radial scaling requires a careful treatment of the radial binning, especially when comparing the lensing distortion profiles with and without NFW scaling. In the following we use the different binning schemes depending on either case studying the stacked lensing profile or studying the scatters of 50 cluster lensing profiles relative to the NFW prediction, which are summarized by the procedures (2a) and (2b) below.

- (2a) *Stacked lensing analysis with NFW scaling implementation* – As in Figure 2.5, we will study

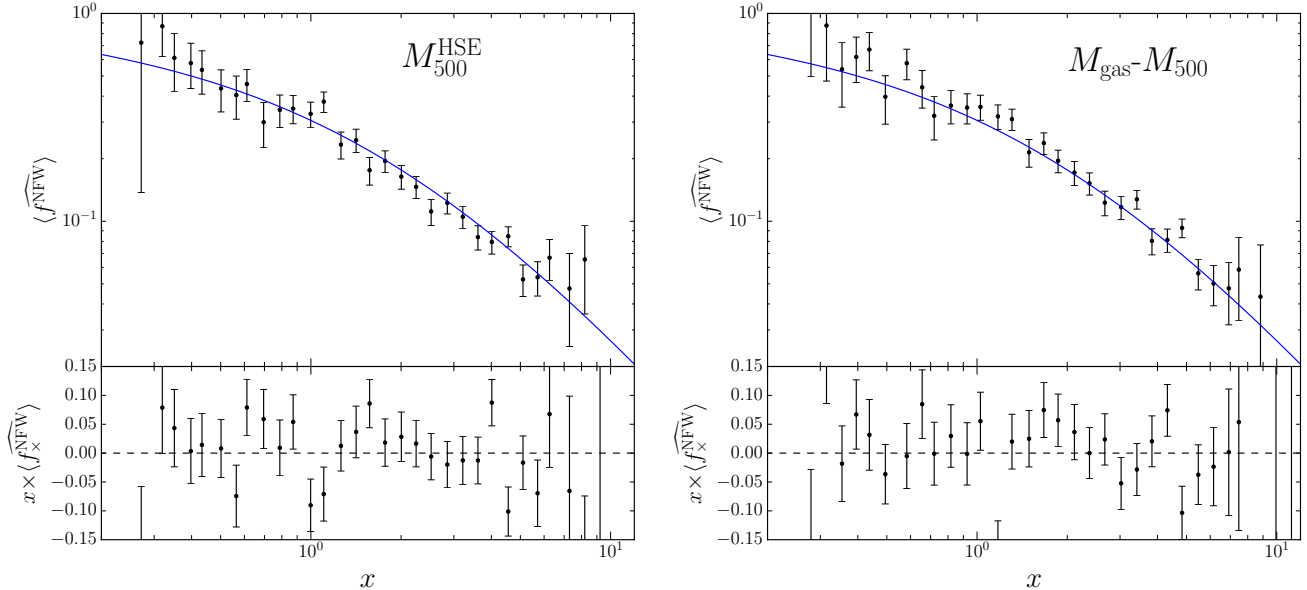


Figure 2.7: The stacked distortion profile of 50 clusters when implementing the NFW scaling analysis: we summed the “scaled” amplitudes of background galaxy ellipticities in each bin of the “scaled” radii according to the NFW parameters, halo mass and concentration, inferred for each cluster based on its X-ray observables. In the left or right panels, we employed the X-ray inferred mass of each cluster from the hydrostatic equilibrium assumption (HSE) or the gas mass, respectively, and then used the halo concentration inferred from the scaling relation $c = c(M; z)$ in DK14. Note that we used exactly the same background galaxies as those for the analysis without NFW scaling in Figure 2.5. The errorbar at each bin is computed based on Eq. (2.18). The solid curve in each panel is *not* a fit, but the NFW prediction (f^{NFW} given by Eq. 2.7) including a small correction due to reduced shear at the small radii (see below Eq. 2.17). The reduced chi-square is $\chi^2/\text{d.o.f} = 31.3/32$ or $30.7/32$ for the HSE or gas mass case, respectively.

the stacked distortion profile of 50 clusters after the NFW scaling of each cluster. Similarly to Figure 2.5, we will use the 32 logarithmically-spaced bins in the “scaled” radius, x , where we used exactly the same background galaxies behind the 50 clusters. After stacking 50 clusters, we can expect a significant detection of the lensing signal at each radial bin, as implied from Figure 2.5. However, the above NFW scaling transforms the original radial range to a different range of the scaled radius x . Hence, the sample of background galaxies in each bin of R or x radii differ from each other. Since the stacked lensing has a sufficiently high S/N at each bin, we checked that the NFW scaling almost conserves the total S/N value (exactly speaking, it causes only about 0.5% fractional change). Note that we estimate the representative value of each radial bin in a similar manner to Eq. (2.14).

- (2b) *Studying the scatters of lensing profiles for 50 clusters* – As we discussed in § 2.2.3, we monitor the scatters of 50 cluster lensing profiles relative to the NFW prediction in order to address the existence of the universal NFW profile. To quantify the scatters, we compute the d^2 value for either case with or without NFW scaling (see Eqs. 2.19 and 2.20 for the definition). In doing this, we need to probe the “shape” of lensing profile for each cluster, and in other words each radial bin needs to be in the signal dominated regime on individual cluster basis. Hence, if we take the 32 bins as in the stacked lensing analysis,

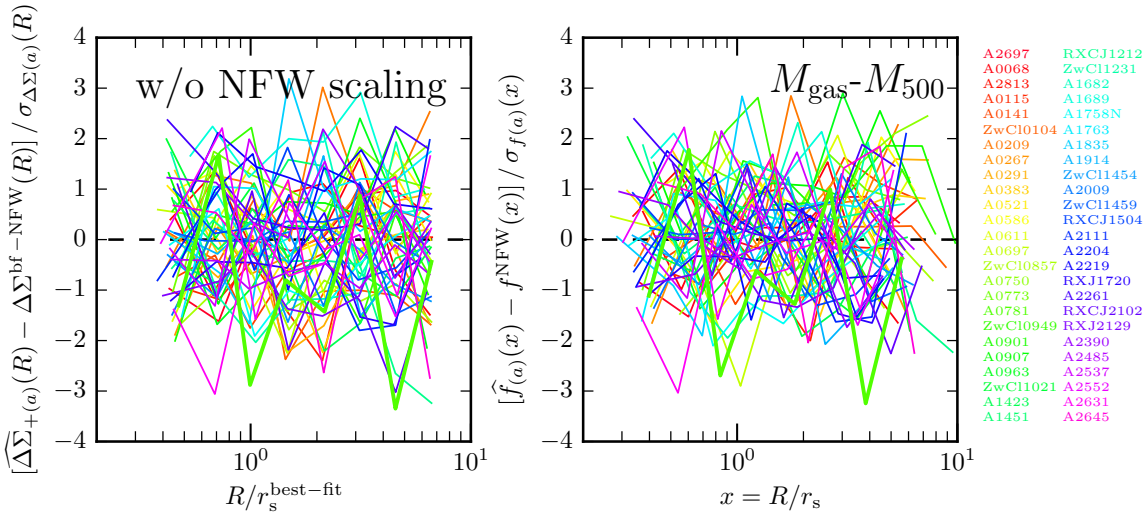


Figure 2.8: The difference between the lensing distortion profiles of 50 clusters and the best-fit NFW profile ($\Delta\Sigma^{\text{best-fit}}(R)$) or the normalized NFW profile ($f^{\text{NFW}}(x)$) for the weak lensing analysis with or without NFW scaling implementation in the left or right panel, respectively. The right panel shows the result when using the gas mass to estimate the halo mass of each cluster. To make a comparison, we show the relative difference to the statistical error at each radial bin (see Eqs. 2.19 and 2.20). Since the lensing profile is noisy on individual cluster basis due to the fewer number of background galaxies, we employed the 8 logarithmically-spaced bins in the fixed range of $0.14 \leq R/[h^{-1}\text{Mpc}] \leq 2.8$ for all the clusters as in Figure 2.6. In addition, we used the same background galaxies in each radial bin before and after the NFW scaling transformation, $x = R/r_s$, for each cluster so that the differences become identical if we set the model NFW profile $\Delta\Sigma^{\text{bf-NFW}} = f^{\text{NFW}} = 0$ (see the procedure 2b in § 2.3.2 for details). Also note that, due to the NFW scaling, the fixed radial range in the left panel is transformed to the different range of the scaled radius for different clusters. The same-color curves in the two panels correspond to the same cluster, and the bold curve shows, as an example, the result for A781, which has the largest deviation from the NFW profile. The sum of squares of all the curves gives an estimate to quantify the scatters of 50 cluster lensing profiles relative to the NFW model – here we call the d^2 value. The NFW scaling yields $d^2 = 527.1$ or 504.6 for the HSE and gas mass cases, respectively, compared to $d^2 = 543.2$ for the case without NFW scaling (Figure 2.5). This corresponds to the improvement $\Delta d^2 = d^2 - d_{\text{w-scaling}}^2 = (4.0)^2$ or $(6.2)^2$, respectively.

each radial bin suffers from the shape noise contamination due to too low number density of background galaxies in each bin. To tackle this trade-off between a finite number of radial bins and the small lensing signals, we employ 8 logarithmically-spaced bins in the range $0.14 \leq R/[h^{-1}\text{Mpc}] \leq 2.8$ for each cluster. Figure 2.6 shows the expected S/N at each radial bin for the 50 clusters. The figure shows that 319 data points among 400 points, corresponding to 79% of 400 data points, are expected to have the S/N value greater than unity. Hence the 8 bins seem suitable for our purpose. Table 2.1 gives the total S/N of each cluster when employing the 8 bins. However, the expected lensing signal at each radial bin would be still noisy. To avoid any artifact arising from the noise dominated bins, we transform each of the original bins in R to the corresponding bin in the scaled radius x after the NFW scaling, rather than redefining the radial bins for a fixed range of x . With this binning, each radial bin before and after the NFW transformation preserves the same background galaxies. Hence, this binning method preserves the S/N value in each radial bin as well as the total S/N value for each cluster, before and after the NFW scaling, as

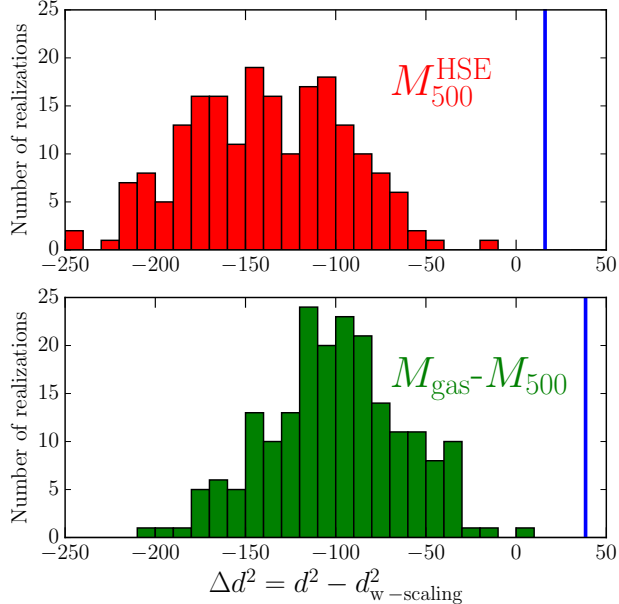


Figure 2.9: A test of the performance of the NFW scaling analysis in Figure 2.7. We randomly assigned the X-ray inferred mass to each cluster, redid the scaling analysis, and then computed the d^2 difference (Eq. 2.25), where the d^2 -value quantifies the scatters of 50 cluster lensing profiles relative to the NFW profile as shown in Figure 2.8. The histogram shows the distribution of 200 random realizations, which can be compared to our main result shown by the vertical line for either the HSE mass or the gas mass case in the upper or lower panels, respectively. All the random realizations give a negative value of Δd^2 , and any of those does not reproduce the measurement value. Compared to the mean and variance of the random realizations, the measured Δd^2 value is away from the mean at 3.6 and 3.7σ for the HSE and gas mass cases, respectively.

can be found from Eqs. (2.19) and (2.20) mathematically. As a result, the different clusters cover different ranges of the scaled radius x .

Figure 2.7 shows the stacked lensing profiles after implementing the NFW scaling (the above case 2a), using the halo mass proxies based on the HSE assumption or the gas mass, respectively. We again note that, to have a fair comparison with Figure 2.5, we have used exactly the same background galaxies. The solid curve in each panel is *not* a fit, but rather is the NFW prediction (Eq. 2.7), including the reduced shear correction $1/[1 - \kappa^{\text{NFW}}(x)]$, where we used the best-fit NFW model to the stacked distortion profile in Figure 2.5. The reduced shear correction is not large (by up to 20% in the amplitude) over the range of radii, as can be found from Figure 2.1. The figure shows that the stacked profile is in excellent agreement with the NFW prediction, to within the errorbars. This agreement supports the existence of NFW profile in the clusters, and implies that the X-ray inferred mass indeed gives a proxy of the genuine mass for each cluster. To be more precise, the reduced chi-square is $\chi^2/\text{d.o.f} = 31.3/32$ or $30.7/32$ for the HSE or gas mass case, respectively, compared to $\chi^2/\text{d.o.f} = 22.5/(32 - 2)$ in Figure 2.5.

We compare the scatters of 50 cluster lensing profiles with and without implementation the NFW scaling, quantified by the d^2 value (Eqs. 2.19 and 2.20), in order to address the existence of *universal* NFW profile. By using the above method (2b), we find the difference between the

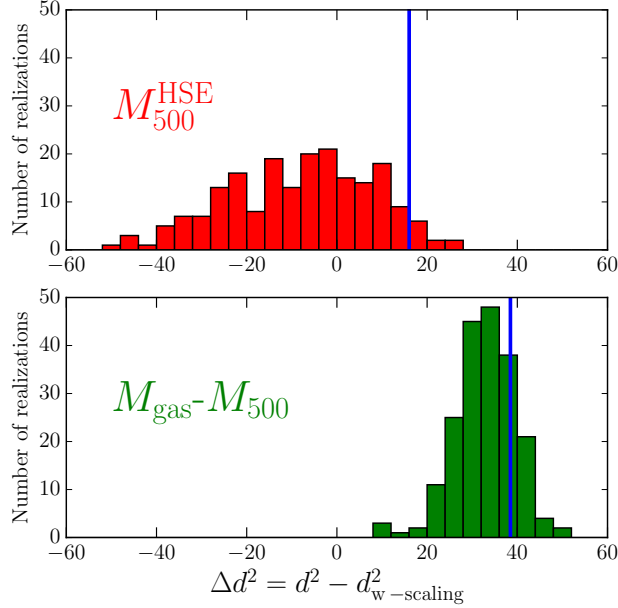


Figure 2.10: As in the previous figure, but show effects of the statistical errors in X-ray inferred halo mass of each cluster on the Δd^2 value. Here, we added a random scatter to each halo mass by an amount of the quoted errorbar in Table 2.1 assuming the Gaussian distribution, redid the weak lensing analysis with NFW scaling, and then computed the Δd^2 value for each realization.

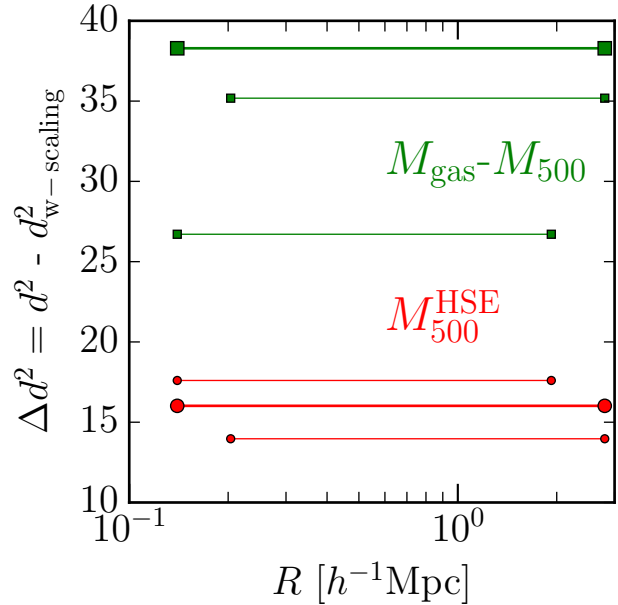


Figure 2.11: The change in Δd^2 (the vertical axis) when using the different range of radii (the horizontal axis) in the scaling analysis. The bold lines are the results for our fiducial choice: $0.14 \leq R/[h^{-1}\text{Mpc}] \leq 2.8$ and 8 logarithmically-spaced bins for all the 50 clusters. The other lines are the results when excluding the innermost or outermost bin from the analysis, respectively for the the HSE or gas mass proxy cases.

d^2 values with and without NFW scaling as

$$\begin{aligned}
 \Delta d^2 &\equiv d^2 - d_{\text{w-scaling}}^2 \\
 &= \begin{cases} 543.2 - 527.1 \simeq (4.0)^2, & (\text{HSE}) \\ 543.2 - 504.6 \underset{35}{\simeq} (6.2)^2, & (M_{\text{gas}} - M_{500c}) \end{cases} \quad (2.25)
 \end{aligned}$$

Thus the NFW scaling for both the HSE and gas mass cases leads to the smaller d^2 -values, meaning the smaller scatters of lensing profiles relative to the NFW profile than the scatters without NFW scaling. The smaller d^2 value for the gas mass implies that the gas mass gives a better proxy of the underlying true masses of clusters (at least the relative mass differences between different clusters). Thus the NFW scaling gives about 4- or 6- σ improvement for the HSE or gas mass, respectively, assuming that the d^2 distribution obeys a χ^2 -distribution. We checked that, even if we use 16 bins instead of our fiducial 8 bins, the d^2 values themselves get enlarged because each bin is more in the shape noise dominated regime, but the d^2 difference, the Δd^2 value, is not largely changed.

The improvement in the d^2 value due to the NFW scaling arises from two parts: the scaling of lensing profile amplitude (or background galaxy ellipticities) and the scaling of cluster-centric radius. The two scalings are specified by halo mass and concentration of each cluster: $e_+[2\rho_c r_s] \propto M_{500c}^{-1/3} c_{500c}^{-2}$ and $x = R/r_s \propto M_{500c}^{-1/3} c_{500c}$, respectively. If we include only the scaling of background galaxy ellipticities, without the radial scaling, we found $d_{w\text{-scaling}}^2 = 512.9$ or 526.5 for the HSE or gas mass case, which equivalently correspond to $\Delta d^2 \simeq (5.5)^2$ or $(4.1)^2$, respectively. That is, the HSE case shows an even greater improvement in Δd^2 compared to Eq. (2.25). On the other hand, if we include only the scaling of radius, but without the scaling of galaxy ellipticities, $d^2 = 547.1$ or 522.3 , which correspond to $\Delta d^2 \simeq -3.9$ or $(4.6)^2$, respectively. Thus, for the HSE case, the radial scaling does not appear to be adequate, and rather gives a positive Δd^2 . For the gas mass case, both the two scalings about equally contribute to the improvement.

Figure 2.8 shows the contribution of each cluster to the d^2 -value, which shows the argument of Eqs. (2.19) or (2.20) at each radial bin for each of 50 clusters. The total d^2 value is obtained by summing the square of each curve over the 8 radial bins and 50 clusters. Table 2.1 gives the total d^2 -value for each cluster. The figure shows that, although it looks noisy, the NFW scaling reduces the scatters. One might notice some outlier clusters: the clusters, which have top three largest $d_{w\text{-scaling}}^2$ values (see Table 2.1), are A781, A209, and A697 for the HSE case, while A781, A2645 and A750 for the gas mass case, respectively.

To draw a more robust conclusion, we make several tests of our results. In Figure 2.9, we studied how the scatters of 50 lensing profiles are enlarged if we implement the NFW scaling analysis by randomly assign the X-ray inferred halo mass to each cluster (without repeated use of X-ray mass). All the 200 random realizations have a negative value of Δd^2 , and any of the random realizations cannot reproduce a similar positive value to the measured Δd^2 (the vertical line) for both the HSE and gas mass cases. To be more quantitative, the measured value Δd^2 is away at 3.6 and 3.7 σ for the two cases, respectively, compared to the mean and variance of the random realization distribution. These results give another support on the existence of NFW profile in the 50 clusters.

One important source of uncertainties in the method is a residual uncertainty in the X-ray inferred halo mass or a possible effect of intrinsic scatter in the mass scaling relation of X-ray observable. Figure 2.10 shows how the statistical errors of X-ray inferred mass affect the Δd^2 value. To be more precise, we added a random scatter to halo mass of each cluster assuming the Gaussian distribution with variance given by the quoted errorbar of each X-ray mass in Table 2.1, i.e. $M'_{500(a)} = M_{500(a)}^X + \delta M_{(a)}$, treated the shifted mass as its true mass, and then redid the NFW scaling analysis. The figure shows that adding the random scatter to each cluster tends to decrease Δd^2 , implying that the central value of the X-ray inferred mass is indeed closer to the underlying true mass. The distribution of Δd^2 is wider for the HSE mass, but this would be ascribed to the larger errors of HSE mass than those for the gas as can be found from Figure 2.4. Again encouragingly, even if adding the random errors to the gas mass, the resulting Δd^2 values

are positive, supporting that the gas mass is a better proxy of the genuine cluster mass as in Figure 2.7.

Although we have used the fixed range of the original comoving radius, $0.14 \leq R/[h^{-1}\text{Mpc}] < 2.8$, for all the clusters as our fiducial choice, Figure 2.11 shows how the results are changed if excluding the inner- or outer-most radial bin of 8 logarithmically-spaced bins from the analysis. The figure shows that, for the X-ray gas mass proxy, excluding the outer- or inner-most bin degrades the NFW scaling or reduces the Δd^2 values, suggesting that the wider range of radii is important to capture the curvature of the mass profile. On the other hand, for the HSE mass case, excluding the outermost bin increases the Δd^2 , again implying that the HSE mass estimate might not be as accurate to infer the genuine mass as the gas mass and involve residual systematic errors.

2.3.3 Discussion and Implications: Comparison with N-body simulations

From a viewpoint of Λ CDM structure formation model, Figure 2.12 compares the measurement results and the N -body simulated halos, as in Figure 2.3, in a two-dimensional space of the d^2 values with and without NFW scaling. To make a fair comparison, we included the effect of intrinsic galaxy ellipticities on the simulation results. To be more precise, (1) we first populated, into each region of simulated halos, the background galaxies taken from the corresponding Subaru cluster data (matched in descending order of halo masses), (2) made a random rotation of orientation of each galaxy ellipticity, which erases the coherent lensing signal of each Subaru cluster, and (3) then computed the d^2 values after simulating the “observed” galaxy ellipticities including both the intrinsic shapes and the lensing distortion of simulated halo. To account for the statistical variance of intrinsic ellipticities, we generated 40 realizations of the N -body simulation results: we redid the d^2 calculations after random rotation of background galaxies. For the simulation results, we consider the three cases similarly to Figure 2.3: the lensing analysis with NFW scaling when using the best-fit NFW parameters of 3D mass profile, the NFW parameters of 2D distortion profile, or the best-fit halo mass of 3D profile, but using the halo concentration inferred from the c - M relation, respectively. The third case is closest to what we did for the actual data. First of all, the simulation results without NFW scaling, denoted by the d^2 values in the horizontal axis, fairly well reproduce the measurements on average, reflecting that the statistical errors in the d^2 value are dominated by the shape noise. Also note that the horizontal spread of the simulation realizations is roughly given by $\sqrt{d^2} \simeq \sqrt{550} \simeq 23$. However, all the simulation results with NFW scaling, $d_{\text{w-scaling}}^2$ in the vertical axis, are systematically smaller than the measured values. Thus this disagreement suggests that we do not properly consider some effects inherent in the measurements on the simulation results. For comparison, the star symbols show the results when using analytical NFW halos to compute the d^2 values where we used the X-ray proxy masses for the HSE or the gas mass to compute the NFW lensing profile of each cluster. The difference between the analytical NFW halos and the simulation results is due to the complexity of mass distribution in the simulated halos, such as asphericity, substructures, and the scatters of halo concentration.

A possible source to reconcile the difference between the measurements and the simulation results in Figure 2.12 is an additional error or intrinsic scatter in the X-ray inferred halo mass (Stanek et al. 2010; Okabe et al. 2010b). Figure 2.13 addresses this question. The left panel shows how adding a scatter to each mass of simulated halos, parametrized by the fractional variance $\sigma_{\ln M} = \sigma(M)/M = 0.1, 0.2$ or 0.3 , degrades the $d_{\text{w-scaling}}^2$ values for the NFW scaling

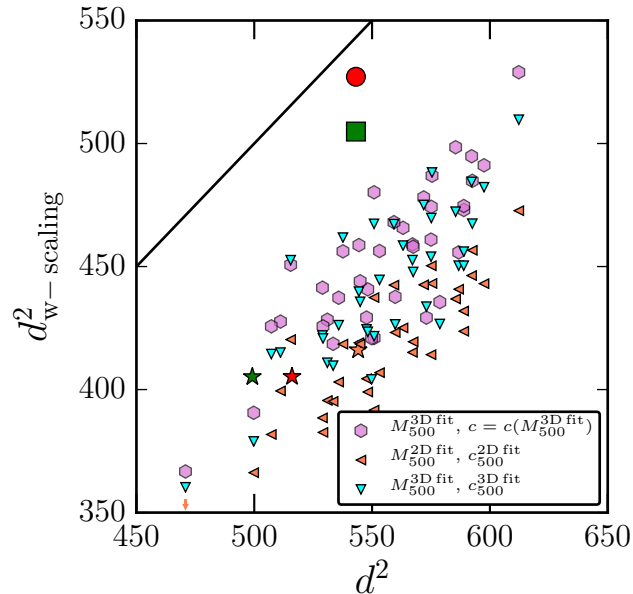


Figure 2.12: Comparison of the measurements and the simulation results for the d^2 -values. (Eqs. 2.19 and 2.20 for their definitions). The bigger-size circle and square symbols are the measurement results for the HSE and gas mass cases, respectively. The other symbols are the simulation results for 40 realizations, combining the N-body halo profiles and the effect of intrinsic ellipticities of background galaxies that are taken from actual Subaru data of each cluster region. The tilted triangle and hexagon symbols are the simulation results; triangles are cases with the best-fit NFW parameters of 3D mass profile for each halo, and the NFW parameters of 2D projected lensing profile. The hexagon symbols are intended to mimic what we did for the actual measurements, using the best-fit mass of 3D profile, and the concentration inferred from the scaling relation $c_{\Delta} = c_{\Delta}(M_{\Delta}; z)$, respectively. (see Figure 2.3 for details). We show the simulation results for 40 realizations of background galaxy ellipticities. Note that, for each realization, we computed the three simulation results; each of the triangle and hexagon symbols with same d^2 value in the horizontal axis, but different $d^2_{w\text{-scaling}}$ values in the vertical axis. For comparison, the orange-color star symbol denotes one particular realization that has a similar d^2 value to the measurement for no NFW scaling case (the vertical axis). The two star symbols in the left-lower corner are the results when using the same realization of background galaxies as in the orange-color star symbol, but using the analytical NFW profiles for the d^2 calculations. Note that the arrow in the lower-left corner denotes the simulation result that is below the plotted range.

analysis. More precisely, we randomly generated a mass scatter δM for each halo assuming the Gaussian distribution with variance $\sigma_{\ln M}$, added the scatter to each halo mass as given by $M'_{(a)} = M_{500(a)}^{2D \text{ fit}} + \delta M$, and then computed the $d^2_{w\text{-scaling}}$ value by treating the shifted mass M' as the true mass of each simulated halo. For the sake of comparison, we used the same 40 realizations of background galaxies as in Figure 2.12, and therefore the degradation is solely due to the mass scatters. Note that, for each realization of background galaxies, adding the halo mass scatters changes only the $d^2_{w\text{-scaling}}$ value in the vertical axis. The figure shows that the halo mass scatters generally degrades the NFW scaling result or equivalently enlarge the $d^2_{w\text{-scaling}}$ value. However, only the additional errors of $\sigma_{\ln M} \sim 0.2\text{--}0.3$ can reproduce the measurement result for the gas mass proxy. This might imply that the X-ray halo mass involves an unknown, systematic error or intrinsic scatter.

As an alternative test, the right panel of Figure 2.13 shows the effects of the quoted error-

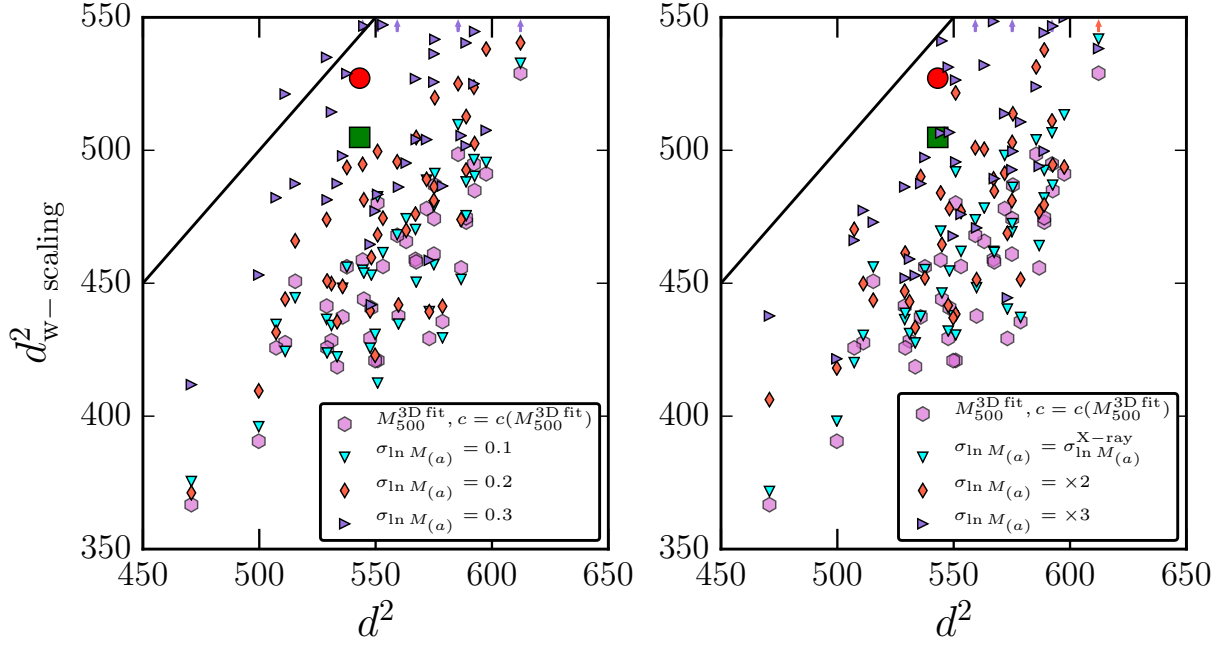


Figure 2.13: d^2 plot with the effects of mass scatter of each halo on the simulation results. The hexagon symbols are the same as in Figure 2.12. For each realization of background galaxies, we added a random mass scatter to each halo, simulated the lensing analysis with NFW scaling by treating the shifted mass as the true mass, and then computed the $d^2_{w\text{-scaling}}$ value. Adding the halo mass scatters tends to degrade the NFW scaling results or preferentially causes an up-scatter of each simulation result in this two-dimensional space. *Left panel:* The simulation results when adding the Gaussian mass scatters by the fractional errors of $\sigma_{\ln M} = 0.1, 0.2$ or 0.3 , respectively. The arrows in the upper horizontal axis denote the case that the simulation results are outside the range shown in this plot. *Right panel:* The results when adding a random mass scatter to each simulated cluster assuming the fractional error proportional to the quoted error of the gas mass proxy relation ; $\sigma_{\ln M(a)} \equiv \sigma_{M(a)}^X / M(a)^X$ or a factor 2 or 3 bigger one.

bars in the X-ray inferred halo masses. Here we added a random mass scatter to each cluster, $M'_{(a)} = M_{500(a)}^{2D \text{ fit}}(1 + \delta \ln M)$ by taking the fractional mass error, $\sigma(M_{(a)}^X) / M_{(a)}^X$, for each cluster (see Table 2.1) assuming the Gaussian distribution, and then computed the $d^2_{w\text{-scaling}}$ value for each realization. Here we used the mass errors for the gas mass proxy in Table 2.1. Note that the mean fractional error of 50 clusters is about 0.11, but here we included variations in the errors for different clusters. The figure shows that, if each cluster has a factor 2–3 larger mass error than the quoted error, the simulation results appear to reproduce the measurements. The mass errors of X-ray observables might underestimate the genuine mass uncertainty, perhaps due to the limitation of the X-ray based method or due to an unknown intrinsic scatter in the X-ray observable and halo mass relation.

2.3.4 The halo mass proxy relation of X-ray observables

The method we have so far developed involves several assumptions. For instance, to implement the lensing stacking with NFW scaling, we need to assume several scaling relations: the halo mass proxy relation of X-ray observables and the halo mass and concentration relation. In the following we address how possible variations in these scaling relations affect the NFW scaling

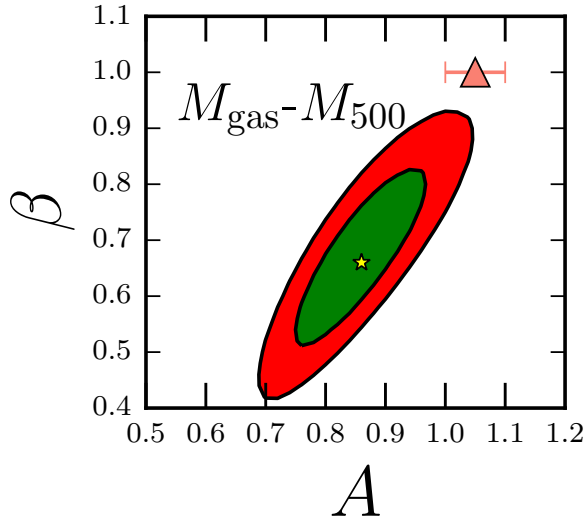


Figure 2.14: Effects of variations in the halo mass proxy relation of X-ray gas mass on the NFW scaling results. We model the variations as $M_{500c}/[10^{14}M_{\odot}] = A \times 11.6 \times (M_{\text{gas}}/10^{14}h^{-3/2}M_{\odot})^{\beta}$, where $A = 1$ and $\beta = 1$ are our fiducial model corresponding to the self-similar scaling model. We estimated the best-fit parameters (the star symbol) by minimizing the d^2 value with varying the normalization and mass slope parameters. The two contours correspond to the regions satisfying the conditions $\Delta d^2 = d_{\text{w-scaling}}^2(A, \beta) - d_{\text{w-scaling}}^2(A^{\text{best-fit}}, \beta^{\text{best-fit}}) = 2.3$ or 6.17, respectively. The triangle symbol with errorbar denotes the result when varying the normalization parameter A alone, with fixing $\beta = 1$.

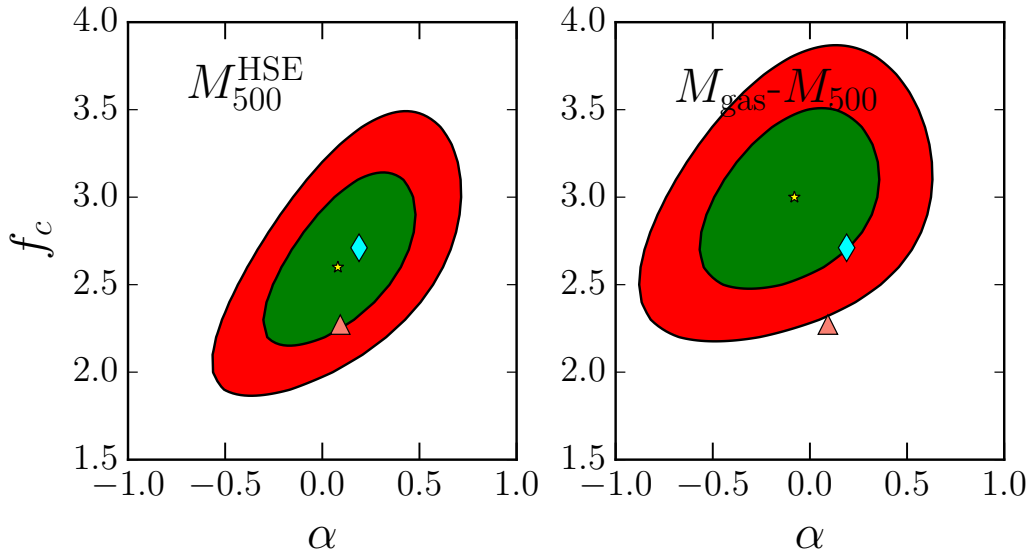


Figure 2.15: Similar to the previous figure, but effects of variations in the halo mass and concentration relation on the NFW scaling results, for the HSE and gas mass cases, respectively. Here we parametrized the variations as $c(M) \propto M^{\alpha}$ (Eq. 2.28), and then minimized the d^2 -value with varying the normalization and mass slope parameters. The diamond symbol in each panel shows the parameters for our fiducial model DK14 at the mean redshift of clusters, $z = 0.23$, while the triangle symbol denotes the parameters of Duffy et al. (2008).

results.

First we study a possible bias in the X-ray inferred halo mass. To address this we simply introduce the calibration factor, $M_{(a)}^{X,\text{corr}} = AM_{(a)}^X$, assuming the same constant factor A for all the 50 clusters. $A = 1$ corresponds to no bias between the X-ray and lensing inferred masses, on average sense of 50 clusters. We then repeat the NFW scaling analysis by varying the calibration factor A . Here we consider the two approaches, (1)–(2a) or (1)–(2b), in § 2.3.2. When minimizing the $d_{\text{w-scaling}}^2$ value with varying A , we find

$$\begin{aligned} A^{\text{HSE}} &= 0.88 \pm 0.04 & (d_{\text{w-scaling}}^2 &= 517.9) \\ A^{M_{\text{gas}}} &= 1.05 \pm 0.05 & (d_{\text{w-scaling}}^2 &= 503.6), \end{aligned} \quad (2.26)$$

compared to $d_{\text{w-scaling}}^2 = 527.1$ or 504.6 for the fiducial model ($A = 1$), respectively. The errorbars are taken from $d_{\text{w-scaling}}^2(A = 1) - d_{\text{w-scaling}}^2(A^{\text{best-fit}}) \leq 1$. Thus adding the normalization parameter in the halo mass proxy relation of X-ray observables slightly improves the NFW scaling results. Although we employed a crude assumption of the halo mass proxy relation, our method would offer a new new method to determine the underlying scaling relation. This is complementary to the standard method which is done by comparing the X-ray observables and the lensing inferred mass estimate on individual cluster basis (Okabe et al. 2010b; Mahdavi et al. 2013; Okabe et al. 2014).

We further introduce another free parameter to allow the halo mass dependence in the X-ray mass proxy relation in addition to the normalization parameter; i.e., we parametrize the halo mass proxy relation as

$$\frac{M_{500}^X}{10^{14}M_{\odot}} = A \times 11.6 \times \left(\frac{M_{\text{gas}}}{10^{14}h^{-3/2}M_{\odot}} \right)^{\beta} \quad (2.27)$$

Then we perform the NFW scaling analysis with varying the two parameters, A and β , simultaneously. Figure 2.14 shows the constraint regions in the two parameter space. Here we minimize the d^2 value with varying A and β . The best-fit scaling model gives and $d_{\text{w-scaling}}^2 = 493.8$ (about 3.3σ improvement from the fiducial model). The best-fit parameters $A = 0.86 \pm 0.06$ and $\beta = 0.66 \pm 0.10$, where we quoted the errorbar from the range $\Delta d^2 \leq 1$ with varying both A and β , although the degeneracy between the two parameters is significant. The scatters of 50 lensing distortion profiles prefer a weaker halo mass dependence than predicted by the self-similar scaling relation at a 3σ level. This might be due to some residual uncertainty in our method, and would be worth further exploring by using a larger sample of clusters or an independent mass proxy relation such as the Sunyaev-Zel’dovich effect.

2.3.5 The halo mass and concentration relation

Another important model ingredient in our analysis is the scaling relation of halo concentration with halo mass. We have so far employed the scaling relation in DK14 as for our default model. On the other hand, other works have proposed a different scaling relation from DK14. For example, Duffy et al. (2008) proposed a different fitting formula of the c - M relation, and predicts a 20–30% lower concentration than in DK14 for cluster-scale halos. However, we found that, even if we use the scaling relation in Duffy et al. (2008) instead of DK14, it almost unchanges the $d_{\text{w-scaling}}^2$ value; more exactly, it enlarges the $d_{\text{w-scaling}}^2$ value only by $\Delta(\Delta d^2) \simeq 1$ – 2 for the HSE and gas mass proxy relations. Hence the current data cannot discriminate these different models of c - M relation.

Here we show one constraint of the underlying c - M relation. Assuming the parametrized form of c - M scaling relation given by

$$c_{500c}(M_{500c}; z) = f_c \left(\frac{M_{500c}}{4 \times 10^{14} h^{-1} M_{\odot}} \right)^{-\alpha} \times (1+z)^{-0.51}, \quad (2.28)$$

we minimized the $d_{\text{w-scaling}}^2$ value with varying the normalization parameter and the mass slope parameter, f_c and α . We took the halo mass inferred from the stacked lensing in Figure 2.5, $M = 4 \times 10^{14} h^{-1} M_{\odot}$, for the pivot mass scale, and the redshift dependence is taken from Duffy et al. (2008)⁶. Note that we fixed the mass normalization parameter to $A = 1$ for the halo mass proxy relation of X-ray observables. The figure shows that constraints on the two parameters are significantly degenerate: the $d_{\text{w-scaling}}^2$ for the best-fit model is 526.3 or 493.8 for the HSE and gas mass, respectively, which is slightly smaller than our fiducial model, DK14, as found from Eq. (2.25). The best-fit parameters are $f_c = 2.6_{-0.2}^{+0.3}$ and $\alpha = 0.08_{-0.12}^{0.13}$ for HSE, while $f_c = 3.0 \pm 0.3$ and $\alpha = -0.08 \pm 0.18$ for the gas mass scaling relation. Thus the current data prefers the amplitude of concentration to be $c_{500c} \simeq 2.6$ – 3.0 for the 50 clusters of these mass scales, which is consistent with both the theory predictions in Duffy et al. (2008) and DK14 within the errorbars, but cannot well constrain the mass slope due to the limited statistics or a narrow range of halo masses.

2.3.6 The halo mass profile

The lensing analysis of NFW scaling rests on the assumption that the mass distribution in clusters follows the *universal* NFW profile. However, the NFW profile is the simplified prediction of N -body simulations, and a further improvement in our method might be available by employing a better model of the mass profile.

Several works have pointed out variations in the inner region of the mass profiles. For instance, there might be variations in the inner slope of the mass profile (e.g., Navarro et al. 2004, and references therein). The baryonic processes would generally affect the inner structures, which tend to cause a greater mass concentration in the inner region and generally breaks the universality of the total mass profile. However, in this study, we looked into the cluster lensing signals down to $R \simeq 0.14 h^{-1} \text{Mpc}$ and above, and these effects would be unlikely to largely change our results.

Another interesting effect is a possible variation in the outer mass distribution at radii near to the virial radius or greater, as proposed in Diemer & Kravtsov (2014b) and Adhikari et al. (2014). These works claimed that the logarithmic slope of massive halos steepens more sharply than the NFW predicts, at the outer regions $R \gtrsim 0.5 R_{200c}$, depending on the details of mass accretion and assembly history. This breaks to some extent the universality of NFW profile at these outer radii. We tested this prediction by using the fitting formula for a typical accretion history that is kindly made available to us by Surhud More. However, we found that the current datasets cannot discriminate the steepened profile at the outer radii. This would be interesting to further explore with an enlarged sample of clusters.

⁶Exactly speaking the fitting formula of Duffy et al. (2008) gives the c - M relation for M_{200c} , so we converted the scaling relation to the relation between M_{500c} and c_{500c} , and found that the redshift dependence is slightly modified from the original dependence $(1+z)^{-0.47}$ by this conversion.

2.3.7 Systematic uncertainty in the lensing measurements

As we discussed above, our results imply that the X-ray inferred mass may systematically underestimate the true mass: we found a possible bias of 5 – 10% level, although it is not significant (at a 2σ level). Eq. (2.9) suggests that a 10% bias in halo mass corresponds to about 3% bias in the lensing amplitudes. This is a tiny amount, and may imply a residual error in the source redshift estimation that is obtained by matching the color of red background galaxies to the COSMOS catalog. Due to the limited color information of the current data (mostly only 2 colors), we cannot resolve this, but a further study is definitely worth exploring. For the same reason, it is worth further looking into a possible remaining systematic error in the shape measurement.

2.4 Discussion and summary

In this work, we have developed a novel method of measuring the cluster lensing distortion profiles along the NFW prediction, one of the most important predictions of CDM structure formation model. The method measures the cluster lensing profiles by averaging the “scaled” amplitudes of background galaxy ellipticities as a function of the “scaled” centric radius according to the NFW prediction of each cluster. To apply this method to real data, we combined the independent datasets for a volume-limited sample of 50 massive clusters that are the Subaru weak lensing catalog in Okabe et al. (2013) and their X-ray observables of *XMM* and/or *Chandra* satellites in Martino et al. (2014). Here we used the X-ray observables to infer the NFW parameters of each cluster; more precisely, we used the halo mass of each cluster based on the halo mass proxy relation of X-ray observables, either the hydrostatic static equilibrium or the self-similar scaling relation of gas mass, and inferred the halo concentration from the c - M relation found in N-body simulations of DK14. We found a $4 - 6\sigma$ level evidence of the existence of universal NFW profile in the 50 massive clusters (see Figures 2.7, 2.8 and 2.9). Our results give a proof of concept of the method we developed in this work.

However, the improvement in the scatters of 50 cluster distortion profiles due to the NFW scaling analysis is not as much as expected from theory using simulations of cluster based on high-resolution N -body simulations (Figures 2.12 and 2.13). We elaborated that, in order to reconcile the difference between the measurements and the simulation expectation, we need to introduce additional halo mass scatters to each cluster, by an amount of $\sigma(M)/M \sim 0.2-0.3$ (see Figure 2.13). This implies intrinsic scatters in the halo mass and X-ray observable relation (Okabe et al. 2010b). We also argued that the discrepancy might be due to an imperfect halo mass proxy relation of the X-ray observables (see § 2.3.4). Hence it would be worth further exploring the method by combining different observables of clusters. A promising example is the Sunyaev-Zel’dovich (SZ) effect. By using or combining the X-ray, optical richness and SZ effects to develop a well-calibrated relation between halo mass and cluster observables for a suitable sample of massive clusters, we can explore a further improvement in constraining the universality of cluster mass distribution. In addition, we throughout used the model c - M relation to infer the halo concentration of each cluster. In other words, we ignored intrinsic scatters of halo concentration that is known to exist even for halos of a fixed mass scale from simulation based studies. If we can use observables to estimate halo concentration for each cluster, it might improve the NFW scaling results. For example, the concentration of member galaxies might be a good proxy of halo concentration on individual cluster basis. This would be worth exploring.

Our method offers various applications. First, we inversely use the weak lensing analysis of NFW scaling to infer the underlying true relation between halo mass and cluster observables.

We made the initial attempt of this possibility in § 2.3.4, but the results seemed to be still limited by statistics as well as unknown systematic errors in the halo mass proxy relation of X-ray observables. Since the NFW scaling method up- or down-weights less or more massive clusters in order to make their profiles to be in the similar amplitudes, it can be applied to halos over a wider range of mass scales as long as the clusters in the sample follow the universal NFW profile. Secondly, we can similarly use this method to explore the underlying true form of the halo mass profile or the halo mass scaling relation with observables, as we attempted in § 2.3.5. As claimed in Diemer & Kravtsov (2014b), massive clusters might display a steeper profile at the outer radii around or beyond the virial radius than predicted by NFW model, depending on the mass accretion history. By subdividing clusters into subsamples using a proxy to infer the mass accretion history, e.g. high or low concentration, we can use the NFW scaling analysis to explore the deviations from NFW prediction at the outer radii. This is a direct test of the hierarchical CDM structure formation model, and will be very interesting to explore.

Our current weak lensing measurements of 50 massive clusters are still limited by statistics, mainly due to a low number density of background galaxies, which we needed to take in order to define a secure sample of background galaxies based on two passband data alone. Hence our method can be further improved by increasing background galaxies, based on photo- z information of more passband data. We can also combine the lensing magnification bias measurement to improve the statistics. On-going wide-area optical surveys such as the HSC survey and the DES survey promise to provide us with a much larger, well-calibrated sample of massive clusters, so it would be interesting to apply the method developed in this paper to those datasets in combination with other wavelength surveys such as X-ray or SZ effects.

Table 2.1: X-ray and Lensing Observables of 50 Clusters

Cluster	redshift	X-ray data			M_{500c} [$10^{14} M_{\odot}$]		Lensing observables		
		r_{500c} [Mpc]	Telescope	$M_{\text{gas},500}$ [$10^{14} M_{\odot}$]	M_{500c}^{HSE}	M_{500c}^{gas}	$(S/N)_{\text{WL}}$	$(d^2)^{\text{HSE}}$	$(d^2)^{M_{\text{gas}}}$
A2697	0.232	1.20 ± 0.04	<i>XMM</i>	0.880 ± 0.037	6.29 ± 0.65	5.98 ± 0.25	6.42	4.47	4.62
A68	0.255	1.40 ± 0.20	<i>XMM</i>	0.903 ± 0.135	10.44 ± 0.86	6.13 ± 0.92	6.24	13.62	7.52
A2813	0.292	1.25 ± 0.10	<i>XMM</i>	1.010 ± 0.092	6.32 ± 0.69	6.86 ± 0.63	5.45	4.66	4.28
A115	0.197	0.89 ± 0.07	<i>XMM</i>	0.546 ± 0.089	3.26 ± 0.21	3.71 ± 0.60	3.61	8.20	8.46
A141	0.230	1.02 ± 0.12	<i>Chandra</i>	0.550 ± 0.084	3.97 ± 1.37	3.74 ± 0.58	5.35	6.01	6.36
ZwCl01014	0.254	0.76 ± 0.01	<i>Chandra</i>	0.235 ± 0.004	1.67 ± 0.07	1.60 ± 0.03	3.55	5.46	5.50
A209	0.206	1.15 ± 0.07	<i>XMM</i>	0.972 ± 0.094	5.45 ± 0.18	6.60 ± 0.64	9.14	21.84	17.37
A267	0.230	1.17 ± 0.12	<i>Chandra</i>	0.703 ± 0.094	5.97 ± 1.84	4.78 ± 0.64	5.37	7.01	7.47
A291	0.196	0.94 ± 0.06	<i>XMM</i>	0.391 ± 0.031	2.92 ± 0.56	2.66 ± 0.21	4.92	8.61	8.92
A383	0.188	1.01 ± 0.08	<i>XMM</i>	0.425 ± 0.036	3.25 ± 0.45	2.89 ± 0.24	5.74	9.11	9.80
A521	0.248	1.25 ± 0.04	<i>XMM</i>	1.230 ± 0.050	7.05 ± 0.34	8.36 ± 0.34	5.98	4.66	5.23
A586	0.171	1.09 ± 0.08	<i>Chandra</i>	0.600 ± 0.049	4.42 ± 0.90	4.08 ± 0.33	5.58	10.90	11.47
A611	0.288	1.20 ± 0.06	<i>Chandra</i>	0.612 ± 0.039	6.80 ± 1.08	4.16 ± 0.26	5.98	8.24	12.30
A697	0.282	1.50 ± 0.10	<i>Chandra</i>	1.490 ± 0.127	13.14 ± 2.74	10.12 ± 0.86	4.89	20.89	12.84
ZwCl0857	0.235	0.85 ± 0.04	<i>XMM</i>	0.351 ± 0.017	2.33 ± 0.23	2.38 ± 0.12	2.45	4.53	4.60
A750	0.163	0.97 ± 0.12	<i>Chandra</i>	0.406 ± 0.061	3.17 ± 1.22	2.76 ± 0.41	6.82	16.54	18.17
A773	0.217	1.21 ± 0.11	<i>XMM</i>	0.907 ± 0.102	7.77 ± 0.94	6.16 ± 0.69	9.03	7.40	11.40
A781	0.298	1.13 ± 0.17	<i>XMM</i>	0.783 ± 0.142	6.72 ± 0.45	5.32 ± 0.96	4.27	28.93	25.32
ZwCl0949	0.214	0.93 ± 0.02	<i>Chandra</i>	0.315 ± 0.010	2.90 ± 0.20	2.14 ± 0.07	5.50	15.34	16.79
A901	0.163	0.79 ± 0.06	<i>XMM</i>	0.208 ± 0.020	1.68 ± 0.39	1.41 ± 0.14	5.58	11.98	13.43
A907	0.167	1.08 ± 0.06	<i>XMM</i>	0.623 ± 0.042	5.17 ± 0.64	4.23 ± 0.29	7.71	11.32	14.53
A963	0.205	1.14 ± 0.07	<i>XMM</i>	0.616 ± 0.050	5.60 ± 0.71	4.18 ± 0.34	7.49	13.40	17.46
ZwCl1021	0.291	1.26 ± 0.05	<i>XMM</i>	1.080 ± 0.048	6.82 ± 0.14	7.34 ± 0.33	6.78	8.76	9.23
A1423	0.213	1.18 ± 0.10	<i>Chandra</i>	0.711 ± 0.095	6.02 ± 1.53	4.83 ± 0.65	4.58	9.89	6.95
A1451	0.199	1.36 ± 0.11	<i>XMM</i>	1.050 ± 0.102	8.97 ± 2.18	7.13 ± 0.69	8.25	6.30	5.44
RXCJ1212	0.269	0.76 ± 0.05	<i>XMM</i>	0.196 ± 0.012	1.67 ± 0.31	1.33 ± 0.08	3.00	9.34	8.86
ZwCl1231	0.229	1.23 ± 0.08	<i>Chandra</i>	0.828 ± 0.078	6.82 ± 1.29	5.63 ± 0.53	5.09	17.35	16.05
A1682	0.226	1.24 ± 0.18	<i>Chandra</i>	0.764 ± 0.137	7.35 ± 3.06	5.19 ± 0.93	7.30	6.12	8.03
A1689	0.183	1.52 ± 0.07	<i>XMM</i>	1.290 ± 0.059	11.98 ± 1.94	8.76 ± 0.40	9.42	11.25	16.82
A1758N	0.280	1.38 ± 0.07	<i>Chandra</i>	1.220 ± 0.062	10.21 ± 1.54	8.29 ± 0.42	3.10	13.65	10.03
A1763	0.228	1.33 ± 0.11	<i>XMM</i>	1.230 ± 0.135	6.60 ± 0.56	8.36 ± 0.92	6.75	9.58	7.09
A1835	0.253	1.57 ± 0.11	<i>XMM</i>	1.550 ± 0.120	14.04 ± 1.27	10.53 ± 0.82	5.96	14.77	13.27
A1914	0.171	1.38 ± 0.08	<i>XMM</i>	1.160 ± 0.073	8.08 ± 1.00	7.88 ± 0.50	4.83	9.22	8.88
ZwCl1454	0.258	1.06 ± 0.10	<i>XMM</i>	0.578 ± 0.060	3.65 ± 0.42	3.93 ± 0.41	3.18	3.94	4.13
A2009	0.153	1.29 ± 0.13	<i>Chandra</i>	0.708 ± 0.082	7.33 ± 2.47	4.81 ± 0.56	4.91	5.79	5.14
ZwCl1459	0.290	1.08 ± 0.25	<i>XMM</i>	0.675 ± 0.187	5.65 ± 0.36	4.59 ± 1.27	3.31	4.16	3.73
RXCJ1504	0.215	1.47 ± 0.35	<i>XMM</i>	1.300 ± 0.337	10.93 ± 0.82	8.83 ± 2.29	4.55	7.70	6.23
A2111	0.229	1.17 ± 0.14	<i>Chandra</i>	0.719 ± 0.110	5.99 ± 1.89	4.88 ± 0.75	4.83	13.10	12.57
A2204	0.152	1.49 ± 0.08	<i>XMM</i>	1.280 ± 0.082	10.66 ± 1.72	8.70 ± 0.56	6.48	11.20	9.16
A2219	0.228	1.75 ± 0.11	<i>XMM</i>	1.882 ± 0.216	14.35 ± 2.04	12.79 ± 1.47	7.51	6.21	6.06
RXCJ1720	0.164	1.23 ± 0.11	<i>XMM</i>	0.771 ± 0.083	6.97 ± 0.68	5.24 ± 0.56	3.80	11.47	7.02
A2261	0.224	1.22 ± 0.12	<i>Chandra</i>	1.000 ± 0.127	6.75 ± 1.89	6.79 ± 0.86	8.88	13.44	13.33
RXCJ2102	0.188	1.00 ± 0.06	<i>XMM</i>	0.450 ± 0.033	3.52 ± 0.61	3.06 ± 0.22	4.04	13.87	12.78
RXJ2129	0.235	1.08 ± 0.04	<i>XMM</i>	0.749 ± 0.037	4.22 ± 0.16	5.09 ± 0.25	3.17	5.10	6.17
A2390	0.233	1.60 ± 0.11	<i>XMM</i>	1.700 ± 0.088	13.67 ± 2.09	11.55 ± 0.60	6.30	8.47	7.41
A2485	0.247	1.11 ± 0.15	<i>Chandra</i>	0.558 ± 0.087	5.32 ± 2.08	3.79 ± 0.59	4.71	1.89	0.52
A2537	0.297	1.19 ± 0.10	<i>XMM</i>	0.739 ± 0.081	7.20 ± 0.73	5.02 ± 0.55	5.05	8.73	9.81
A2552	0.300	1.25 ± 0.09	<i>Chandra</i>	1.020 ± 0.094	7.81 ± 1.64	6.93 ± 0.64	3.98	11.30	10.85
A2631	0.278	1.20 ± 0.09	<i>XMM</i>	1.030 ± 0.088	8.51 ± 0.98	6.93 ± 0.64	4.61	18.05	16.23
A2645	0.251	1.15 ± 0.18	<i>Chandra</i>	0.541 ± 0.117	5.98 ± 2.59	3.68 ± 0.79	6.59	19.54	19.62

Note: The X-ray observables (r_{500c} , M_{500c}^{HSE} and $M_{\text{gas},500}$) taken from Tables 2 and 3 of Martino et al. (2014): r_{500c} is the radius for the interior overdensity $\Delta = 500$, M_{500c}^{HSE} is the mass estimate based on the hydrostatic equilibrium, and $M_{\text{gas},500}$ is the gas mass interior to r_{500} (see text for details). $M_{500c}^{M_{\text{gas}}}$ is the total mass interior to r_{500c} assuming the *simple* self-similar scaling relation given by Eq. (2.24). The mean mass of 50 clusters $\langle M_{500c} \rangle / [10^{14} h^{-1} M_{\odot}] = 4.42$ or 3.82 for the HSE and gas mass cases, respectively. The last three columns are the lensing observables that are computed from the lensing measurement of Okabe et al. (2013). $(S/N)_{\text{WL}}$ is the total signal-to-noise ratio of lensing distortion measurement for each cluster over the 8 radial bins in the range $0.14 \leq R/[h^{-1}\text{Mpc}] \leq 2.8$. $(d^2)^{\text{HSE}}$ or $(d^2)^{M_{\text{gas}}}$ is the deviation of the lensing distortion profile compared to the NFW prediction, defined by Eq. (2.19) or (2.20) for each cluster.

Chapter 3

Transient survey of M31

3.1 Introduction

3.1.1 Magnification property of point source-lens system

General relativity predicts that a background object can be significantly brightened by strong lensing if the background and foreground objects are almost perfectly aligned along the line of sight of an observer. We can use the lensing magnification to search for an invisible, small compact object that is a possible candidate of dark matter and, if so, should exist in the halo regions of the Milky Way and M31 Galaxy.

Here we describe the observational properties of lensing magnification, as illustrated in Fig. 3.1. We denote, by β , the angle between the lens and the source object on the sky, and α as the angular separation between the source and the image. We also define the following distances; r_0 as the distance between the lens and the image in the lens plane, r between the lens and the image, D_S as the distance between the observer and the source, and x as the distance to the lens normalized by D_S . Then β and α can be described as: $\beta = r_0/xD_S$, and $\alpha = r/xD_S$.

The bending angle for a point mass is given as

$$\delta = \frac{4Gm}{c^2l} \quad (3.1)$$

(see Appendix A for the derivation). In the following we call the object which makes foreground gravitational field as “lens”, and “source” for the background object (eg. m in Eqs. (1.52) denotes the lens mass). Then the lens equation in this system can be described as:

$$D_S\beta + D_S(1-x)\delta = D_S\alpha, \quad (3.2)$$

Putting α, β, δ in this equation:

$$r^2 - r_0r - R_E^2 = 0 \quad (3.3)$$

where R_E is Einstein radius defined as:

$$R_E^2 = \frac{4GMD}{c^2}, \quad D \equiv D_Sx(1-x) \quad (3.4)$$

Note that Einstein radius is the size of so-called Einstein ring, which appears only when the observer, lens, and source are perfectly aligned in the line of sight and the lens has a axially

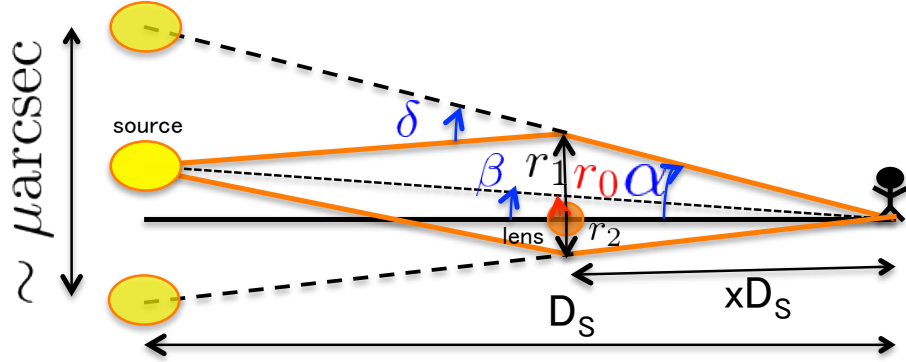


Figure 3.1: An illustration of gravitational lensing system. The light ray emitted from a source is bent by the gravitational field of a lens, and the source can be observed by multiple images due to the lensing. For a system where a star in M31 is a source object and a PBH of $10^{-7}M_{\odot}$ in either halo region of MW or M31 is a lensing object, the two images due to lensing are not resolved even by the Subaru data, because the angular separation between the two images is about 10^7 arcseconds compared to $O(0.1'')$, a typical angular resolution of the HSC/Subaru data.

symmetric mass distribution. Thus the following solutions of the lens equation represent positions of the two images:

$$r_{1,2} = \frac{r_0 \pm \sqrt{r_0^2 + 4R_E^2}}{2} \quad (3.5)$$

Since lensing does not change the surface brightness of a source object, the lensing magnification is given by the change of the apparent angular extent of the source object due to lensing:

$$A_{1,2} = \left| \frac{r_{1,2}}{r_0} \frac{dr_{1,2}}{dr_0} \right| = \left| \frac{r_{1,2}^4}{r_{1,2}^4 - R_E^4} \right| \quad (3.6)$$

For a system where a star in M31 is a source object and PBH of $\sim 10^{-7}M_{\odot}$ in the halo regions of MW or M31 is a lens object, the two images due to strong lensing events are not resolved by the Subaru data, because the angular separation is order of 10^{-7} arcseconds compared to $\sim O(0.1)$ arcseconds resolution of Subaru data. This is the so-called ‘‘microlensing’’ effect. Note that we assume that source star is a star in M31, and we don’t consider that a star in the MW halo region is a source star in our analysis. The total magnification of the lensed image is given by

$$A = A_1 + A_2 = \frac{u^2 + 2}{u\sqrt{u^2 + 4}}, \quad u \equiv \frac{r_0}{R_E} \quad (3.7)$$

Next we describe time variation of the flux during a microlensing event. The magnification of source image varies with time as the lens object moves in front of the source object. Here we define v as the relative velocity component of the lens object perpendicular to the line of sight, and d as the closest distance of lens to the line of sight. The closest distance to the lens image can also be characterized by the impact parameter, defined as $u_{\min} = d/R_S$. Here we define a typical time scale of the magnification time variation as

$$t_0 = \frac{R_E}{v} \quad (3.8)$$

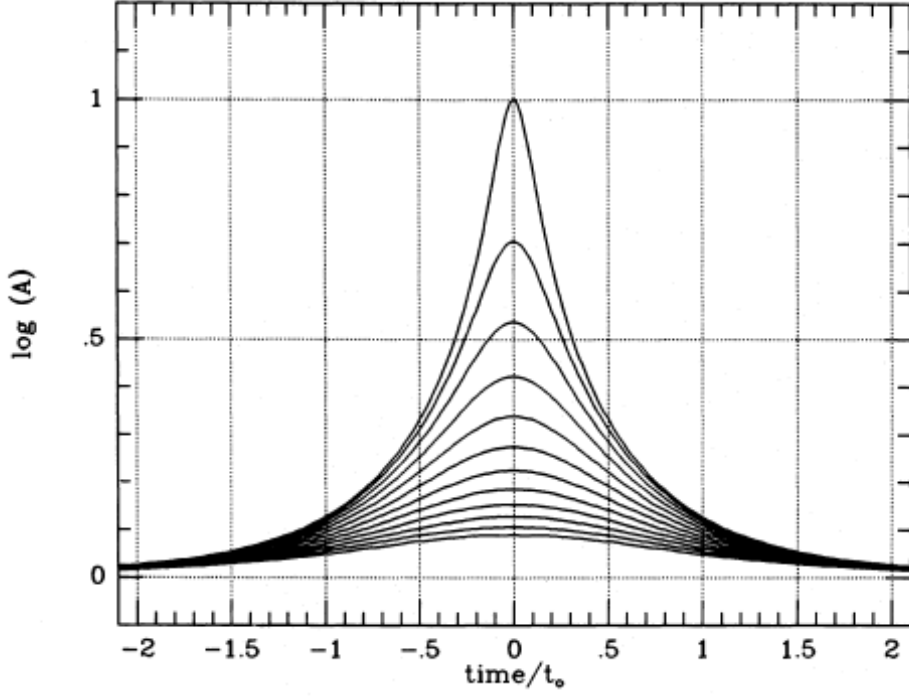


Figure 3.2: Simulated light curves for microlensing events, taken from Fig. 2 of Paczyński (1986). Each light curve stands for different impact parameter u_{\min} at 0.1, 0.2, ..., 1.1, 1.2, and light curve with larger magnification amplitude corresponds to smaller u_{\min} parameter.

With this parameter, the time variation of lens flux can be characterized as:

$$(v(t - t_{\max}))^2 + d^2 = r_0^2 \quad (3.9)$$

where t_{\max} is the time when the lens and the source are in the closest separation on the sky. By combining Eqs. (3.7) and (3.9), we obtain

$$u^2 = \frac{r_0^2}{R_E^2} = \frac{(t - t_{\max})^2}{t_0^2} + u_{\min}^2 \quad (3.10)$$

Hence the flux magnification of microlensing event is given by a function of time as:

$$A(t) = \frac{y^2 + u_{\min}^2 + 2}{\sqrt{y^2 + u_{\min}^2} \sqrt{y^2 + u_{\min}^2 + 4}}, \quad y = \frac{t - t_{\max}}{t_0}, \quad (3.11)$$

which implies that magnification is larger for smaller impact parameter u_{\min} . Note that neither the wavelength of the light ray observed nor the original luminosity of the source alter an amount of the lensing magnification.

If a source star is located at $D_S = 770$ kpc, the standard timescale of microlensing event as in Eq. (3.8) is given by:

$$t_0 \simeq 1.8 \text{hours} \left(\frac{M}{10^{-7} M_{\odot}} \right)^{\frac{1}{2}} \left(\frac{x D_S}{100 \text{kpc}} \right)^{\frac{1}{2}} \left(\frac{200 \text{km/sec}}{v} \right) \quad (3.12)$$

where we assumed that a target mass of PBH is $10^{-7} M_{\odot}$, $D_L = 100$ kpc for a distance to the lens PBH, and $V_{\text{halo}} = 200$ km/sec for the perpendicular velocity component of the lens.

3.1.2 Preview of our study

The properties of dark matter has been studied from many aspects with observations and simulations. The previous studies have suggested that dark matter is non-baryonic, non-relativistic, and interacts with ordinary matter only via gravity. Currently unknown stable particle(s) beyond the Standard Model of Particle Physics is considered as viable candidates, so-called Weakly Interacting Massive Particles (WIMPs). However they haven't been yet detected neither in elastic scattering experiment nor by collider experiments. Primordial black hole is another viable candidate of dark matter, which was first proposed by Hawking (1974). A scenario of PBH dark matter does not require new stable particles. The mass range of PBH varies depending on the formation scenario in the early universe (Carr et al. 2010).

Gravitational microlensing effect is a unique way to probe dark matter candidate, first proposed by Paczyński (1986). In microlensing regime, the flux of background star is magnified by the gravitational field of foreground object when they come in line of sight. Thus dark components can be detected through the magnification of background stars while they move. Previous microlensing studies using data such as Kepler and MACHO projects have already succeeded to detect exoplanets. The current upper limits on an abundance of PBH covers almost full range of mass scales we are interested in Capela et al. (2013a). Nevertheless, it is worth further exploring a more stringent limit on the PBH abundance.

In this study we propose a transient search for M31 dense-star region, using Hyper Suprime-Cam at Subaru telescope. Our survey expects higher event rate of PBH microlensing than the previous search, owing to the wide field-of-view and excellent image quality for the dense star field. The one pointing of HSC can cover the entire bulge and disk regions of M31. However, the analysis is expect to be not straightforward; for example, reduction procedures need some careful treatments because no previous transient search performed a careful reduction for images with such a dense field taken by highly resolved wide field camera. Thus we will develop the method to optimize the transient analysis using the software called HSC-pipe. Our observation also enables to search for various variable stars such as flares, binary stars and microlensing due to free-floating exoplanets.

3.2 Observation and analysis

We expect a large number of transient candidates in the dense star region of M31. The M31 is the largest spiral galaxy in the neighbor of Milky Way and is about 770kpc away from us. Hence many stars, especially in bulge and disk regions of the M31, can be in one CCD pixel; that is, each star cannot be resolved even by the HSC/Subaru. In § 3.2.1 we describe our strategy for our observation in detail. Then we describe the methodology of data reduction in § 3.2.2, and procedures we used to extract variable candidates in § 3.2.3.

3.2.1 Obsevation

(1) Methodology of transient survey : pixel lensing

In the previous microlensing study in Large Magellanic Cloud (LMC), another dense-star region, the photometry on each star is achieved because of its proximity; only 50 kpc away from us (Alcock et al. 2000). However, this is not the case for M31. As M31 is about 770 kpc away and further than LMC, multiple stars can be in the same CCD pixel.

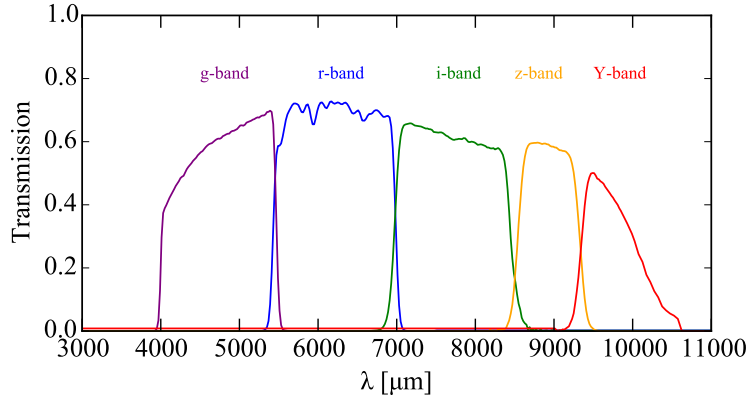


Figure 3.3: The total transmission curve for each broad-band filter of the Subaru/Hyper Suprime-Cam system. Each curve takes into accounts the transmission of each filter, quantum efficiency of fully depleted CCDs, transmittance of the dewar window, transmittance of the Primary Focus Unit of the HSC (POpt2), and reflectivity of the Primary Mirror.

In order to measure the time variation of flux in such a crowded imaging data, we adopt a method called pixel lensing (Alard & Lupton 1998). Even when multiple stars locate in a pixel, we can trace the change of flux in a pixel unit. Thus we can extract the location of variable candidates assuming that there is only one variable star in a pixel. In addition we adopt a technique so-called image difference to make comparison between images in different time frames. Image difference technique is also helpful for precise photometry in pixel lensing regime because we can cancel the effect from surrounding stars (see Sec 3.2.3 for the detail). As this comparison requires an accurate astrometry matching between different frames, we use the reference image generated by combining best-seeing frames to perform the image difference between the reference image and a target frame image in order to minimize effects of imperfect astrometry.

(2) Instrument : Hyper Suprime-Cam

Hyper Suprime-Cam (HSC) is a wide-field imaging camera attached at the prime focus of Subaru telescope. This camera consists of 116 CCD chips; 104 for science, 4 for auto-guide, and 8 for auto-focus, and each CCD has 2k x 4k pixels, with a pixel scale of 0.168 arcsec. One unique characteristic of this camera is the wide field of view (FoV) as large as 1.5 degree at a single frame, which is three times larger than the size of full Moon in radius. Also high resolution is expected owing to the large primary mirror of 8.2 meters in effective diameter and low humidity of the summit of Mauna Kea. 261 robotic fingers keep the primary mirror in a perfect shape no matter where the telescope is pointing in the sky. The filter transmittance is shown by Fig. 3.3 using the HSC filter model¹ including quantum efficiency of fully depleted CCDs (FDCDDs), transmittance of the dewar window, transmittance of the Primary Focus Unit of the HSC (POpt2), and reflectivity of the Primary Mirror.

(3) Details of observation

A search of microlensing events requires a precise photometry of stars. The HSC pointing of our observation was determined so as to cover the entire region of M31, from the inner bulge to the outer disk regions, with its one pointing. Hence the pointing is centered at the coordinates of the M31 central region: (RA, dec) = (00h 42m 44.420s/+41d 16m 10.1s).

¹<http://subarutelescope.org/Observing/Instruments/HSC/sensitivity.html>

Target	Transit	Elevation	Rise	Set
J00420+4115	20:51	67.6	16:26	01:17

Target visibility from Mauna Kea
Night of 23 Nov 2014

Sunset 17:37
Twilight ends 18:56

Sunrise 06:32
Twilight starts 05:14

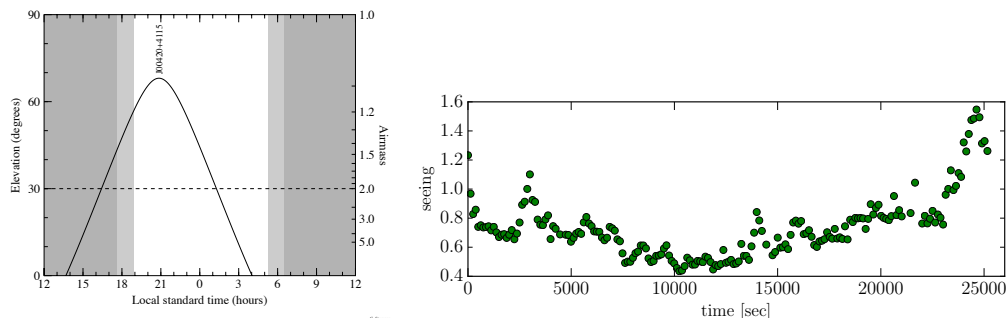


Figure 3.4: Characteristics of our HSC M31 observation. Left panel shows the time-variation of altitude of target field (M31) during observation. Our observation started from 18:33:59 on November 24 2014, and ended at 1:35:34 when the altitude gets lower than 30 degrees. Right panel shows the seeing of each exposure. We conducted the “focusing” (determined the focus position of the camera) three times during the night, 19:50:33, 22:37:02, and 0:37:07.

As we described above, we need to compare/differentiate the total flux of the same CCD pixel between different exposures in order to find transient candidates. That is, we want to measure the same (multiple) stars by the same CCD pixel, because we then care only about the relative flux difference in the same pixel of different exposures (do not care about an absolute flux calibration between different pixels). Therefore, we did not employ any dithering strategy for our observation. However, in reality the HSC/Subaru system has an imperfect accuracy of auto-guiding and/or pointing, so we have found variations in the pointings of different exposures, by a few pixels up to pixels, as we will discuss later.

Our observation was conducted in November 23, 2014 on dark night, one day after new moon. We acquired the 194 exposures of M31 for about 7 hours starting from sunset of the day until the elevation of M31 on the sky becomes down to about 30 degrees. The sampling rate of images is about 2 minutes, 90 seconds for each exposure and about 30 seconds for readout. All images were taken in r -band filter, corresponding to $0.64 \mu\text{m}$ in wavelength. The visibility (elevation) of M31 and the seeing size of each exposure are given in Fig. 3.4. Here the “seeing” is a commonly-used quantity to characterize a spatial resolution of an image, i.e. the size of the point spread function (PSF) of the image.

3.2.2 Data reduction: single frame processing

One HSC exposure consists of data from 104 science CCD chips. The raw data transferred from the Subaru Observatory is given in fits format, and each exposure amounts to about 2Gbyte in data size. The data itself contains only flux information (more exactly, ADU counts) in pixel coordinate. For example, to compare the images between different exposures, i.e. the difference image, we need to use the common coordinates of the images used (the same objects should be in the same coordinates in between different exposures). A precise photometry requires a correction of various systematic effects such as night glow, instrument noise, vignetting of the camera, and variations in responses between different CCD pixels.

In this section we describe our analysis method, focused on the reduction method on a single exposure data. Our current procedure is not perfect, and some problems are described in § 3.3.1. All data reduction was done using the HSC pipeline, the specialized software package that has been developed for the HSC SSP program, being led by scientists at Kavli IPMU, Princeton University and NAOJ.

Single frame processing of CCD data

Raw CCD data contain various contamination. Some effects are time-dependent and could cause an inhomogeneity between different images (taken in different time). Thus we calibrate every CCD data to correct for these effects. To make some basic calibrations as described below, we used the calibration data that was taken during the same observation run, on November 14 2014. The basic calibrations we implemented are summarized below: ²

- Bias subtraction
The CCD readout noise fluctuates the pixel counts around some non-zero constant, even if a shutter of the camera is not open (i.e. no incident photon). Hence the procedure “Bias” correction is needed to correct for this non-zero counts by using the counts of zero-second exposure data in each CCD pixel. We used the 3 sigma clipped mean of 10 BIAS exposures to make correction in each pixel.
- Dark current subtraction
Another CCD noise is the so-called dark current. Dark current is caused by random motion of electrons in detector, and the characteristics is different from pixel to pixel. The amount of dark current depends on the length of exposure time. We took the 300 sec exposures, with closing the shutter, then estimate the dark current rate (counts/sec), and subtract the dark current contamination from each science exposure based on the exposure time. Note that the dark current contamination for the r-band image is negligibly small compared to Poisson noises from sources plus sky background.
- Flat-field determination
Even if all the CCD chips are illuminated by the same photon flux, each CCD pixel generally has different acquired counts due to variations in the pixel-to-pixel sensitivity of the detector and/or due to distortions in the optical system (e.g. vignetting). We performed the flat field correction, i.e. corrected for the inhomogeneities, by using the dome flat data.

After the above basic data processing, we need to subtract background contamination due to light diffusion of the atmosphere or other unknown source – background subtraction. However, the background subtraction for the M31 region is quite challenging, because there is no blank region and every CCD chip is to some extent affected by unresolved, diffuse stellar light. Hence, we would suffer from an under- or over-subtraction. Nevertheless, since we are mainly interested in time-variable stars, we tried to perform the two methods of background subtraction, as will be described in § 3.3.1 in detail.

We further need to correct for effects of cosmic rays. For the fully-depleted CCDs, cosmic ray events imprint a characteristic trail-like image. For a blank field, it is relatively straightforward

²Main reference for this part is <http://subarutelescope.org/Observing/DataReduction/>. The detailed procedure on HSC-pipe is described in <http://hsca.ipmu.jp>. Details are described in the following reference: <http://www.astro.princeton.edu/~rhl/photo-lite.pdf>.

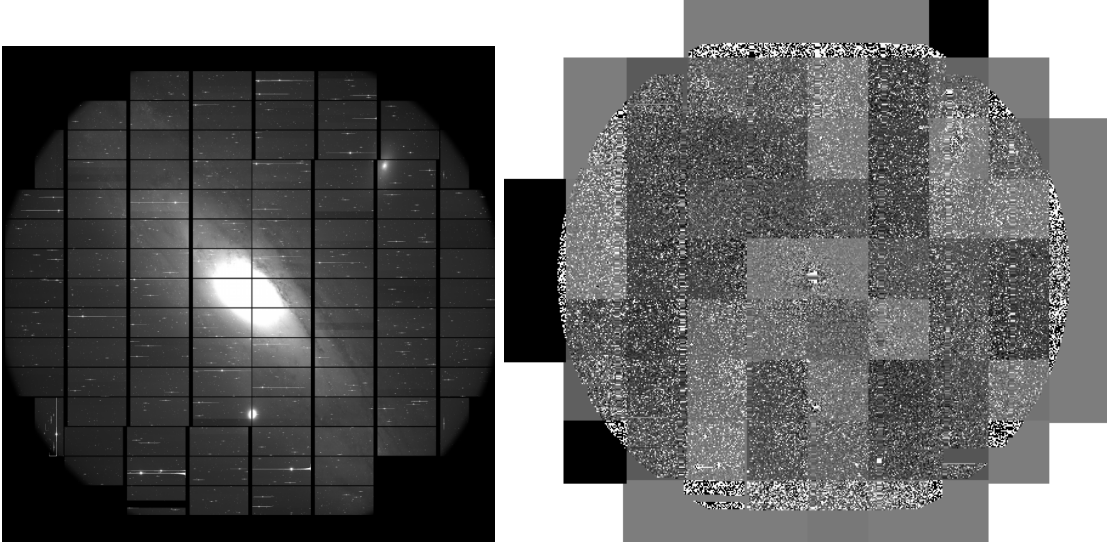


Figure 3.5: An example of our exposure image of the M31 region. Left panel displays one raw image taken by Hyper Suprime-Cam. Each rectangle-shape sub region, enclosed by black-color gap, corresponds to a single CCD chip. Right panel shows one example of reduced image, the one later called as reference image in z-scale (The detail of this image is described in § 3.2.3). This figure is in a unit called “tract”, composed of sub-regions called “patches” (displayed as different-color rectangular regions in this figure).

to identify the CR image from the trail-like image, or by combining several exposures. However, the CR removal is not so straightforward for the dense star field we are working on. We skipped the CR removal for simplicity, and will discuss the residual effect later.

To implement the difference image technique in order to find transient candidates, we used the following methods:

- WCS determination

Here we describe how to determine the WCS coordinate system for 194 exposures. In addition to our fiducial exposures each of which is a 90 sec exposure data, we also took 30 sec exposure at the beginning of our observation, because bright stars are less saturated in the short exposure, and therefore we can use more stars for astrometry determination. By using the star catalog of Pan-Starrs survey as the input catalog for the M31 region, we solved astrometry solution of every 11 images, 30 sec exposure plus time-sequential 10 exposures taken from the science 194 exposures.

The HSC pipeline provide us with a useful feature, the so-called “SkyMap”, which defines a conversion of the celestial sphere to the flat coordinate system, “SkyMap coordinate”, based on a tiling or tessellation. The largest region in the coordinate is called a “Tract”, and it contains a “Patch”. These processes performed a warping of each exposure to determine the common WCS of the SkyMap.

3.2.3 Data process for transient survey

After the basic data reduction as mentioned in the previous section, we apply the image difference technique to the 194 exposures in order to search for transient candidates. If an object had a variation in its flux, the object would appear as an object with positive or negative counts in the

difference image. On the other hands, other objects, which have no flux change, will disappear in the difference image. In the following, we describe procedures that we used for our transient search.

(1) **Methodology : Image difference**

Making the image difference or image subtraction comparing different exposures is one of the most important data processes for our science. If two exposures to be compared have same seeing, same pointing and similar sky noise, the image difference would be straightforward. However, our 194 exposures have quite different seeing sizes (ranging from 0.4'' to 1.6''), and have variations in the pointing accuracy (within 5 pixels between time-sequential two exposures). In addition, the M31 field contains dense, crowded star regions. Hence, we need to make a more careful analysis.

To have a robust result of the image difference, we combined or coadded 10 best-seeing size exposures among the 194 exposures to generate the “reference” image, where the 10 exposures are not time sequential (but most of the 10 exposures are from the data in 3 hours from the observation start). Fig. 3.4 shows how the seeing size changes with time from the observation start. For a target image to be compared with the reference image, we coadded the 5 time-sequential exposures to generate the target image with improved signal-to-noise ratio. We have 37 target images (note that the target images might contain some exposures used in the reference image). Hence, we have 37 time-sequential target images, given in the units of SkyMap patches. Our method thus has a sensitivity to find transient objects with time scales longer than 10min.

We subtract the reference image from each of the 37 target images in order to generate the difference image. Fig. 3.6 shows an example of the difference image. Almost all the stars are cleanly subtracted. Note that, if a single visit is used to compare with the reference image, cosmic rays show up in the difference image. This is another region to use the coadd image of 5 exposures for the image difference. We expect that an object that has a flux change shows up in the difference image (for this particular example, there is no secure candidate of variable star). Note that there are several failure regions in performing the image subtraction. For example, in the bulge region of M31, we cannot construct the coadd images because there are too many stars and we cannot solve the astrometry from the distribution of identified stars. The summary of image difference scheme is given in Fig. 3.7.

(2) **Detection method of variable candidates**

As we described, we constructed the 37 difference images by comparing each of 37 time-sequential coadded images with the reference image. Since time separation between the 37 coadded images is about 10min, we can search for transient candidates whose variations are longer than 10 minutes. Our main interest is variable stars, and we need to exclude fake candidates arising from cosmic rays, fakes due to imperfect image subtraction (e.g. around bright stars), and so on.

To remove obvious fakes in the first step, we impose the following conditions to identify transient candidates, based on the fact that the secure candidates should look like a PSF image in the difference image.

- minSizeRatio (Minimum value of size ratio of detected source and PSF): 0.75
- maxSizeRatio (Maximum value of size ratio of detected source and PSF): 1.25

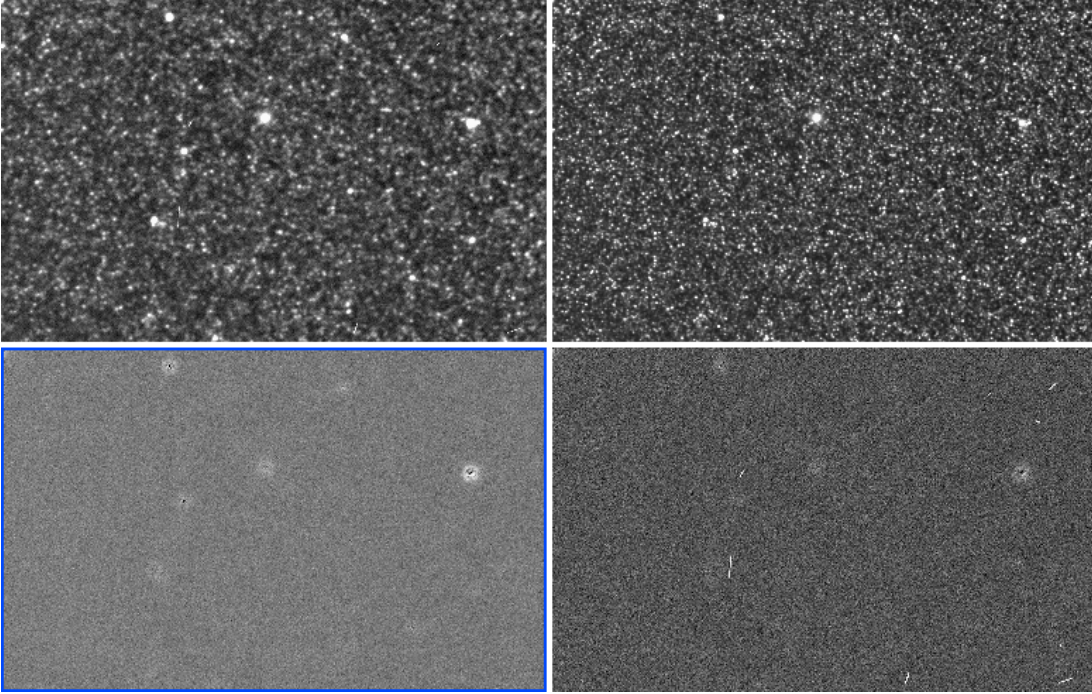


Figure 3.6: An example of the image subtraction of the two images. Here we show the image taken from the 1/60 region of patch=2.6, which is in between the disk and halo regions; the size of image is 25'' for the horizontal width. *Upper left*: one example of reduced image of single-visit frame. *Upper right*: the “reference image” generated by combining or coadding the 10 best-seeing exposures among the 194 exposures. *Lower left*: the difference image obtained by subtracting the target image, which is constructed by coadding the 5 time-sequential images, from the reference image. Almost all the stars, except for a saturated, bright stars, are cleanly subtracted. Our default analysis for transient search uses the target images of 5 time-sequential coadds for other patches. Photometry of transient candidate object is performed on the difference image. *Lower right*: for comparison, the difference image when subtracting the single exposure from the reference image. For this case, there are cosmic rays in the image.

- *limAxisRatio* (Limit value to be consistent with PSF): 0.75
- *maxResidual* (Maximum value of residual after PSF subtraction): 3.0
- *thresholdValue* (Threshold of signal to noise ratio of PSF counts): 5.0

The former two conditions exclude candidates which looks unlikely to be a point source; *minSizeRatio* excludes candidates whose shapes are very elongated, and *maxSizeRatio* mainly excludes those with tiny, vague shapes. The latter two conditions are imposed concerning the flux distribution. As mentioned before, variable star candidates are expected to have a point-source flux distribution that can be therefore well fitted by the PSF in the image. Thus *limAxisRatio* condition excludes candidates whose flux distribution cannot be well fitted by PSF in the difference image. In addition *maxResidual* removes candidates whose residual image after subtraction of the fitted PSF image is too large. Finally *thresholdValue* selects candidates whose PSF magnitude in the difference image satisfies $S/N > 5$.

We identify secure candidates that pass all the above conditions. However, the number of identified transient candidates in the 37 difference images are still too many, although the

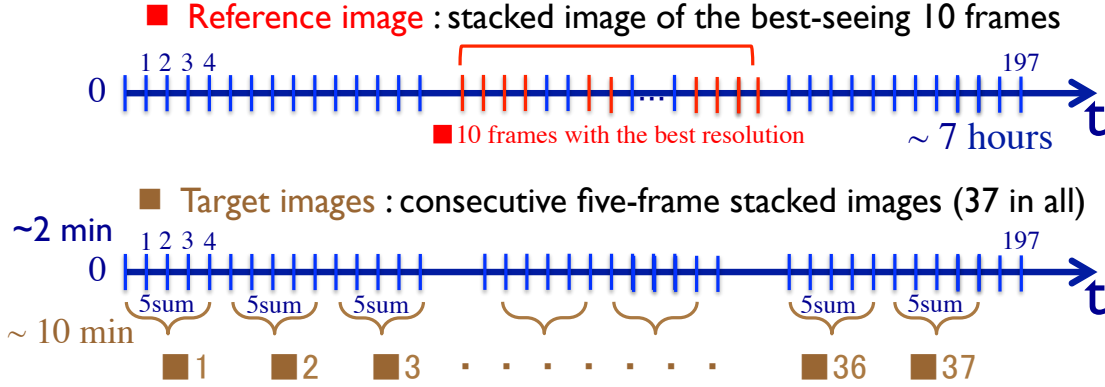


Figure 3.7: Summary of § 3.2.3, describing the image difference method in our survey. Upper panel shows the way reference image is constructed; simply by stacking the best-seeing 10 frames. Note that these frames are concentrated on the period around $\sim 11,000$ sec from the observation start; in other words, some of the 10 exposures are not time-sequential. Lower panel shows the way of generating target images to be compared with the reference image. We coadded 5 time-sequential exposures to generate each target image, where each object has an improved signal-to-noise ratio and cosmic rays are more cleanly removed.

images with worse seeing size tend to give us a smaller number of the candidates. Fig. 3.8 shows typical fake candidates that passed the above conditions. In particular, the number of survived fakes changes a lot depending on a chosen threshold value of *limAxisRatio*. However, we consider the upper conditions are loose enough to pick up any real variable candidate because they already pick up many fake events. One important note is that median subtraction around a target greatly helps to reduce some fakes (see the detail in § 3.3.1).

After the detection selections we construct a catalog of variable candidates, simply grouping those within ± 2 pixels in pixel coordinates from the 37 different-time frames. The properties of variable candidates is described in detail on § 3.3.2.

(3) Photometry of a time-variable star candidate

Once a secure candidate of time-variable point source is found, we have to make a photometry of the candidate in order to measure the light curve. However, the photometry in a dense star region, where multiple stars exist in each CCD pixel, is difficult. To overcome this difficulty, we use the following method by making best use of the difference image.

For a secure candidate found based on the above method, we first determine the WCS position of the candidate in the difference image. Then we measure the PSF magnitude at the WCS position of the candidate in the reference image that is deepest and has the highest spatial resolution:

$$m_{\text{Ref}} = -2.5 \log \left(\frac{C_{\text{Ref}}}{\text{fluxmag0}_{\text{Ref}}} \right) \quad (3.13)$$

where C_{Ref} is the counts of the PSF photometry and $\text{fluxmag0}_{\text{Ref}}$ is the magnitude zero point of the reference image. Then we also perform the PSF photometry at the same WCS position of the candidate in the *difference image* of each target exposure, rather than in the original image. In this way we believe that we can measure the change in the PSF flux

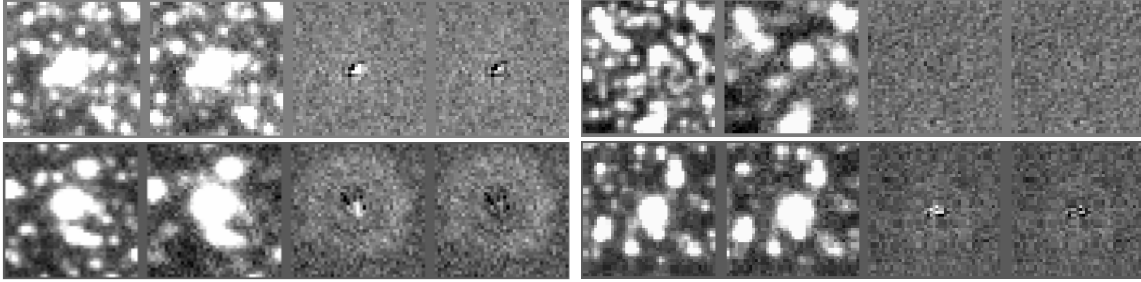


Figure 3.8: Examples of transient candidates that are excluded by our conditions to select a point (PSF-like) source transient in the difference image. The 4 postage-stamp images in each panel show the reference image (the coadd image of the 10 best-seeing images), target image (the coadd image of 5 time-sequential images), the difference image and the residual image after subtracting the best-fit PSF image, from left to right, for each fake candidate. Upper panel shows a typical example of fake candidates that are excluded by the condition `maxSizeRatio` (the image looks smaller than the size of PSF at the image position). Upper right panel shows a typical example of fake candidates that are excluded by the condition `maxSizeRatio` (the image looks larger than the PSF size). Lower left panel displays an example of fake candidates that are excluded by the condition `limAxisRatio` (the shape of the image appears inconsistent with the PSF shape, although the size looks consistent with the PSF size). Lower right panel displays an example of fake candidates that are excluded by the condition `maxResidual` (the residual image looks too large).

for the candidate. By adding the PSF magnitude to the magnitude in the reference image, we can estimate the apparent magnitude of the candidate in the target image:

$$m_i = -2.5 \log \left(\frac{C_{i,\text{diff}} + C_{\text{Ref}}^{i,\text{diff}}}{\text{fluxmag}0_{i,\text{diff}}} \right) \quad (3.14)$$

where $C_{i,\text{diff}}$ is the counts of the candidate for the i -th target image. Fig. 3.9 shows the light curve for an example secure candidate measured based on the method. For comparison, the right panel shows the light curve for the candidate, if we measure the PSF magnitude at the same WCS position of the candidate in the target image, rather than measuring in the difference image. In this case, the shape of the light curve is similar to the curve of seeing size shown in Fig. 3.4. In this case, the PSF magnitude contains contamination from surrounding stars; for an image with larger PSF size, the PSF magnitude tends to be brighter due to contamination of the surrounding stars within the PSF size. Fig. 3.10 illustrates our photometry method of each variable candidate in each target image.

3.3 Results

After an identification of secure time-variable stars and their light curve measurements, we can study properties for different types of time-variable point sources. Here we describe the main results based on our analysis. There should still be a room to improve the transient search. We first discuss effects of different data processing methods on our search of time-variable point-source candidates, in § 3.2.2. Then we will discuss properties of different types of time-variable point-source candidates in § 3.2.3.

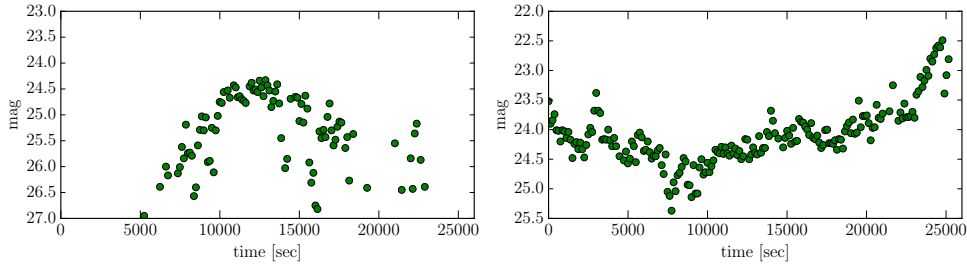


Figure 3.9: An example of the light curve of a secure time-variable point source candidate. We made a photometry of the candidate in a dense star region, where multiple stars can be in a CCD pixel. We first find a secure candidate from the image difference comparing the reference image and the target image, as we described in Sec. 3.2.3. We then make the PSF photometry at the same WCS position of the found candidate in each of the 194 difference images. Note that the PSF counts in the difference image can be negative, if the candidate gets fainter compared to that in the reference image. Then we add the PSF magnitude counts to the PSF magnitude at the same WCS position in the reference image in order to estimate the total flux of the candidate at the time of the target image. Note that the reference image is mostly from the best-seeing exposures at $t \sim 10000$ sec. For comparison, the right panels shows the light curve of the candidate if we use the PSF magnitude at the same WCS position of the candidate using each of the target image, rather than using the difference image. The shape of the light curve appears similar to time variation of seeing size in Fig. 3.4, reflecting that the estimated PSF magnitude is overestimated for the image with larger PSF size due to contamination from the surrounding stars in the image.

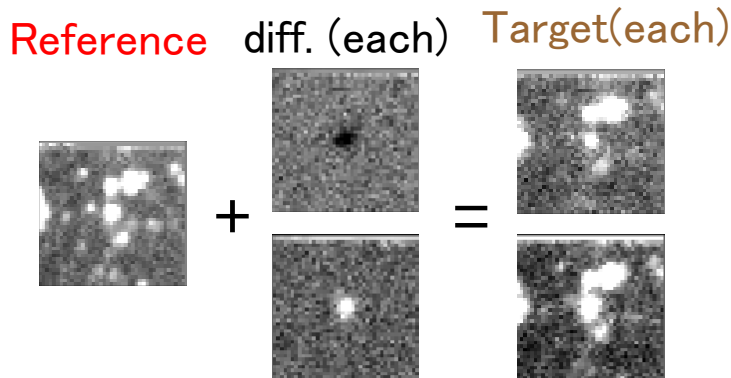


Figure 3.10: An schematic illustration of our photometry measurement of time-variable point-like source in the dense star region of M31. We made use of the difference image in the target image rather than using the original image. The left image is a postage-stamp image around a secure time-variable star candidate in the reference image. Then, the middle image shows the difference image for the target image. We make the PSF photometry on the difference image at the same WCS position of the candidate. The upper image show the case that the candidate in the target image appears fainter than that in the reference image, while the lower image shows the case that the candidate appears brighter than that in the reference image. By adding the PSF magnitudes in the reference image and the difference image of the target exposure, we estimate the PSF magnitude of the target image as given in the right panels.

3.3.1 Impacts of different data processing methods

As we stressed several times, a photometry in a dense star region of M31 is very challenging. Hence, the different data processing methods change the photometry results of time-variable

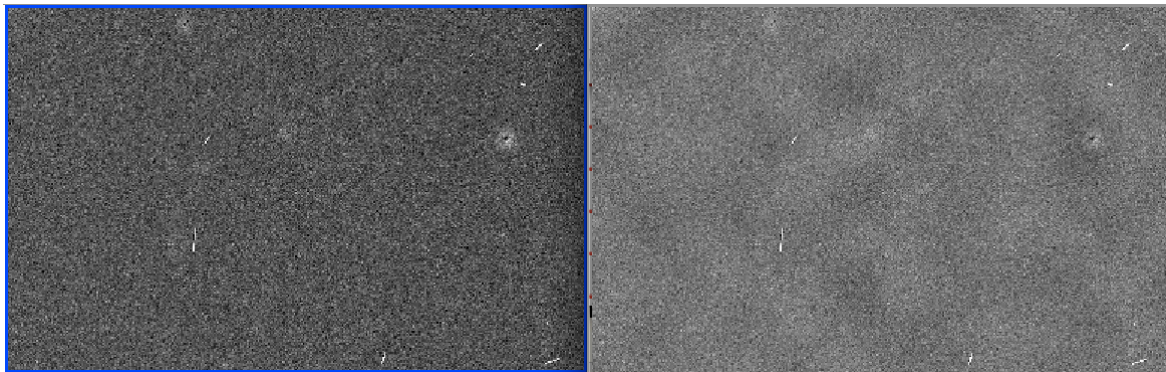


Figure 3.11: Comparison of the two images reduced by using different background subtraction methods. Left panel shows an example of the difference image using the 6th order polynomial fitting for background estimation, as in the lower right panel of Fig. 3.6. Right figure shows an example of the difference image using the spline fitting method for the 64 meshes in each CCD chip (default method). This image shows a residual pattern of the background field, which causes an inaccuracy in the photometry of time-variable star candidates.

point-source candidates. Here we discuss effects of different analysis methods.

(1) Background subtraction for single-frame processing

As we stressed in § 3.2.3, background subtraction is an important process for precise photometry (see § 3.2.3 for the detail). This process, however, is not simple especially for a wide field imaging data like HSC. Normally we divide each CCD chip into different meshes (the default subdivision is done into 64 meshes in each CCD chip), and then estimate a smooth background by spline-interpolating the average counts over different meshes. However, the spline fitting does not work well because a large number of stars in each CCD chip cause a large variation of background counts even within the chip. Thus a over- or under-subtraction of the background counts can often happen, leaving an inhomogeneous pattern in the background-subtracted image as shown in the right panel of Fig. 3.11.

In order to overcome this inaccuracy, we employed a higher-order polynomial fitting of the background. We employed the 10-th order polynomial fitting for the CCD chips around the bulge region, which are particularly dense star regions. For other CCD chips, we used the 6-order polynomial fitting.

The different background subtraction methods lead to a different number of time-variable candidates. Fig. 3.12 compares the distributions of identified candidates based on the different subtraction methods, the spline-fitting method (right panel: the default method of HSC pipeline) and the polynomial fitting method developed in this paper (left panel). The number of candidates found using the polynomial method is about 11,000, while it is about 1500 candidates for the spline fitting method. Note that both the methods fail for M31 bulge region and a region around NGC205, which are extremely dense star regions. This is due to the fact that the pipeline can't identify a sufficiently number of stars due to too dense stars, with many saturated pixels, and warping different exposures to the same WCS doesn't succeed. Hence, we can't either make the difference images for these regions.

(2) Star-flag treatments on astrometry procedure

One problem to note is that polynomial fitting often fails in mosaic procedure because

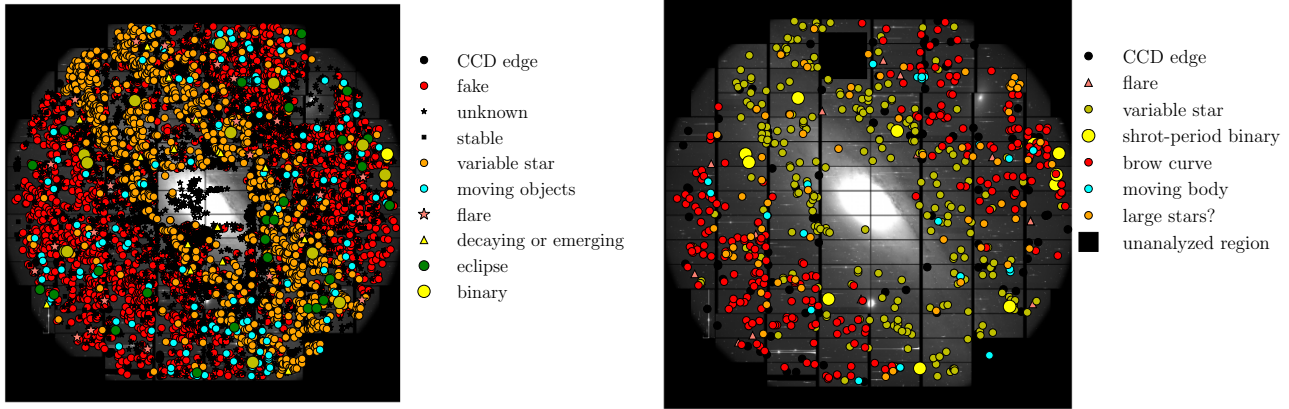


Figure 3.12: Distribution of variable star candidates across the M31 region covered by 104 CCD chips. The right panel shows the distribution of variable candidates obtained when using the spline fitting method for background subtraction in each CCD chips (the default method of HSC pipeline). For this case we found about 1500 candidates in total. The different color symbols are different types of variable candidates classified based on their light curves. Left panels displays the distribution of variable candidates obtained by using the 6 or 10-th order polynomial fitting method for each CCD chip (see text for details). For this case, we found about 11,000 candidates. For a particularly dense star region such as the bulge region or NGC205 region, our data processing method cannot properly work, and we cannot properly find candidates of variable stars in these regions.

only limited number of stars are used for the calculation. This problem is caused by the misdirection of cosmic rays as stars and the following misclassification of stars and galaxies due to the wrong measurement of PSF magnitudes. Therefore we applied object-size condition for PSF measurement, and abandon to use smaller candidates than default condition for images with seeing worse than $0.8''$ (default minimum size threshold is 0.9 , and here changed to 1.3 for images with seeing $\sim 1.2''$). At this moment we have succeeded to achieve a fairly accurate background subtraction using the polynomial fitting method, as shown in the left panel of Fig. 3.11.

(3) Median background subtraction in the postage-stamp image around each candidate in the difference image

As we described, we use the difference image to perform the PSF photometry of each time-variable candidate. However, the background subtraction is challenging and we often find a residual background mode around a candidate in the difference image. For example, if the difference image has a coherent negative counts around a candidate, the PSF photometry cannot work, because the PFS function is a decaying function with radius, asymptotically going to zero at large radii, and therefore a fitting of the PSF function to the difference image of the candidate with varying either positive or negative PFS flux parameter fails to reproduce the coherent background at large radii. To avoid a contamination of the residual background to the PSF photometry of a candidate, we measure the median background mode in 41×41 pixels around each candidate, subtract the median background from the postage-stamp image, and then perform the PSF photometry of the candidate in the difference image. Fig. 3.13 shows the improvement in the PSF photometry due to the local background subtraction in the difference image. Based on the results, we used the median background subtraction around each candidate in the difference image as our default analysis. We succeed to discard more than 1000 fake events from images with



Figure 3.13: Effects of residual background uncertainty in the difference image on the PFS photometry of a time-variable candidate. The left and right panels show the postage-stamp image around the same time-variable candidate: from left to right in each panel, the reference image, the target image, the difference image and the residual image after subtracting the fitted PSF image from the difference image. In the right panel, we found a residual background counts in the difference image. Due to this residual background, the PSF photometry doesn't work, and the rightmost image shows a residual image after subtracting the fitted PSF image. Left panel shows that the PSF photometry can work if the median background in the 41×41 region around the candidate is subtracted before the PSF photometry.

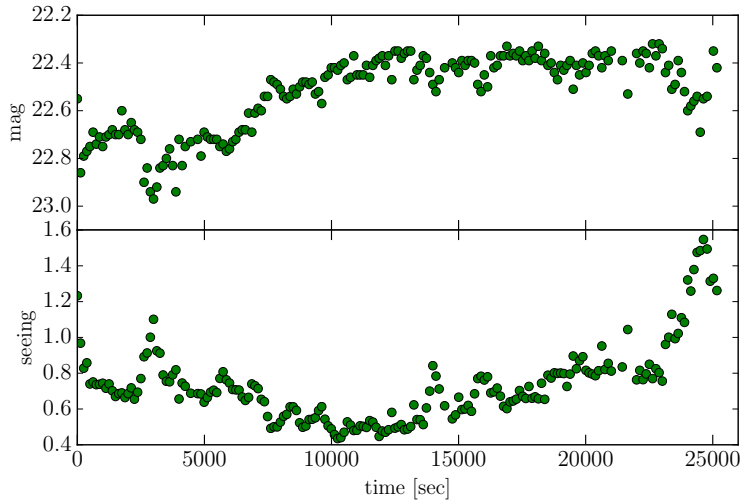


Figure 3.14: A typical example of a fake candidate whose light curve (upper panel) has a clear correlation with the seeing variation (lower panel). The light curve has a sharp feature when the seeing size has a sudden change.

median subtraction.

(4) **Fake candidates due to imperfect PSF matching in the image difference process**

Making the difference image or subtraction of the reference image from the target image requires a matching of different PSFs in the two images; more exactly, the HSC pipeline allows us to estimate the differential Kernel between the two PSFs so as to minimize residual images in the difference image. However, in reality, an imperfect PSF matching leaves residual fluxes of every object in the difference images. For some objects, the residual images might pass our detection threshold ($S/N > 5$). Again, once a candidate passes the detection threshold in a single target image, we will study the light curve of the candidate over time. If this is the case, the light curve of such a fake object would correlate with the seeing size. In fact we are finding such fake candidates, as shown in Fig. 3.14. At the moment we think that such candidates are fake, if their light curve has a correlated shape with seeing variations in time. We have found about 1,000 such fake candidates, among 11,000 candidates. We simply made several ways tests in mosaic procedure by changing the group of image used to solve astrometry: 20-frame grouping instead of 10-

frame (current analysis), or 1-frame combined with one 30 sec exposure image. The number of failure changed a bit but not drastically, because most candidates are detected in other time-frames. Therefore we skip this part to continue the analysis.

3.3.2 Properties of secure candidates

In this section we discuss properties of secure candidates whose light curve has a typical transient feature (flash, contiguous variation, etc.), as shown in the left panel of Fig. 3.12. Our classification of different types of time-variable stars is based on our eye-ball checks of their light curves. We found 11,462 secure candidates.

To study color of each secure candidate we used the g-band data of M31 that was taken in the engineering run on June 16, 2013, in addition to our r-band data. The g-band data have a seeing size of about $0.6''$, consist of 10 exposures, and have 750 seconds in total ($120 \times 5 + 30 \times 5$). We made the coadd images of the g-band data. We used Kurucz (1993) to model the stellar color taking into account the HSC filter responses we used.

In the following, we summarize properties of each type of time-variable candidates. The typical light curve for each type is shown in Fig. 3.15, and the light curves for individual promising candidates are given in Appendix C.

- Eclipsing binary

This type of candidates display a light curve with eclipse dip, during a given duration, and then such a transient feature repeats with a given period. We classify these kinds of candidates as an eclipse binary of stars, where two stars are rotating around each other and either of the two stars causes an eclipse on another star, leading a dip in the light curve of their total flux. The depth of ellipse, time duration and period are different from candidate to candidate. All the candidates seem to be M-type stars based on their $g-r$ colors. The candidates are described in Fig. C.4.

- Binary stars

For candidates that have pulsating light curves, we classify those as candidates of binary stars. If the two amplitudes of light curve within one period are similar, the stars have almost same mass and size stars. Their $g-r$ colors indicate that almost all binary systems are M-type stars. About 10 systems have a period shorter than our observation duration (about 7 hours), and the shortest period is about 1.2 hours. These short period binary systems would be a contact binary system, where the two stars share the common envelope. These binary systems we found are shown in Fig. C.5.

- Cepheid variable stars

For candidates whose light curves display a rising or declining curve over 7 hours with about 0.1-1 magnitude change, we classify those as Cepheid variable star candidates. Most Cepheid candidates are found along the disk region of M31, and the distribution seems to match the distribution of classical δ Cep variable stars found by PAndromeda project (Kodric et al. 2013). Due to the limited time observation, we can't measure an entire period of the light curve, so can't determine the period of each candidate. Their $g-r$ colors indicate that most candidates are A- or F-type stars. Fig. C.6 show the Cepheid candidates.

- Stellar flare

For the candidates whose light curve shows a sudden magnification in brightness, followed

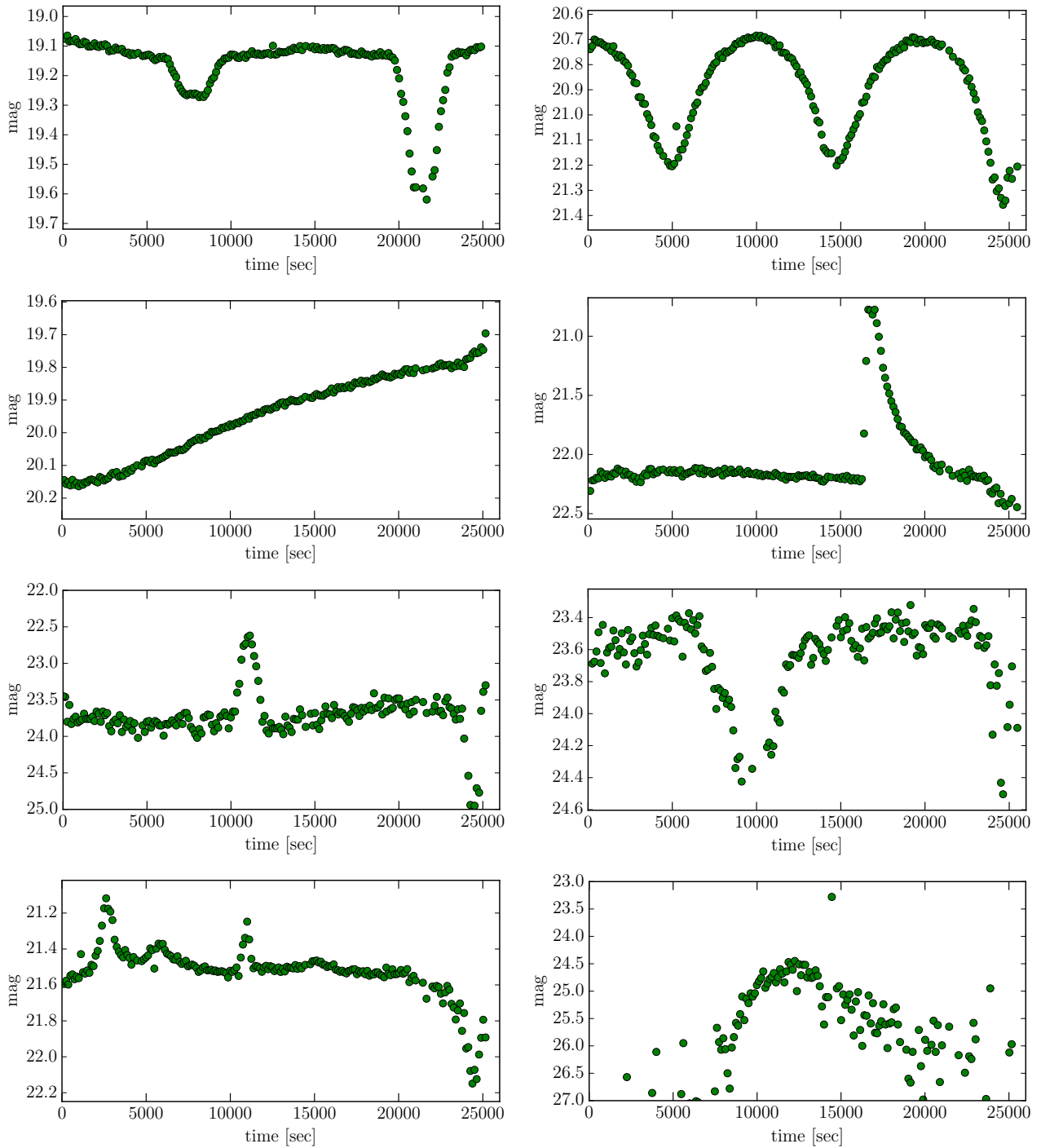


Figure 3.15: Examples of the light curves for different types of variable star candidates, as described in § 3.3.2. The panels in the left column, from top to bottom, show candidates of eclipse binary system, Cepheid variable star, moving object in the Solar system, and deflection spikes. Similarly, the panels in the right column show candidates of binary star system, star flare, a star near to CCD chip edge, and RR-Lyrae variable star. Left column shows candidates of eclipsing binary stars, Cepheid variable star, moving object in the Solar System, and magnification due to mirroring spikes; while right column displays candidates of binary star, flare star, star close to CCD edge, and candidate of RR-Lyrae variable star, from top to bottom. More details and examples are described in Appendix B and C.

by an almost exponential decay, we classify the candidates as a stellar flare. The magnification is typically 1 mag, but one candidate shows almost more than 2 magnitude magnification. Their g-r colors indicate that most candidates are M-type stars. Hence, these flare stars are likely to be in the MW halo region. Prominent star flare is a well-known phenomena for a M-type star, and originates from a reconnection of the magnetic field in the atmosphere as observed in the Sun. We didn't find a flare candidate for G-type star. This is consistent with the previous work, which shows that M-stars have more frequent flare events because energetics in the atmosphere is more affected by their magnetic field compared to G-type stars (Moffett 1974; Lacy et al. 1976; Henry & Newsom 1996).

- Moving objects: asteroids in the Solar system

These candidates are main confusion to microlensing search. These candidates display a Gaussian-shape curve at the fixed WCS position. However, after more careful look of these candidates, we found that these candidates are moving objects: point-source images in the time-sequential difference images display a clear trail in the postage-stamp image region. Hence, we consider these candidates as asteroids or comets in the Solar system. We have so far found two promising candidates of asteroids.

- Fake candidates near to the edge of CCD chip

We sometime found fake candidates that are around pixels within a few pixels from CCD chip edge. These are electrostatic effects near the edge of CCDs (a few pixels for our Hamamatsu CCDs) which means that the photometry is incorrect. This magnification feature is unique property for shot-period sampling: from the same test as discussed in § 3.3.2, we found that candidates from longer sampling selection are not sensitive to this incorrect photometry. One example is displayed in Appendix B.

- Artificial candidates due to imperfect photometry correlated with seeing size

These are fake candidates whose light curve is as shown in Fig. 3.14. Even if we identify a candidate from a PSF-like source in the difference image and then make the photometry to measure the light curve from the time-sequential difference images, the resulting light curves has a similar shape or correlation with seeing size. Hence, we conclude that this is due to an imperfect subtraction of the reference image from the target image due to the imperfect PSF measurement. Hence, we think that the light curve has a correlation with the seeing size. In particular, the exposures around ~ 3500 and $\sim 14,000$ sec have a bad seeing ($\sim 1.0''$), and the light curve shows a feature (e.g. bump or dip) around the particular epochs. When a CCD pixel has a defect, it sometimes causes an artificial image in the difference image. Furthermore, we sometime found artificial candidates in the vicinity of a bright star due to the imperfect image subtraction. After checking these images by visual inspection, we identify these fake objects. Some examples are shown in Appendix B.

- Candidates whose light curve peaks at the best-seeing epochs

1,000 candidates have a similar light curve which peaks at the best-seeing epochs. The exposures of best-seeing conditions are deepest, and the PSF photometry at the candidate position has least contamination from the surrounding stars. Most candidates have a peak magnitude of $r \sim 24.5 - 25$, and the distribution of these candidates is across the halo region of M31. If these candidates are RR-Lyrae variable stars, which have an absolute magnitude of $r \sim 1$ mag, the apparent magnitude is consistent with the hypothesis that the RR-Lyrae stars are in 750 kpc distance, which is the distance to M31. However, selection from color

criteria of the Solar spectral models suggests that many of them are M-type or K-type stars, which is inconstant with empirical law that RR-Lyrae variables tend to be A-type or F-type stars. Still there are more than 100 candidates of A-type or F-type candidates. Note that currently we cannot distinguish these candidates from fake candidates (see the detail in § 3.3.2).

Following the above study we also get some indication of event properties as follows:

(1) Frequency of time variables for each type of variable stars

Our observation has unique property that many light curves has a peak $\sim 11000\text{sec}$, around the best seeing period as displayed in Fig. 3.14. To see if these peaks are real, we imposed another detection conditions as following § 3.2.3: first separate all images into even-odd groups using serial numbers. For each group we conducted the same detection tests as mentioned before; imposing selection conditions to the each stacked images that are composed of five time-sequential images. The final time-variable candidates are constructed from those which passed the conditions more than twice. Therefore we construct two sets of candidates which can imply for the variable stars with timescale longer than 20 minutes.

We compared the two results of even-odd tests with the candidates of 10 minutes cadence, derived from § 3.2.3. The candidates are be classified into three groups by the detection frequency and property: the first group including those detected in both even-odd cases, the second corresponding to those detected either in even-odd criteria, and the third constructed by those detected in only in previous analysis. The first group includes candidates that are feasible, most of which contain smooth curve or bumps; characteristics often seen in Cepheid stars or binary stars. Also the candidates categorized in the third group are likely to be fakes because many of them have noisy behavior or log-flux peaks. The unique event with peaks around the best seeing are contained in all three group sets, with almost the distribution for three cases. The same is true for events with sub-peaks correlated with the variation of seeing. Although we cannot get clear implications for the seeing-correlated events, this sampling rate test can work as a way to remove fake candidates.

(2) Color and magnitude property

Color and magnitude are important rulers to measure the stellar property. In this study we classify the time-variable candidates with these properties. Fig. 3.16 shows the results. Color selection suggest that many variable candidates have colors corresponding to low temperature stars, with similar distribution as suggested by faint star distribution. Also, most of stars in M31 disk have similar color or magnitude properties with $g-r \sim 0$.

3.4 Searching for microlensing events of PBH for cadence M31 observation

As we have so far described, we found about 11,000 time-variable candidates from our analysis. We search, from the host sample of candidates, for microlensing events due to primordial black holes that might exist in the halo regions of MW and M31. After briefly reviewing basic properties of microlensing, we estimate an expected event rate of the microlensing for stars in M31 assuming that all the dark matter in halo regions of WM and M31 are PBHs of an assumed mass scale.

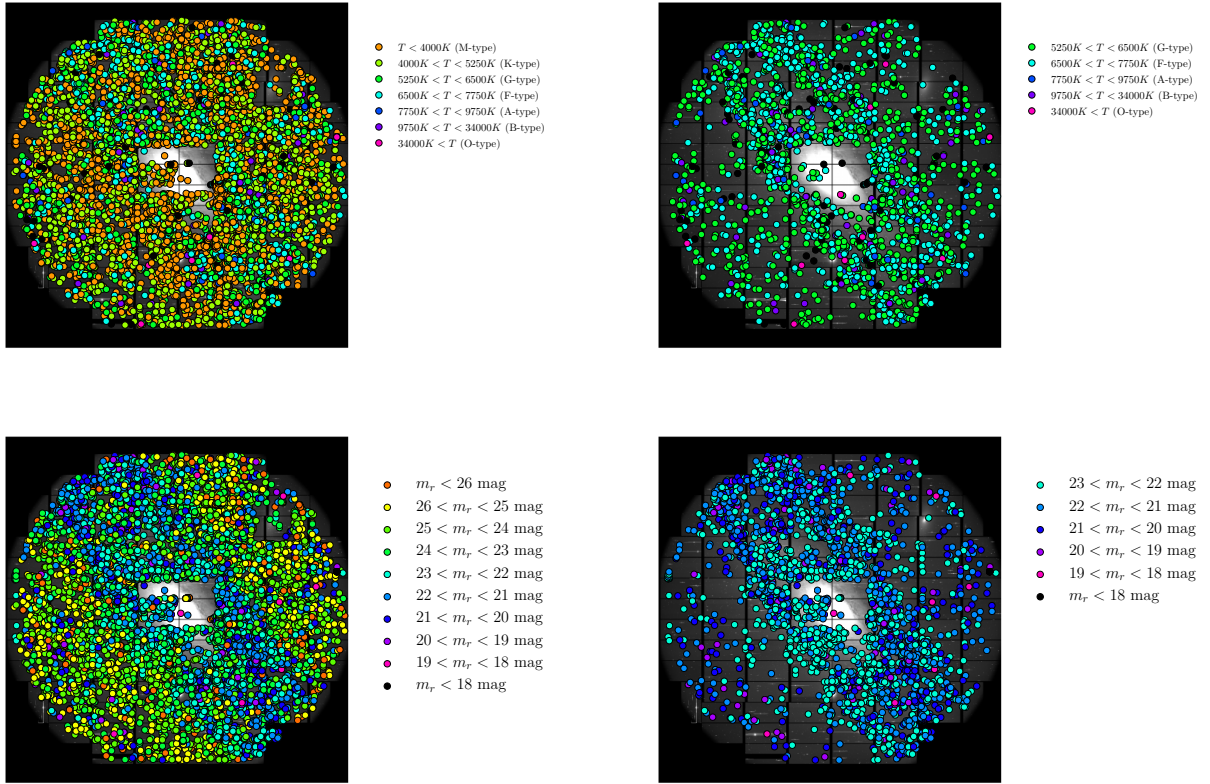


Figure 3.16: Event classification from color and magnitude implications. *Upper panels:* candidates categorized by $g-r$ color conditions; each star-type category is calculated by combining HSC filter model as displayed in Fig. 3.3 and stellar spectrum of Kurucz air model (here we adopt solar type stars of Kurucz 1993). Note that we only take into account temperature information for stellar-type classifications. Left panel shows all candidates, and right panel excludes stars with low temperature. *Lower panels:* candidate distribution classified by r -band magnitude in the reference image. Left panel shows all candidates, and right panel shows only those brighter than 23 magnitude.

We then use a simulation of the microlensing taking into account observational conditions and noise in order to estimate a detection efficiency of the microlensing events. Finally we estimate a number of source stars in M31 from the HSC data and then derive constraints on the abundance of PBHs from our search of the microlensing events.

3.4.1 Basic properties of microlensing events from Massive Compact Halo Objects (MACHOs)

In this section we briefly summarize microlensing properties. We especially take into account the pixel lensing regime in our survey, where we need additional care other than basic canonical microlensing scheme.

(1) Optical depth of microlensing event

We consider a microlensing event illustrated in Fig. 3.17 following Paczyński (1986). Here we define, by “microlensing”, as a phenomena where a background source enters within an Einstein radius of PBH on the sky, leading to a large magnification effect on the background

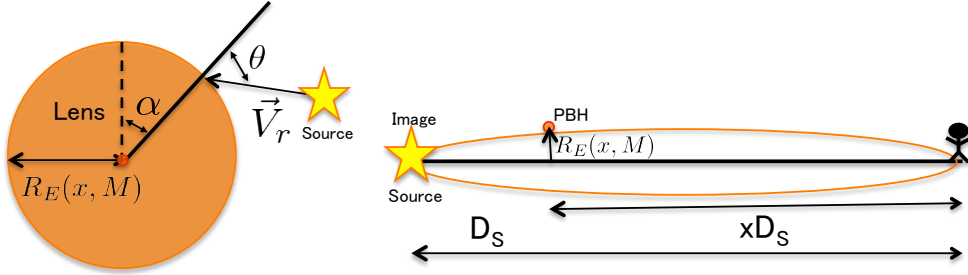


Figure 3.17: The systems describing gravitational microlensing effect. Left figure shows a case when a source star enters the Einstein radius of a lens star. Right figure describes the simplified system of Fig. 3.1; light from source object are bent to form multiple images, but their separation is too small to be resolved for us.

source: $r_0 < R_E$. If we consider a distribution of PBHs in between an observer and a source star, which are PBHs in halo regions of MW and M31 for our case, we can define an optical depth of microlensing for a source star:

$$\tau = \int_0^{D_S} n(D_L, M) \pi R_E^2(D_L, M) dD_L \quad (3.15)$$

where $n(x, M)$ is the number density of PBHs with a single mass M and at distance $x D_S$ from an observer. R_E is the Einstein radius defined as

$$R_E^2 = \frac{4GM D}{c^2}, D = \frac{D_L D_{LS}}{D_S} = D_S x(1 - x) \quad (3.16)$$

where D_L , D_{LS} and D_S are the distances between the observer and the lens PBH, the lens and the source star, and the observer and the source, respectively. Then we can rewrite optical depth using the average mass density $\rho = nM$:

$$\tau = \int_0^1 \frac{4\pi G D}{c^2} \rho(x) dx \quad (3.17)$$

Thus optical depth τ does not depend on the mass of MACHOs M , and only depends mass density $\rho(r)$ as a function of the distance from galactic center r . Note that we throughout this paper consider the optical thin limit, $\tau < 1$.

Next we model the mass distribution between M31 and us in the Milky Way Galaxy (MW). We assume that the dark matter distribution in each halo region of MW or M31 is given by an Navarro-Frenk-White (1997; hereafter NFW) model

$$\rho_{\text{NFW}}(r) = \frac{\rho_c}{(r/r_s)(1 + r/r_s)^2}, \quad (3.18)$$

where r_s is the scale radius and ρ_c is the central density parameter. We adopt $\rho_c = 1.40 \times 10^7 M_\odot/\text{kpc}^3$ and $r_s = 16.1$ kpc for MW (Nesti & Salucci 2013), and $\rho_c = 4.05 \times 10^7 M_\odot/\text{kpc}^3$ and $r_s = 8.18$ kpc for M31 (Geehan et al. 2006). These NFW profiles are shown to reproduce the observed rotation curves for MW and M31, respectively (Klypin et al. 2002). Taking into account the fact that the Earth (an observer) is placed at distance, $R_\oplus = 8.5$ kpc, from the MW center, the distance to a PBH at distance D_L is given as

$$r(D_L) = \sqrt{R_\oplus^2 - 2R_\oplus D_L \cos(l) \cos(b) + D_L^2} \quad (3.19)$$

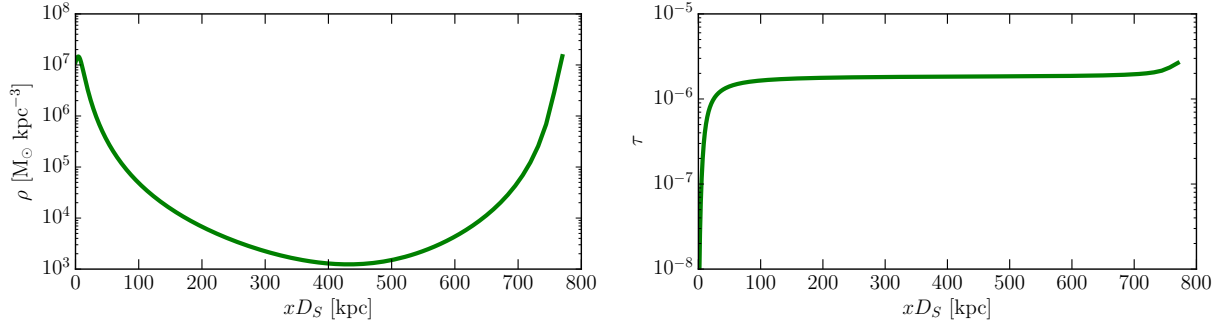


Figure 3.18: Left panel: Mass density profile as a function of distance from the Earth (an observer) in the direction to M31. We assume that the Earth is at 8.5 kpc from the MW center. We assume NFW profiles for the mass density profiles either of which is consistent with the observed rotation curve of MW or M31 as proposed in Klypin et al. (2002). The mass density profile is given by a superposition of the two NFW profiles. Right panel: The differential optical depth of microlensing due to PBH of mass $10^{-7}M_{\odot}$ at the distance $x D_S$ [kpc] ($D_S = 770$ [kpc], $0 < x < 1$) from an observer, for a star in M31. Here we assumed that the mass in the MW and M31 halo regions is fully composed of PBH.

where we assume the M31 position in Galactic coordinates as $l = 121.2^{\circ}$, $b = -21.6^{\circ}$ as mentioned in § 3.2.1, the distance to M31 is $D_S = 770$ kpc. As for M31 halo profile we take into account the location of the targeting field (patch=2,6), which is ~ 6.7 kpc away from the M31 center. The left panel of Fig. 3.18 shows the mass density profile as a function of distance from the Earth towards to M31, while the right panel shows the differential optical depth; integrating the curve up to a given distance, $x D_S$ (x axis) gives the optical depth. Thus optical depth for a star in M31 is $\tau \sim 2 \times 10^{-6}$, that means that microlensing is very rare even for a single source star. However, we consider a millions of source stars in M31, we expect one event, if dark matter in halos of WM and M31 is made of PBHs.

Note that one can calculate optical depth from the property of microlensing event detected. The estimator is given by

$$\tau_{\text{obs}} = \frac{1}{E} \frac{\pi}{4} \sum_i \frac{\hat{t}_i}{\epsilon(\hat{t}_i)} \quad (3.20)$$

where \hat{t}_i is typical timescale of microlensing, $\epsilon(\hat{t}_i)$ is detection efficiency for i -th microlensing event, and E is the total exposure in the unit of [The number of stars observed(star) \times observation length(years)]. Thus optical depth can be a indicator of halo models by comparing the model estimator with observation.

(2) Expected event rate

In the following we calculate the expected number of microlensing events of PBHs per unit observation time – i.e. expected even rate. If a source star moves across the Einstein radius, with a relative velocity on the sky, v , the time scale of microlensing is computed as

$$T = \frac{2\sqrt{R_E^2 - d^2}}{v} = \frac{2}{v} \sqrt{\frac{4GMD}{c^2}} \sqrt{1 - \beta^2} = 2t_0 \sqrt{1 - \beta^2} \quad (3.21)$$

where R_E is the Einstein radius, d is the shortest separation between star and PBH, and $\beta \equiv d/R_E$ is the impact parameter. To model the velocity component, we assume that

each PBH in the halo region of MW or M31 moves according to the gravitational force of the interior mass at the PBH position:

$$V_{\text{halo}} = \sqrt{\frac{GM_{\text{ran}}(< r)}{r}} \quad (3.22)$$

where $M_{\text{ran}}(< r)$ is the interior mass at radius r from the center, defined as

$$M_{\text{ran}}(< r) = 4\pi\rho_s r_s^3 \left[\ln(1+x) - \frac{x}{1+x} \right], \quad x = r/r_s \quad (3.23)$$

The typical time scale of microlensing can be estimated as

$$\hat{t} = 2t_0 \simeq 3.5\text{hours} \left(\frac{M}{10^{-7}M_\odot} \right)^{\frac{1}{2}} \left(\frac{x D_S}{100\text{kpc}} \right)^{\frac{1}{2}} \left(\frac{v}{200\text{km/sec}} \right)^{-1} \quad (3.24)$$

Here we employed $V_{\text{halo}} = 200\text{km/sec}$ for the typical velocity v , and considered PBHs with mass scale of $10^{-7}M_\odot$ and at distance 100kpc from us, as an example. Therefore the event rate of microlensing can be calculated as:

$$\Gamma = \frac{4}{\pi} \frac{\tau}{\hat{t}} = 0.91 \left(\frac{M}{10^{-7}M_\odot} \right)^{-\frac{1}{2}} \left(\frac{x D_S}{100\text{kpc}} \right)^{-\frac{1}{2}} \left(\frac{v}{200\text{km/sec}} \right) [\text{events/star/year}] \quad (3.25)$$

Next we take into account the velocity dispersion of PBH for precise modeling by assuming the Maxwell distribution:

$$f(v; r) = \frac{1}{\pi^{\frac{3}{2}} v_c^3} e^{-\frac{v^2}{v_{\text{halo}}^2}} d^3\vec{v} \quad (3.26)$$

Then the event rate can be expressed in the cylinder coordinate $d^3v = v_r dv_x dv_r d\theta$ as: (Griest et al. 1991)

$$d\Gamma = \frac{\rho(r)}{M} f(v) v_r^2 \cos\theta r_E dv_x dv_r d\theta d\alpha dx \quad (3.27)$$

where we assume that velocity direction of PBH is isotropic, and the mass density is consisted of NFW density profiles of MW and M31 halo. The integral can be calculated by substituting the variable as: $\hat{t} = \frac{2R_E}{v_r}$. Therefore the event rate of microlensing is given by:

$$\frac{d\Gamma}{d\hat{t}} = \frac{32D_S}{\hat{t}^4 M v_c^2} \int_0^1 \rho(x) R_E^4 e^{-\frac{4R_E^2}{\hat{t}^2 v_c^2}} dx \quad [\text{events/star/year}^2], \quad (3.28)$$

As for PBH in MW halo, we convert the lens distance r , originally expressed in the galactic coordinate (l, b) to the the distance x normalized by D_S following the same way as in Eq. 3.19: $r^2 = R_\oplus^2 + (x D_S)^2 - 2R_\oplus x D_S \cos l \cos b$, where R_\oplus is the distance from the solar system to the Galactic center. Fig. 3.19 displays the event rate for lens PBH in either MW halo or M31 halo, and source stars in M31 ($D_S = 770\text{ kpc}$). We calculated for cases with PBH mass of $M = 10^{-7}-10^{-9}M_\odot$. The event rate for PBH mass M can be calculated by scaling the $m = M_\odot$ case with \sqrt{M} for horizontal axis and M^{-1} for vertical axis. The left panel of Fig. 3.19 shows the expected event rate from our data, showing that PBH in mass

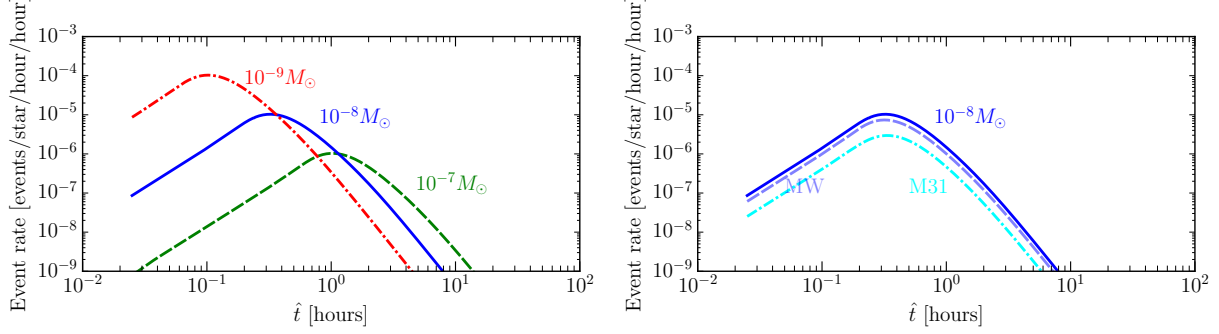


Figure 3.19: The differential event rate of microlensing due to PBHs, per unit observation time (hour), per a single star in M31, and per unit time scale of microlensing (hour). The x-axis is the timescale of microlensing. Here the mass distribution of MW or M31 halo region is given by the NFW profile, all the dark matter is made of PBHs, and we considered PBHs with mass 10^{-9} , 10^{-8} or $10^{-7}M_{\odot}$, respectively. The lighter PBH has a shorter microlensing time scale. Right panel shows the relative contribution to the microlensing rate due to PBHs in either MW or M31 halo region.

range $10^{-9}M_{\odot} - 10^{-7}M_{\odot}$ has maximum event rate in our sampling rate. Also one example of the contribution from PBHs in the two halos is given in the right panel.

We can calculate the total event rate by integrating Eq. 3.28 with \hat{t} :

$$\Gamma = \int_0^{\infty} \frac{d\Gamma}{d\hat{t}} d\hat{t} = 1.7 \times 10^{-6} \left(\frac{M}{10^{-7}M_{\odot}} \right)^{-\frac{1}{2}} \quad [\text{events/star/hour}] \quad (3.29)$$

The average timescale $\langle \hat{t} \rangle$ is also given by:

$$\langle \hat{t} \rangle = \frac{1}{\Gamma} \int_0^{\infty} \hat{t} \frac{d\Gamma}{d\hat{t}} d\hat{t} = 1.8 \left(\frac{M}{10^{-7}M_{\odot}} \right)^{\frac{1}{2}} \quad [\text{hour}] \quad (3.30)$$

(3) Light curve characterization in pixel lensing regime

The property of microlensing event is characterized by two factors: magnification amplitude and event duration. These two quantities are characterized by the Einstein time scale t_E and the maximum magnification of the light curve, A_0 .

As we described, our definition of microlensing is the case that a source star enters within the Einstein radius of PBH, which correspond to the magnification $A > 1.34$. In the pixel lensing method we need to discriminate the lensed star from other stars. When extracting the physical parameters from the observed light curve of microlensing, it is known that the fitting gives a strong degeneracy between the Einstein time scale (t_E) and the impact parameter β (Gould 1996; Baltz & Silk 2000).

In order to quantify the microlensing event, we adopt two observables for characterizing the events following Riffeser et al. (2006): the full-width-half-maximum timescale of the event (t_{FWHM}) and the flux excess above the background (ΔF). These two quantities are related to the canonical microlensing parameters as following: First we characterize the event duration as the full width of the half-maximum peak in the light curve. By definition, t_{FWHM} of a light curve can be described as:

$$A \left(\frac{t_{\text{FWHM}}}{2} \right) - 1 \equiv \frac{A_0 - 1}{2} \quad (3.31)$$

where A_0 represents the maximum magnification of the light curve. Here we will characterize the timescale as a function of impact parameter β , the quantity described as u_{\min} in Eq. (3.10). Then we can rewrite the timescale in the same way as described in Gondolo (1999):

$$t_{\text{FWHM}} = t_E \omega(\beta) \quad (3.32)$$

where

$$\omega(\beta) = 2\sqrt{2f(f(\beta^2)) - \beta^2}, \quad (3.33)$$

$$f(x) = \frac{x + 2}{\sqrt{x(x + 4)}} - 1 \quad (3.34)$$

where $\omega(\beta)$ satisfies $\omega(\beta \ll 1) \simeq \beta\sqrt{3}$, and $\omega(\beta \gg 1) \simeq \beta(\sqrt{2} - 1)^{0.5}$. Next we describe another parameter to represent the amplitude of light curve. In image difference technique it is much convenient to adopt the maximum flux of the event instead of maximum magnification:

$$\Delta F_{\text{max}} = F_0 \left(\frac{\beta^2 + 2}{\beta\sqrt{\beta^2 + 4}} - 1 \right) \quad (3.35)$$

where ΔF represents the excess flux due to microlensing effect. Following the image difference technique we can set the detection threshold flux ΔF_{det} as: $\Delta F_{\text{det}} \equiv F(t) - F_{\text{ref}} = \Delta F_{\text{bl}} + F_0(A(t) - 1)$. Note that $\Delta F_{\text{bl}} = 0$ holds for case where the source is not affected by gravitational lensing effect.

3.4.2 Current status: constraint of PBH abundance from HSC M31 data

In this section we describe the current status of microlensing analysis. Here we briefly summarize the results of our analysis using the data of one patch region alone, “patch=2,6”, which is located between the halo and disk regions of M31.

(1) Null test

A detection efficiency of microlensing event is sensitive to the noise properties in the difference image. To estimate the noise field in the difference image difference, we use the following method. We first randomly select 1000 points in a bank region of the difference image (excluding the region of a candidate). Second we make the PSF photometry of the random points. Then we compute the variance of the PSF magnitude, which gives us an estimate of the noise field in the patch. Note that, in estimating the noise variance, we performed the median background subtraction in the difference image of the patch as we described above.

Fig. 3.20 shows the case with noise threshold 1σ , 3σ and 5σ flux converted to magnitude unit. On each panel, square symbols are tests with difference images constructed from time-sequentially five-stacked images, and circle marks are tests with difference images of each visit. We used the former images for detection and the latter images for photometry.

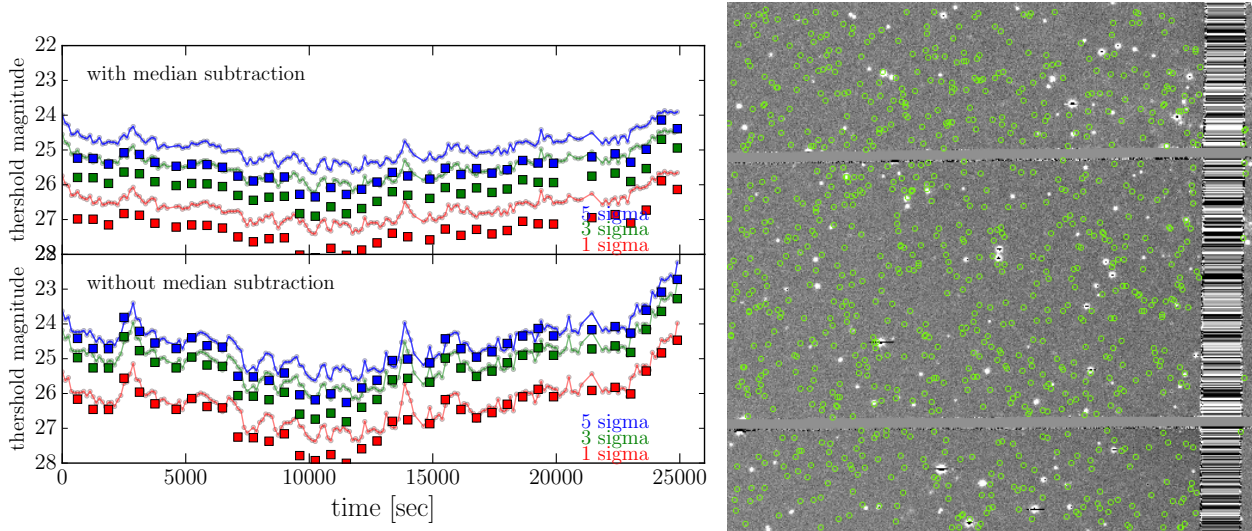


Figure 3.20: An estimation of noise variance in the difference image. Here we show the results for the difference image of patch=2,6 as an example. We randomly select 1000 points in a blank region of the difference image (as shown in the right panel), measure the PSF magnitude of each point and then estimate the variance of PSF magnitude. The left panels shows the noise variance, 1, 3 or 5sigma, as a function of observation time. The square symbols show the results when using the coadd images of 5 time-sequential exposures for the difference image. The circle symbols, connected by the line, are the results for each exposure. The difference in the upper and lower plots, in the left panel, is with or without the median background subtraction of the difference image.

As expected, the noise gets smaller when we stacked five images than cases with each image. Also it is proved by comparing the upper and lower panels that the threshold gets smaller for the measurement with local median subtraction. The results imply that stars with base magnitude 25 or 26 magnitude are around the borderline for 5 or 3 sigma noise thresholds respectively.

(2) Magnification threshold from photometry error

Until now, we define magnification threshold of microlensing event as $A > 1.34$ in this experiment. To see if the threshold is proper, we looked into the uncertainty of PSF photometry. Fig. 3.21 shows the magnitude or PSF flux error distribution of field stars on the reference image. The error distribution indicates that stars with PSF flux ~ 0.6 [ADU] at 90 sec exposure, corresponding to stars brighter than 25.8 mag can barely probe $A > 1.34$ magnification. Although this flux error comes from reference image and the measurements on difference images might have different effect, we conclude that 3σ threshold Fig. 3.20 can work as noise threshold by comparing the result in the upper panel.

(3) Detection efficiency

We have so far employed the formal definition of microlensing that a source star should be within the Einstein radius of a foreground PBH, corresponding to the magnification $A > 1.34$. However, it is unclear whether the lensed source can be detected by our observation. The detection threshold should depends on the intrinsic brightness of a source star, the noise field in the difference image, the amount of lensing magnification, and the time-scale of light curve in order for us to capture the light curve within our observation time duration (7 hours). Thus we need to properly estimate the detection efficiency.

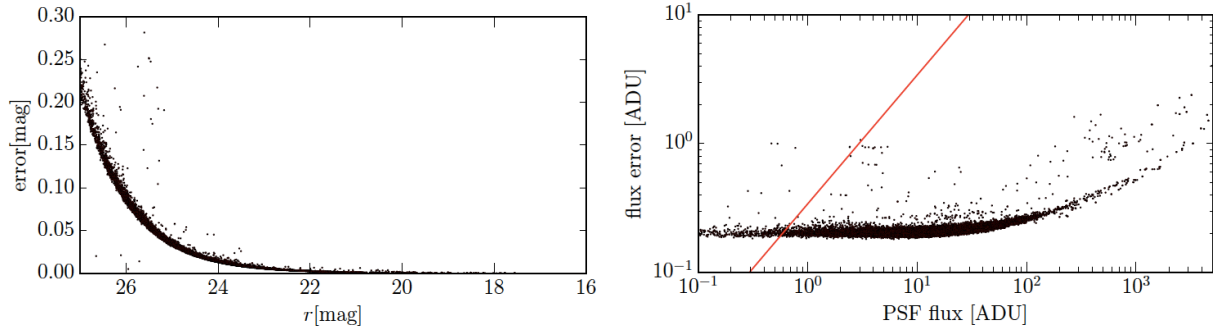


Figure 3.21: Uncertainty of star flux in our data. Left panel shows PSF magnitude errors of each star. The star samples are constructed from the star catalog of the targeting field (the detail of catalog property is described in § 3.4.2). Right panel displays the PSF flux error in the unit of ADU for the same star samples of 90 sec exposure. The red line corresponds to the border line that flux error is above or under 0.34 times of PSF flux, which indicates that stars with PSF flux larger than the line can overcome the magnification condition: $A > 1.34$. The error distribution indicates that stars with PSF flux ~ 0.6 [ADU] at 90 sec exposure, corresponding to stars brighter than 25.8 mag can barely probe $A > 1.34$ magnification.

Detection efficiency is simply given by $\epsilon(\hat{t}_i) \equiv (\text{The number of detected events}) / (\text{Total number of events occurred})$. In the following we discuss the two kinds of tests performed for efficient estimation; one with simulated light curves, and the other with embedded candidates in the image.

a) *efficiency test with light curve simulations*

First we studied the event property with simulation of microlensing light curves. The theoretical light curves are constructed by mimicking our detection method as in § 3.2.3; we simulated the time-variased flux of each event in the difference images. For each event we change the conditions using three parameters; Einstein time scale t_E , impact parameter β , and the time when maximum amplification occurs t_{\max} . Note that impact parameter is decided to meet the condition $0 < \beta < 1$, and typical time scale t_{FWHM} and maximum flux parameter ΔF_{\max} are calculated from the above parameters. Also for excess noise parameter, we correct for the base flux in the same way as derived from image difference technique; the reference magnitude is constructed from the average of 10 best-seeing frames.

By assuming cases with the PBH mass $10^{-7}M_{\odot}$, we created every 1000 events for different t_{FWHM} , and counted the number of events when more than three data points continuously passed the 3σ noise threshold as in the upper panel of Fig. 3.20. For the event time scale we take 5 minutes for the minimum so as to have more than three data points above the noise threshold. We also take 11 hours as the maximum timescale because events longer than this timescale have longer half-width-half-maximum than the total observational time, which makes it difficult to discriminate the microlensing event with other variable star such as Cepheid variable stars. On each light curve we add the flux noise to the simulated microlensing flux measured at the random point in the difference image. One example of simulated light curve is given in Fig. 3.22. Note that 1000 points are selected by avoiding the CCD edge region, because we cannot measure the flux property at that point.

Fig. 3.23 describes the detection efficiency for events with different timescale and

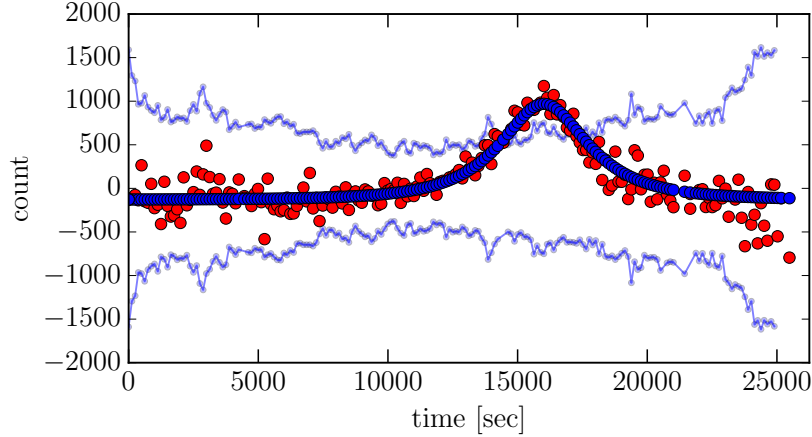


Figure 3.22: One example of simulated light curve of a microlensing event in the difference image. Red points indicates the simulated light curve, taking into account the flux noise at an assume position in the difference image at a given time. Smooth blue points is the fitting curve of the simulated light curve, and faint blue lines in the background represents the 3σ noise threshold.

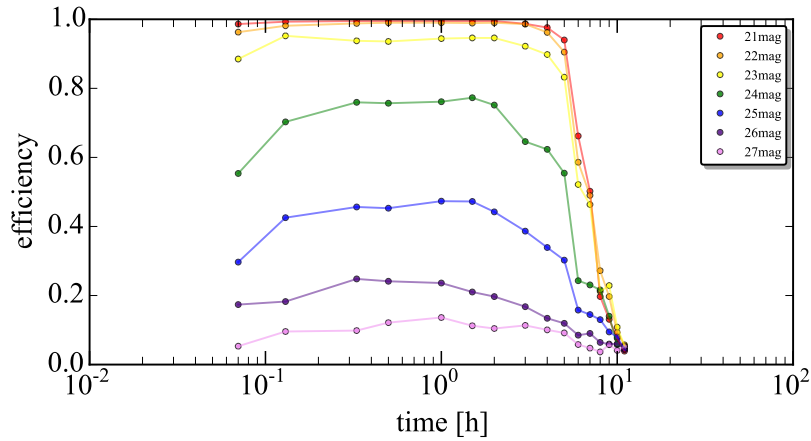


Figure 3.23: The detection efficiency estimated from light curve simulations taking into account the noise field in each difference image of 194 target images we used for the analysis (see text for details). Here we generated Monte Carlo simulations of microlensing events randomly varying the two parameters: the impact parameter (or maximum lensing magnification) and the FWHM time scale parameter, for source stars of a fixed magnitude as indicated by legend. The x-axis is the microlensing time scale. The detection efficiency for each source magnitude is estimated from 1,000 realizations.

source magnitudes. There exist drastic drops of detection efficiencies for events longer than the observational period, longer than 7 hours. one reason for this effect is that fitting by theoretical microlensing light curve does not work for these events because of unstable baseline. For events with time scale shorter than observational period, the detection efficiencies are almost constant for stars brighter than 23 magnitude. On the other hand, when the source stars fainter than 24 magnitude have lower detection efficiency, which indicates that faint stars need some specification to pass the threshold. Another characteristics of detection efficiency is that it takes lower value for events with shorter time scale. This is reasonable for shorter events because it is hard for them to pass the threshold when magnification peak falls in high noise period.

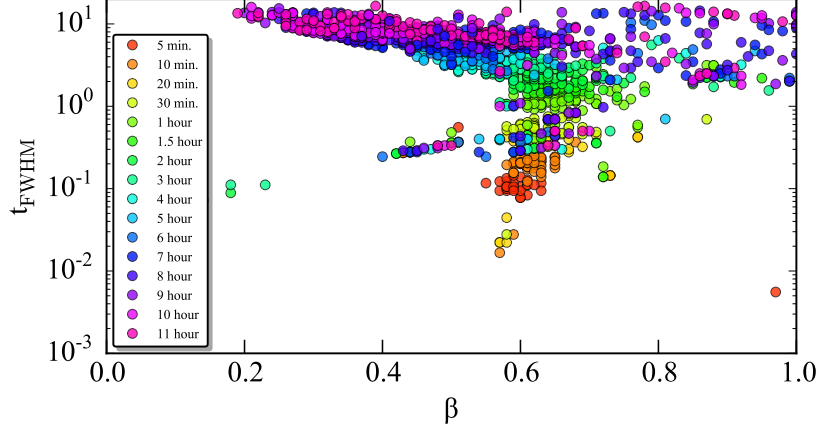


Figure 3.24: The distribution of microlensing parameters for source stars with 24 magnitude. Each point is derived by the fitting of a simulated light curve. We tested 400 events for every event with different time scale. Here we perform the fitting with two parameters; impact parameter β and timescale parameter t_{FWHM} , and the maximum time of the event t_{max} is fixed at the time of maximum flux.

We also looked into parameter properties that meet the selection conditions, just by fitting the simulated light curves with theoretical microlensing prediction. To simplify the case, we fit the light curves with t_{FWHM} and β parameters, and fix t_{max} as the time of maximum peak during observation. Fig. 3.24 shows the best-fit parameter distribution derived from simulated events of 24 magnitude. This figure indicates that β has some threshold for all the time scale, suggesting that events are detected only when source stars come close enough to the center of PBH lens in the line of sight.

b) *efficiency test with fake object simulations*

We performed another test to estimate the detection efficiency in more concrete way; burying fake microlensing stars in the observational CCD imaging data and proceed the same analysis as mentioned in § 3.2.3. Thus we can include the PSF smoothing effect followed by the stacking or subtracting procedures, which might affect the flux count in the output images. Also we can take advantage of the same detection condition, including shape conditions or the residual condition, which are all neglected in the light curve simulations.

Fake stars simulations are all performed by *fake-pipe* module installed in HSC-pipe, which enables one to bury fake stars in CCD reduced image by means of PSF information in that field. In order to study the detection efficiency we buried 1000 stars at random position, avoiding the CCD edge regions. The flux variation due to microlensing effect are calculated in the same way as we performed in the light curve simulation; taking t_E , β , and t_{max} as free parameters.

Fig. 3.25 shows the comparison of detection efficiency derived from the different tests: light curve simulation, light curve simulation with successful fitting, and burying tests. Among the results from source stars of 24 magnitude, burying test implies slightly smaller efficiency compared to tests with simulated light curve. This might come from the additional performance of HSC-pipe for the subtraction and detection in the difference images. In the following we adopt the implications from simulated light curves although the estimation is very optimistic.

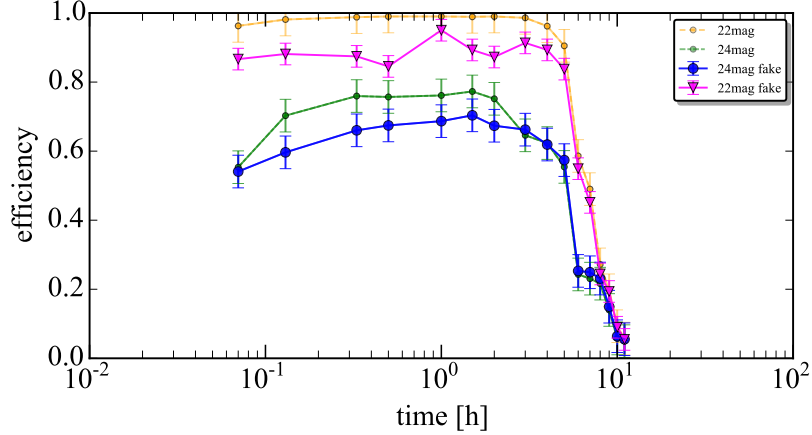


Figure 3.25: Comparison of detection efficiency from different tests, focusing on the results from stars with 22 and 24 magnitude (All the error-bars come from Poisson noise). Small circles show the results from light curve simulations (the same as shown in Fig. 3.23), and large marks represent the results from fake image simulations, where we inject fake point source in the real image and performed the same analysis of microlensing search.

(4) Star number counts in HSC M31 data

The expected number of microlensing events in a field greatly depends on the number of source stars in that field (see the detail in § 3.4.3). However in M31 field, it is hard to estimate the star number counts because multiple stars are expected to exist in one pixel and cannot be resolved; the situation so-called pixel lensing regime. In the following we describe our test in the targeting field to seek for better estimation way of the star number counts .

In the first step we take a look at the star property in the targeting field by taking advantage of the reference image with seeings ~ 0.45 . Even in the pixel lensing regime, stars in M31 halo region are almost resolved with the help of high resolution. Therefore we constructed two kinds of star catalogs by HSC-pipe, and look into the properties. The properties of two catalog are summarized as follows:

- (1) *Star catalog constructed by HSC-pipe* — containing stars detected by *multiband.py* programs, which performs auto-deblending procedures. Photometry was performed on fixed point with PSF magnitude. Due to the failure of the program, stars are selected only from partial regions.
- (2) *Peak catalog* — including the positions of auto-detected peaks by HSC-pipe. For each peak we perform PSF photometry. The distribution of peaks is spread all over the image, but some magnitude threshold might prevent the detection of dark candidates.

Fig. 3.26 shows the magnitude distribution of stars for three regions: halo region, targeting region in-between halo and disk, and bulge region. Basically two catalogs have similar distribution, but the number counts from star catalog tends to be lower than that of peak catalog due to the lack of analyzed region in star catalog. Also for distribution of number counts, star catalogs tend to have log-declined slope in the fainter end while peak catalogs have magnitude threshold, both of which is inconsistent with the monotonic increase tendency suggested by empirical star luminosity function (ex. Mamon & Soneira 1982). We also calculate the sum of pixel count with PSF count from catalog, with the

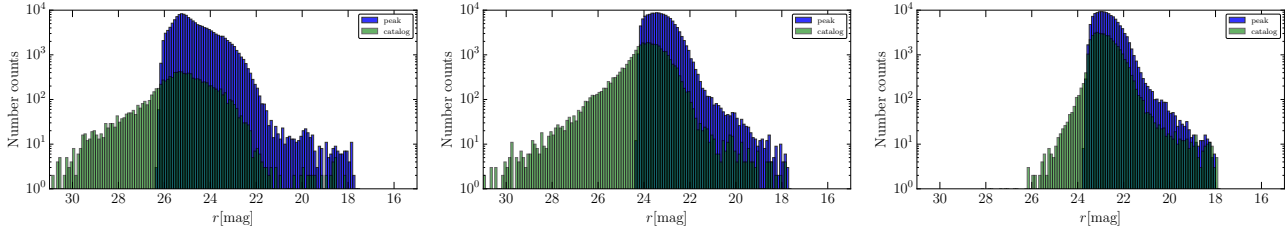


Figure 3.26: The number counts of stars in some patch regions of M31. Here we employ 0.1 mag for the magnitude binning, and considered two different catalogs of stars. The blue histogram shows the number counts for stars that are identified by the HSC pipeline based on the imposed conditions. The green histogram shows the number counts for "peaks" that are identified from local peaks in the flux field in each image. Left panel is from M31-halo region (patch=1,5), middle panel is from halo-disk region corresponding to the targeting field in this section (patch=2,6), and right panel is from bulge region (patch=4,4).

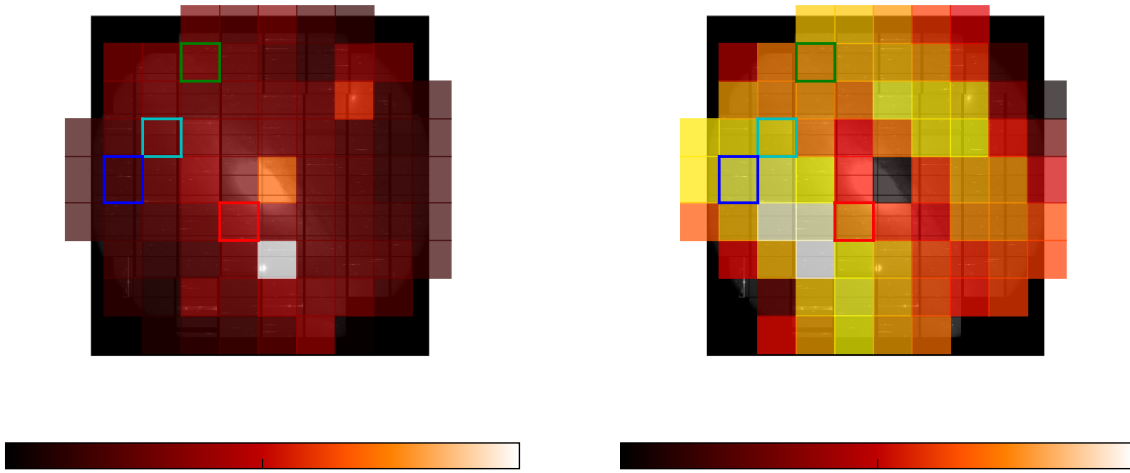


Figure 3.27: Flux and peak number counts distributions of HSC-M31 region. The rectangles in each map show analyzed regions: blue rectangle is M31-halo region (patch=1,5), cyan one is halo-disk region corresponding to the targeting field in this section (patch=2,6), green one is disk region (patch=3,8), and red one is from bulge region (patch=4,4). Both panels are plotted with linear color scales; white side of the bottom color bars means larger and black means smaller. Left panel shows the distribution of the average flux counts in the unit of patch, suggesting the existence of very bright patches around M31 bulge and NGC205. Right panel shows the distribution of the number density of peaks. The number counts of peaks is smaller for disk and bulge regions, which is inconsistent with higher pixel counts compared to halo region.

sum of the whole pixel counts in the image. The result is summarized in the following table, which indicates that the total PSF count calculated with peak positions is in the same order of total pixel count.

From the above pixel count result, we conclude that the peak catalog can basically work as star catalog of the targeting field. We also consider that the number counts can be more safely estimated by extending the threshold magnitude up to around 26 [mag] with monotonically increased counts following empirical luminosity function and the halo region case (in the left panel of Fig. 3.26).

Table 3.1: Properties of flux count and star number counts for sub-regions of HSC-M31

Region	#patch	Total pixel count	Total peak count	Total Star count	#peaks	#stars
Halo	1,5	3.11×10^6	2.34×10^6	1.52×10^5	147387	14807
Halo-disk	2,6	4.71×10^6	5.70×10^6	9.66×10^5	136933	40976
Disk	3,8	4.87×10^6	6.12×10^6	8.86×10^5	119188	32694
Bulge	4,4	5.91×10^6	1.24×10^6	2.32×10^6	124096	46904

Note: Total pixel count property in different regions; M31-halo region (patch=1,5), halo-disk region corresponding to the targeting field in this section (patch=2,6), disk region (patch=3,8), and bulge region (patch=4,4). The total PSF count of the targeting region (patch=2,6) derived from peaks is in the same order as total pixel count of that image.

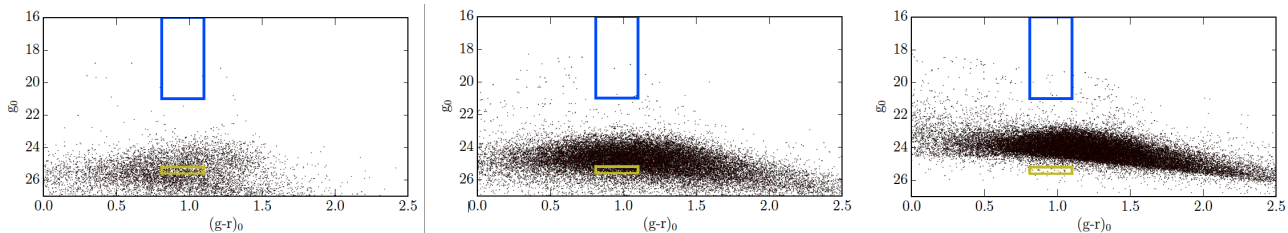


Figure 3.28: Color-magnitude diagram for three regions constructed from star catalog: halo region (patch=1,5), targeting region in-between halo and disk (patch=2,6), and bulge region (patch=4,4) from left to right. Red giants in M31 are expected to show up around $g_0 \sim 25$ mag and $(g - r) \sim 1.0$ region (corresponding to yellow box; red giants in MW is expected in blue-box region). However, we cannot study the expected clumpy property due to the failure in the debrending process of *multiband.py* program, which prevent the statistical study of the stars.

Note that there exists a conventional way to correct the field magnitude by combining extinction map and empirical luminosity function. Magnitude property differs due to the dust distribution in the field, which redden the magnitude in homogeneously even within the same galaxy, and might cause a systematic bias and large uncertainty. Extinction map can be constructed by studying the sub-field properties; taking advantage of the color-magnitude distribution of Red Clump Giants in that field (Paczynski et al. 1999). We draw color-magnitude diagram by g -band and r -band star catalog as in Fig. 3.28, and searched for red giants such as Asymptotic Giant Branch (AGB) stars by Kurucz (1993) air model. However, due to the magnitude cut in the star catalog we could not estimate the property of Red-Clump stars from the diagram.

As for magnitude bias, we take into account extinction effect when modeling the M31 halo density profile, because inhomogeneity can largely bias the microlensing result especially for M31 halo-lensing case. Currently for the self-lensing case we do not allow for the extinction effect because Andromeda Galaxy is 20 degree away from the galactic plane, which makes the inhomogeneity small enough compared to M31's contribution.

(5) Event selection on M31 data

In this section, we describe our selection criterion for microlensing events with HSC-M31 data. Basically we applied the same selection criterion as we imposed in simulation: noise

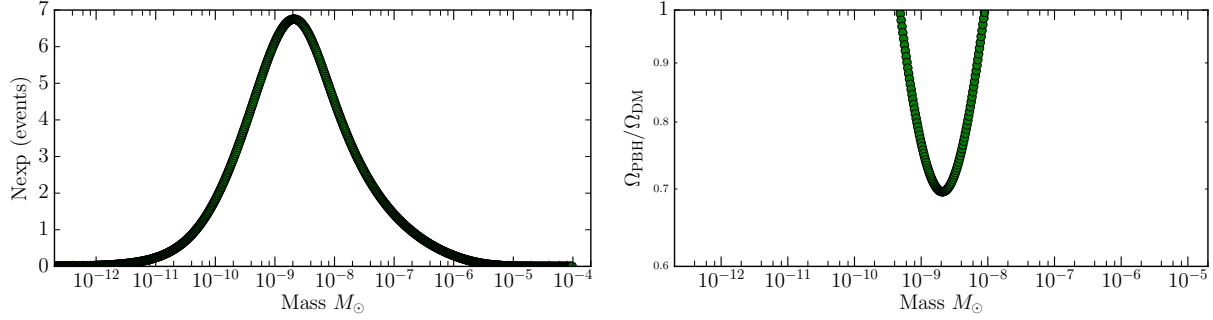


Figure 3.29: Expected number of microlensing events for source stars in the patch=2,6 region, as a function of PBH mass in the horizontal axis. The right panel shows an upper limit on the abundance of PBHs assuming we don't have any secure candidate of PBH microlensing (no detection). To convert no detection to the upper limit, we assumed that some portion of dark matter in the halos regions of MW and M31 is made of PBHs, parameterized by $\Omega_{\text{PBH}}/\Omega_{\text{DM}}$ in the vertical axis.

threshold and fitting condition. We select candidates by fitting theoretical microlensing light curve with our database, with errorbars from PSF photometry. Here we take the base magnitude A_s for the 176 candidates in targeting field of patch=2,6, for example, we have no candidate to have best-fitting parameters by successful fitting.

There are some candidates which can pass the fitting conditions. For example, the light curve of moving object, the third figure in left law of Fig. 3.15 can be fitted by microlensing light curve. As we have no criterion to clearly exclude such candidates, for now we just exclude them by comparing with image or eye-ball selections.

3.4.3 Constraint on abundance of PBHs

From the all the results above, we can derive the mass fraction of PBHs occupying the entire halo. In the following we estimate the fraction by null detection of microlensing event at the targeting field (patch=2,6). First we consider the expected number of microlensing events, taking into the account of the detection efficiency we estimated above. Here we assume the halo model of Milky Way galaxy as the standard exponential model. Then the event rate can be estimated as:

$$\frac{d\Gamma}{d\hat{t}} = \frac{32D_S}{\hat{t}^4 M v_c^2} \int_0^1 \rho(x) R_E^4 e^{-\frac{4R_E^2}{\hat{t}^2 v_c^2}} dx \quad [\text{events}/\text{star}/\text{yr}^2]$$

where M is the mass of PBHs, and \hat{t} is the duration time of the microlensing event. In the case where MACHO has flat mass distribution like delta function, the expected number of events N_{exp} with MACHOs of mass M is estimated as the integral of the event rate via \hat{t} , multiplied by duration time and the total exposure:

$$N_{\text{exp}}(M) = E \int_0^\infty \frac{d\Gamma}{d\hat{t}}(\hat{t}, M) \epsilon(\hat{t}) d\hat{t} \quad (3.36)$$

where E is the multiplication of the number of stars and the total observational period in the unit [star×years]. By assuming that the length of our observation is 7 hours and the targeting field (patch=2,6) contains 1.4×10^5 stars, We can calculate the expected number of events as in the left panel of Fig. 3.29.

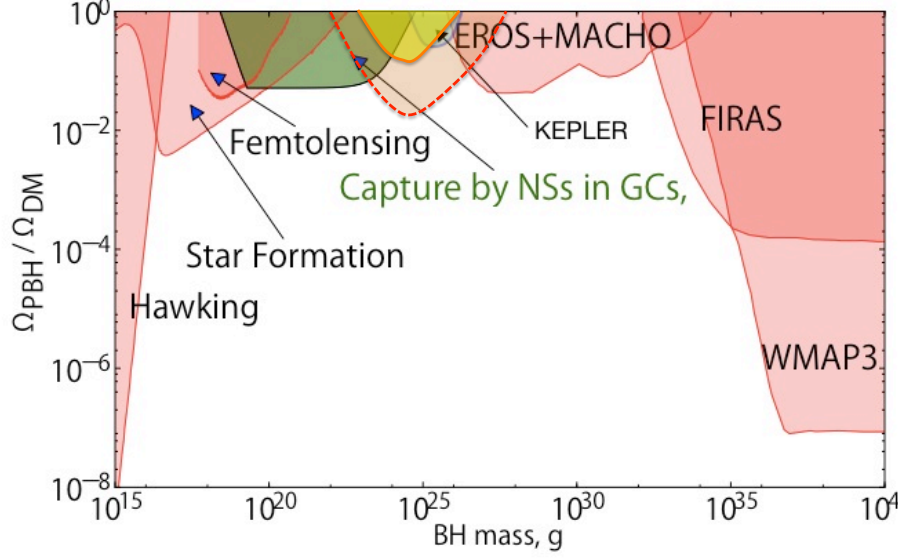


Figure 3.30: Summary of upper bound on the abundance of PBH, as its contribution to dark matter, in comparison with other constraints (Capela et al. 2013a). The orange line is the upper limit obtained from this thesis work using the 4 patch fields as used in Fig. 3.27. The red dashed line is the constraint if using all the data of M31 (very preliminary) and assuming no detection of PBH microlensing.

From this result we estimate the mass fraction of PBH to dark matter. Assuming that the event has Poisson distribution, the upper limit where less than one event happens in 95% confidential level is $N_{\text{exp}} < 3.7$. Then we can put upper limit on the dark matter fraction of PBHs in the total dark matter halo as:

$$f_{\text{lim}}(M) = \frac{3.7}{N_{\text{exp}}(M)} \quad (3.37)$$

Note that this upper limit holds whichever the lens body resides in the Milky Way halo or not. The current limit from four-patch fields from our analysis is presented in the right panel of Fig. 3.29. We also display the constraint expected from the whole field of view by the fact that total star counts from peak statics are 6, 843, 112.

3.5 Discussion and summary

In this work we discussed our tests of nature of dark matter on star scales, and searched dark matter candidate so-called primordial black hole (PBH). We make use of microlensing effect for the search which is expected when PBH comes in the line of sight of background stars. Microlensing effect is rare event; only one in million stars can happen. Thus we used the Hyper Suprime-Cam (HSC) images of Andromeda Galaxy (M31) on stars in M31 to gather large number of stars and achieve higher event rate. The PBH is one of viable candidates for dark matter, and we performed tests to establish a way to constrain the abundance of PBHs of mass scales, 10^{-9} - $10^{-7} M_{\odot}$, with the dense-cadence imaging data from wide-field camera. One large problem is that default analysis mode of HSC-pipe software could not reduce the images with large number of stars; which caused troubles as in background subtraction, star catalog construction, image difference, and event detection. Therefore we managed to establish the reduction method as described in § 3.2 and § 3.3, to extract transient candidates from the images.

From the reduced images we performed two kinds of analysis: transient study and microlensing implication. As for transient study we succeeded to extract as much as $\sim 11,000$ transient candidates. We draw light curves for all the events and classified them by peak characteristics, $g-r$ color and magnitude. These characteristics help us figure out unique candidates as well as noise properties. The summary of candidate characteristics is provided in § 3.3 and Appendix B and C. We also started the second analysis; estimating microlensing properties and implication expected from our data. Currently we could not find any microlensing candidates from the data by the fitting of theoretical microlensing light curve. Thus we started to estimate the upper limit of mass fraction of PBH to the total dark matter abundance implicated from our data. As our data covers large field of view, we need to take into account field-dependent properties such as star number counts and extinction. Therefore we divided the field of view into 10×10 sub-regions. In the first step we carefully looked into one single patch targeting region (patch=2,6) to reveal the position dependence, somehow succeeded to estimate the star number counts in the field. Our method constructed for one patch can be basically applied for wider field survey simply by considering position dependence and repeating the analysis. Also we make sure that our observation achieves strongest constraint on the mass fraction by simplified analysis.

This project is still ongoing, and we might need further investigation of microlensing property. Especially disk and bulge region we might need further correction for estimating the magnitude or number counts of stars, because peak counts might not work for these regions. Also for microlensing event from PBHs in M31 halo region, we need to estimate the event rate more carefully by taking into account so-called finite-source effects or limb-darkening effect, which might greatly affect event time-scale estimation (see Riffeser et al. 2008, for the detail).

The development achieved in our study can be applied to to future new time-space astronomy; aiming at faint, short-timescale events by wide-field or short-cadence survey. Currently several wide-field deep transient surveys are ongoing or planned not only by HSC, but also by the Palomar Transient Factory (PTF)³ and the Large Synoptic Survey Telescope (LSST)⁴. As for transient candidates, we can establish clear criteria to categorize the events like flares and binary stars including noise characteristics. Since our observation presents unique properties of faint, short-timescale variable candidates that has never been searched before, it would be helpful to characterize the time-dependent behavior of events in the future short cadence survey; as for microlensing study, event criteria can work as reference to remove contamination from microlensing candidates, for example.

³<http://www.ptf.caltech.edu/ipf>

⁴<http://www.lsst.org>

Chapter 4

Summary and Conclusion

In this thesis we explored properties of dark matter by using the gravitational lensing observables of Subaru data. To address this question we studied astronomical objects of totally different scales: massive clusters at Mpc scales and primordial black holes at 10^{-3} cm scale (the horizon scale for the formation of PBH with mass scales of 10^{25} g). Our finding is summarized as follows:

- *Part I: Universality test with weak lensing cluster profiles*

We developed a method of using the weak lensing measurements of massive clusters in order to test “universality” of the dark matter density profile that is as predicted by Navarro-Frenk-White (NFW) model, one of the most important predictions of the cold dark matter dominated structure formation scenario. The universality of NFW profile means that all the mass profiles for clusters of different masses can be transformed to a universal function if properly scaling the amplitude and radius for each mass profile.

To apply this method to real data, we combined the independent datasets for a volume-limited sample of 50 massive clusters that are the Subaru weak lensing catalog in Okabe et al. (2013) and their X-ray observables of *XMM* and/or *Chandra* satellites in Martino et al. (2014). We found a $4 - 6\sigma$ level evidence of the existence of universal NFW profile in the 50 massive clusters. To derive these results we have carefully studied a proper radial binning of the lensing distortion measurement and how to define the representative central value of each radial bin taking into account the cluster-centric distances and the lensing weights of background galaxies in the annulus. Our results give a proof of concept of the method we developed in this work.

We quantified the performance of the NFW scaling analysis by monitoring the scatters of 50 cluster distortion profiles relative to the NFW prediction. However, the improvement in the scatters of 50 cluster distortion profiles due to the NFW scaling analysis is not as much as expected from theory using simulations of cluster based on high-resolution N -body simulations. We elaborated that, in order to reconcile the difference between the measurements and the simulation expectation, we need to introduce additional halo mass scatters to each cluster, by an amount of $\sigma(M)/M \sim 0.2-0.3$. This implies intrinsic scatters in the halo mass and X-ray observable relation (Okabe et al. 2010b). We also argued that the discrepancy might be due to an imperfect halo mass proxy relation of the X-ray observables.

- *Part II: M31 transient survey*

PBH, which might have been formed in the early universe, is one of viable candidates of

dark matter. Here we used the dense cadence observation of M31 Galaxy (2 min cadence observation over about 7 hours) in order to search for microlensing events of PBH with mass scales of $10^{-9} - 10^{-7} M_{\odot}$, with the Hyper Suprime-Cam (HSC) data. The wide field-of-view of HSC allows us to cover the entire bulge and disk regions of M31 with one pointing and the 8.2m Subaru aperture allows us to measure a light curve of a star down to $r \sim 25\text{mag}$ even with 90sec exposure.

However, the PBH microlensing is in the pixel lensing regime; although multiple stars in M31 can be in a single CCD chip, only one source star can be amplified in its flux by gravitational lensing of a foreground PBH that is in halo regions of MW or M31. Thus the pixel lensing requires a careful analysis. Using the HSC pipeline, which has been developed for the HSC SSP program, we search for time-variable star candidates based on the image subtraction between the target and reference images. The current pipeline achieves a clean subtraction of most stars by taking into account the different PSFs of target and reference images, and illuminates candidates of time-variable point sources in the difference image. We then measure the light curve of each candidate based on the PSF photometry of the candidate in the difference image. We found about 11,000 transient candidates across the entire M31 region. These include secure candidates of star flare, binary stars, eclipse, variable stars, moving object, etc. However, at this moment, we haven't yet found a secure candidate of PBH microlensing event.

Employing the NFW profiles to reproduce the observed rotation curves of MW and M31, respectively, and assuming that all the dark matter in their halo regions is made of PBHs, we found that at least one star among 10^5 - 10^6 stars in M31 can be gravitationally lensed by a foreground PBHs. Since the HSC data allows us to detect 10^5 stars in each patch (about 100 arcmin²) region or there should be much more stars including unresolved fainter stars, a null detection of PBH microlensing in our data allows us to derive a stringent upper bound on the abundance of PBHs. We derived an upper bound such as $\Omega_{\text{PBH}}/\Omega_{DM} \sim 0.01$ for PBH of mass scales $10^{-8} M_{\odot}$.

Our studies can be easily extended to upcoming wide-area imaging surveys such as the HSC SSP Survey and the LSST Survey.

Acknowledgements

For these two years I received a lot of advices and helps from many people. Without their kind supports and helps I could not proceed the study and daily life.

First of all, I would like to express my gratitude to my supervisor, Professor Hiroaki Aihara, for his great support. He gave me a chance to work on these projects, and advised me a lot of on presentations which was always helpful.

I'm really grateful to Masahiro Takada, who always supports these projects and kindly discussed me a lot. He taught me from the basics of gravitational lensing and astrophysics, and introduced me the interesting research topics. He also read this manuscript and gave me useful comments.

As for weak lensing study I would like to thank my collaborators, Nobuhiro Okabe, Rossella Martino, and Ryuichi Takahashi for data, simulation and comments. I appreciate the kindness of the LoCuSS collaboration; they allowed us to study this topic with their data. I also express my thanks to Surhud More for helpful discussion and comments.

I also receive a lot of advice on the transient search project. I would like to give thanks to Takahiro Sumi, Robert Lupton, and Masaomi Tanaka for helpful discussion. I really appreciate their help to interpret the outcomes. Also Yoshiaki Ono, Song Huang and Ryoma Murata kindly provided me instructions for running fake pipeline, which was indispensable for estimating the properties of the imaging data. Especially I would like appreciate a lot to Naoki Yasuda, who always discussed on transient survey. Throughout my heavy reduction I made a lot of trouble with master server at IPMU, but he always repaired and presented me better options for data analysis.

I especially give thanks to Masashi Yokoyama, Yoshiyuki Onuki, Denis Epifanov and Kuniko Kono, who helped me a lot to lead my life at laboratory. Also I would like to appreciate the encouragements from all staffs, members and students at Aihara-Yokoyama lab, IPMU, and all of my friends. Without their supports I couldn't lead my comfortable student life. I also appreciate the kind comments from Toshinori Mori and Masami Ouchi for this thesis.

Last but not least, I would like to thank my family for all the kind supports they gave to me.

Appendix A

Deflection angle in the spherically symmetric gravitational field

In this section we describe the deflection angle in the spherically symmetric gravitational field, following the method of Futamase et al.(1995). Since the general relativity predicts the light path as Schwarzschild metric, we consider the following geodesic equation without perturbation:

$$ds^2 = 0 \iff 2K \equiv \left(1 - \frac{2m}{r}\right) \dot{t}^2 - \left(1 - \frac{2m}{r}\right)^{-1} \dot{r}^2 - r^2 \dot{\theta}^2 - r^2 \sin^2 \theta \dot{\phi}^2 = 0 \quad (\text{A.1})$$

where \cdot is the differential derivative with affine parameter s . We adopt the variational calculus method using the Euler-Lagrange equation:

$$\frac{\partial K}{\partial x^\alpha} - \frac{d}{ds} \left(\frac{\partial K}{\partial \dot{x}^\alpha} \right) = 0 \quad (\text{A.2})$$

where the four variable $x^0 = t(x)$, $x^1 = r(s)$, $x^2 = \theta(s)$, $x^3 = \phi(s)$. Combining $\alpha = 0, 2, 3$ cases with Eq. (A.1):

$$\alpha = 0: \quad \frac{d}{ds} \left(\left(1 - \frac{2m}{r}\right) \dot{t} \right) = 0 \quad (\text{A.3})$$

$$\alpha = 2: \quad \frac{d}{ds} (r^2 \dot{\theta}) - r^2 \sin \theta \cos \theta \dot{\phi}^2 = 0 \quad (\text{A.4})$$

$$\alpha = 3: \quad \frac{d}{ds} (r^2 \sin^2 \theta \dot{\phi}) = 0 \quad (\text{A.5})$$

Here we consider the motion in the $\theta = \pi/2$ plane. If $\dot{\theta} = 0$ holds in this plane, the motion is within this plane because $\ddot{\theta} = 0$, and higher-order derivative also becomes zero from Eq. (A.4). Integrating Eq. (A.5) makes preservation of angular momentum equation,

$$r^2 \dot{\phi} = h \quad (\text{A.6})$$

where h is constant. Similarly integrating Eq. (A.3) makes:

$$\left(1 - \frac{2m}{r}\right) \dot{t} = k \quad (\text{A.7})$$

where k is constant. Putting this equation into Eq. (A.1) becomes:

$$\left(1 - \frac{2m}{r}\right)^{-1} k^2 - \left(1 - \frac{2m}{r}\right)^{-1} \dot{r}^2 - r^2 \dot{\phi}^2 = 0 \quad (\text{A.8})$$

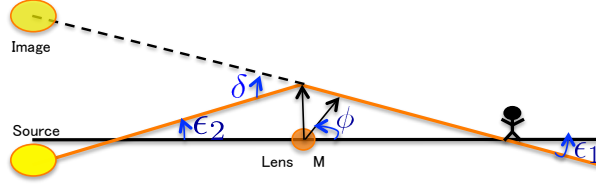


Figure A.1: A simple schematic representation of gravitational lensing effect describing the deflection of light path around massive object.

Also r in Eq. (A.6) can be transform by $u = 1/r$ as:

$$\dot{r} = \frac{d}{ds} \left(\frac{1}{u} \right) = -\frac{1}{u^2} \dot{u} = -\frac{1}{u^2} \frac{du}{d\phi} \dot{\phi} = -h \frac{du}{d\phi} \quad (\text{A.9})$$

Putting Eq. (A.6) and Eq. (A.8) into Eq. (A.9)

$$\left(\frac{du}{d\phi} \right)^2 + u^2 = \frac{k^2}{h^2} + 2mu^3 \quad (\text{A.10})$$

Then differentiating this equation with ϕ describes a light path projected to a $t = \text{const.}$ plane,

$$\frac{d^2u}{d\phi^2} + u = 3mu^2 \quad (\text{A.11})$$

Since $m = 0$ holds in the limit of the special relativity theory, the general solution can be described as:

$$u = \frac{1}{l} \sin(\phi - \phi_0) \quad (\text{A.12})$$

This solution has the same form with Newtonian prediction, which expresses the straight line from ϕ_0 to $\phi_0 + \pi$ where $l = \text{const.}$ Thus the light path in the Schwarzschild metric can be considered as the perturbed form of the special case. Then the solution of Eq. (A.11) can be written as

$$u = u_0 + 3mu_1, \quad (\text{A.13})$$

where u_0 is Eq. (A.12) in the limit that mu is small enough, and $\phi_0 = 0$. Putting Eq. (A.13) into Eq. (A.11) and neglect terms with higher-order than (mu) ,

$$\frac{d^2u_1}{d\phi^2} + u_1 = u_0^2 = \frac{\sin^2\phi}{l^2} \quad (\text{A.14})$$

Therefore, general solution of Eq. (A.11) is:

$$u = \frac{\sin\phi}{l} + \frac{m(1 + C\cos\phi + \cos^2\phi)}{l^2} \quad (\text{A.15})$$

where m/l is small.

Next we move on to decide deflection angle δ in spherically symmetric gravitational field, considering the case where $r \rightarrow \text{inf}$, which means $u \rightarrow 0$ so the right side of Eq. (A.15) is zero,

then the asymptote angles are $-\epsilon_1$ and $\pi + \epsilon_2$ as shown in the figure. In the limit of $\epsilon_1, \epsilon_2 \rightarrow 0$, Eq. (A.15) shows

$$\begin{aligned} -\frac{\epsilon_1}{l} + \frac{m(2+C)}{l^2} &= 0 \\ -\frac{\epsilon_2}{l} + \frac{m(2+C)}{l^2} &= 0 \end{aligned}$$

$$\therefore \delta = \epsilon_1 + \epsilon_2 = \frac{4m}{l} \tag{A.16}$$

If we explicitly write the gravitational constant G and light velocity c , the deflection angle can be written as:

$$\delta = \frac{4Gm}{c^2 l} \tag{A.17}$$

Appendix B

Effects from non-celestial moving bodies

Short-cadence transient survey can be suffered from non-celestial causes from telescope or CCD properties. In this section we summarize the possible properties suggested from our results.

- Defraction spikes

There are around 80 events with some sharp peaks in the light curves, which are not correlated with the time-variation of seeing. For these events many spiky patterns show up as in Fig. B.1, especially around nearby bright stars. These spikes are artificial noise of telescope, caused by the change of the targeting direction in the sky. The patterns turn clockwise around a star as the observation goes on, and magnify the surrounding stars when the spikes pass by.

- CCD edge

In this HSC-M31 study we fixed the observational field of view by automatic tracking system of the telescope so as to reduce the coordinate uncertainty in image difference technique. However, there exists small movement due to the uncertainty of the tracking system as displayed in the lower left panel of Fig. B.2. Therefore electrostatic effects near the edge of CCDs (a few pixels for our Hamamatsu CCDs) cause incorrect photometry, which induces magnification of flux for nearby objects as in the upper left panel. Around a few hundred stars close to CCD edges are detected as candidates in our observation.

- CCD defect

There also exist around 30 cases where small defected parts of CCD are detected as transient candidates. As CCD defects cannot give correct flux measurement, they sometimes produces small bright region in difference images, which are detected as time-variant candidates.

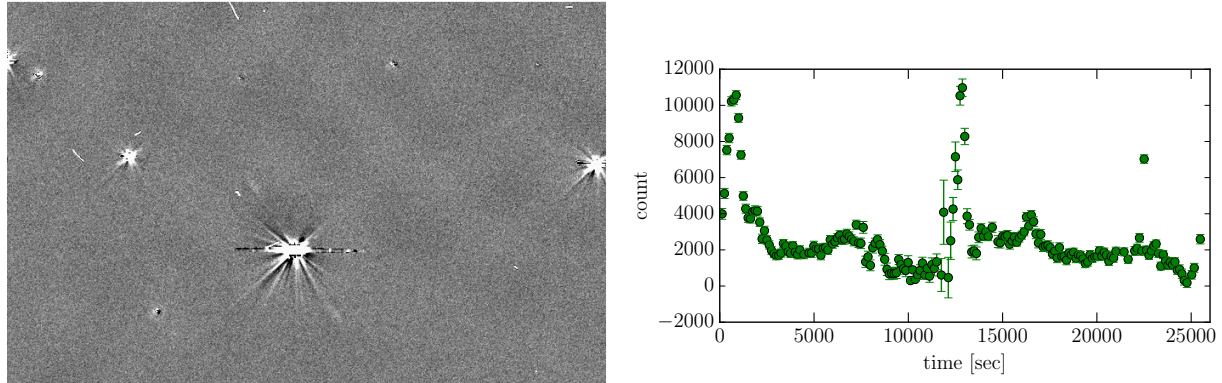


Figure B.1: The effect from diffraction spikes. Left panel shows one part of difference image containing spike patterns. Spikes are often seen in brighter stars, and the patterns turn clockwise during the observation. Right panel displays an example of light curve affected by spikes of a nearby star. Peak around ~ 13000 sec is caused by a spike.

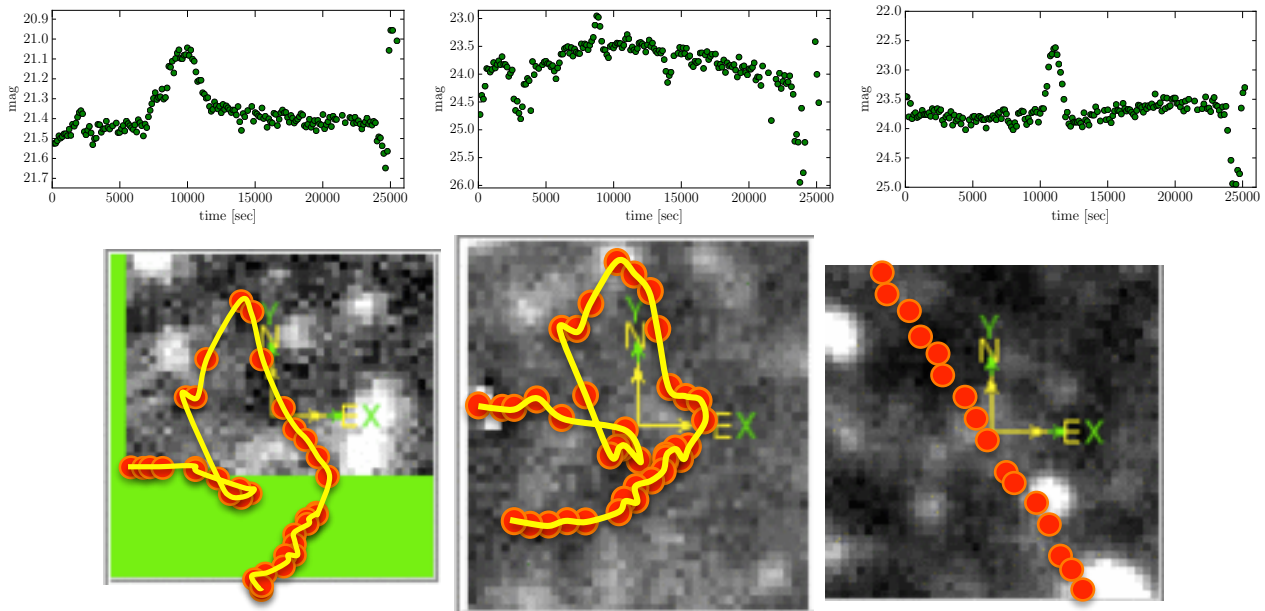


Figure B.2: Examples of moving candidates; Left panel shows an example of CCD-edge move during HSC-M31 observation. The green region corresponds to region outside a CCD chip, and red circle draws the trace of the edge. Middle panel displays one example of light curve affected by CCD defects. Peak around ~ 9000 sec is caused by the defect part. Right panel shows one example of moving candidate of celestial object. Unlike the other two images this object draws a straight motion path.

Appendix C

Characteristics of unique events

In this section we describe some detailed properties of unique candidates.

C.1 Eclipsing binary stars: white - brown dwarf system

Among the eclipsing binaries we found a unique candidate; as shown in Fig. C.1, one dark star totally hide the other star so that the flux becomes totally dark. This system is considered to be composed by a white dwarf and a brown dwarf.

C.2 A star before nova

A red nova was found on February 2015, about three months after our observation. Therefore the candidate might be at the stage of merging of two stars. Fig. C.2 shows the light curve and image of the target star, at 00h 42m 07.99s +40d 55m 01.1s in radec coordinate which is close to M31 bulge. This object is not detected with our selection criteria probably due to small change of flux. The magnification is only 0.02 mag during our observation, which is so small that we cannot say clearly if this is true.

C.3 Appearing star or disappearing star

There are around 10 stars which suddenly appear or disappear during observation without the effect from CCD edge. We could not find out the reason so far, but many of them reside close to the bulge region.

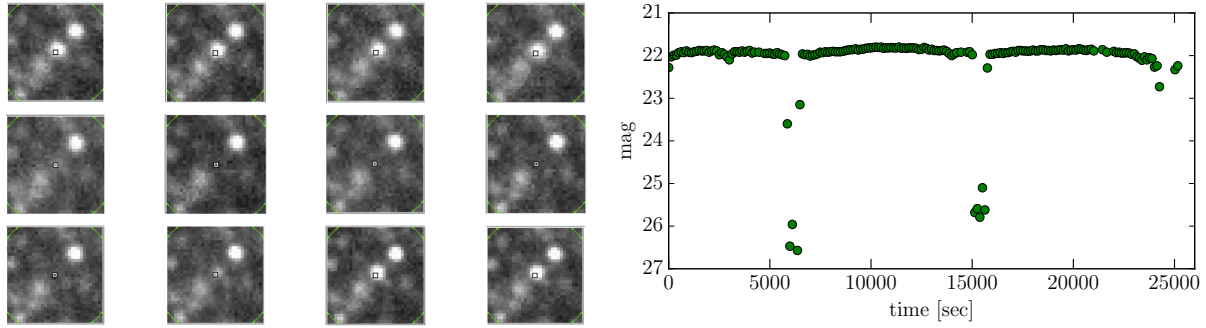


Figure C.1: Eclipsing binary stars consisted of a white dwarf (WD) and a brown dwarf (BD). Left panel displays pictures of WD-BD system; showing time variation from left to right. Right panel gives the light curve of the same eclipsing-binary system, containing very deep dips with length around 10 minutes.

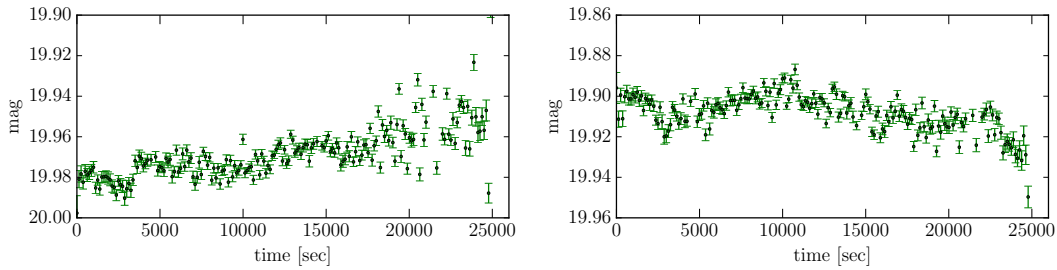


Figure C.2: Left figure shows the light curve of nova candidate which contains very faint magnification. For comparison, right figure shows a typical example of light curve for a star without magnification.

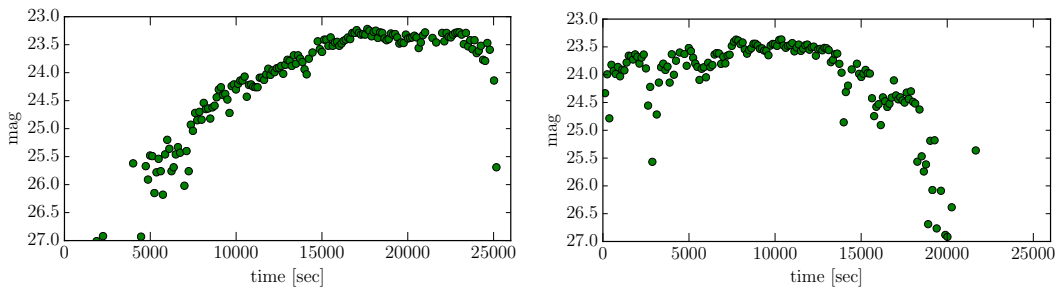


Figure C.3: Light curves for appearing and disappearing stars.

C.4 Eclipsing binary

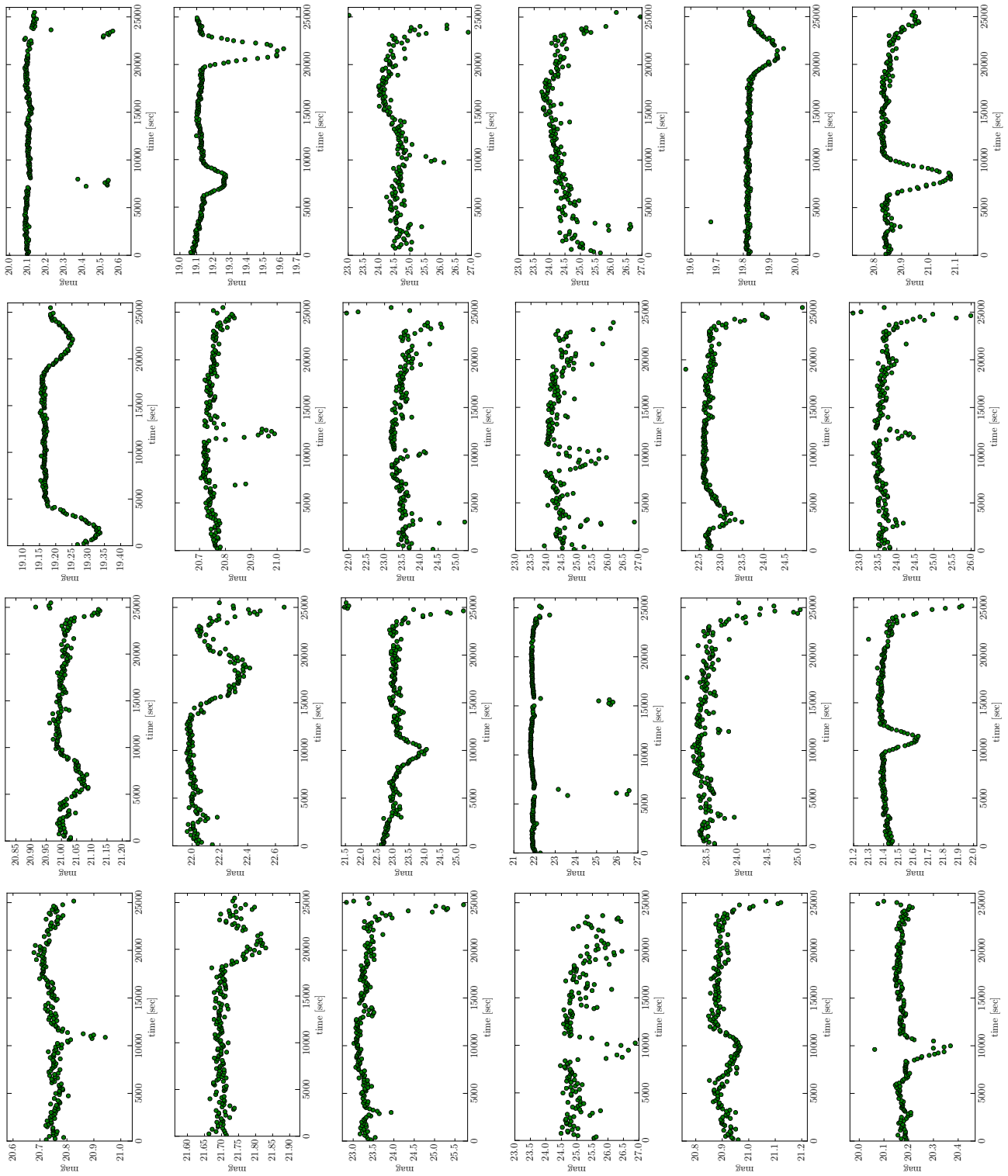


Figure C.4: Light curves of eclipsing binary-star candidates.

C.5 Binary stars

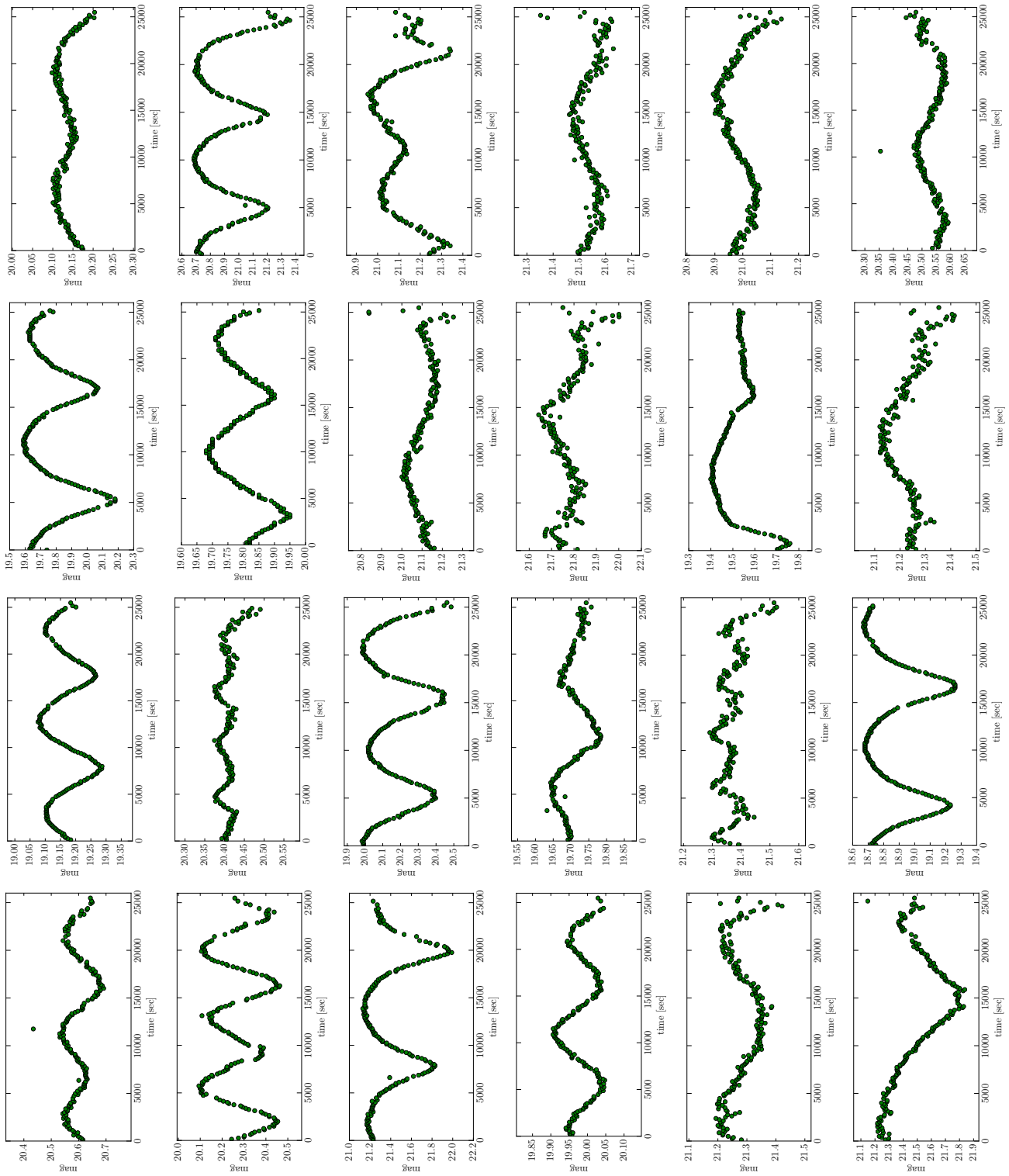


Figure C.5: Light curves of binary-star candidates.

C.6 Cepheid candidates

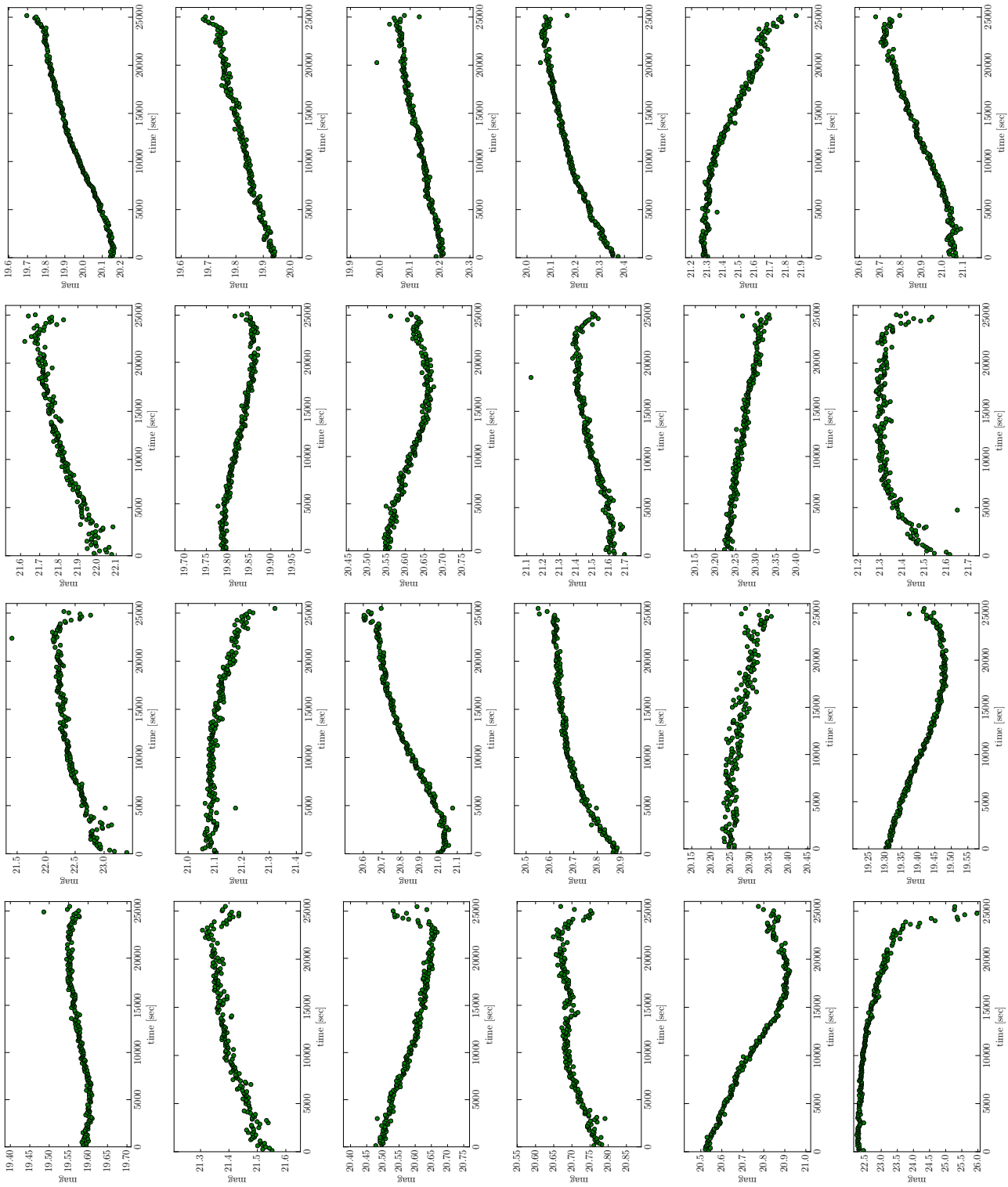


Figure C.6: Light curves of cepheid variable-star candidates.

C.7 Flares

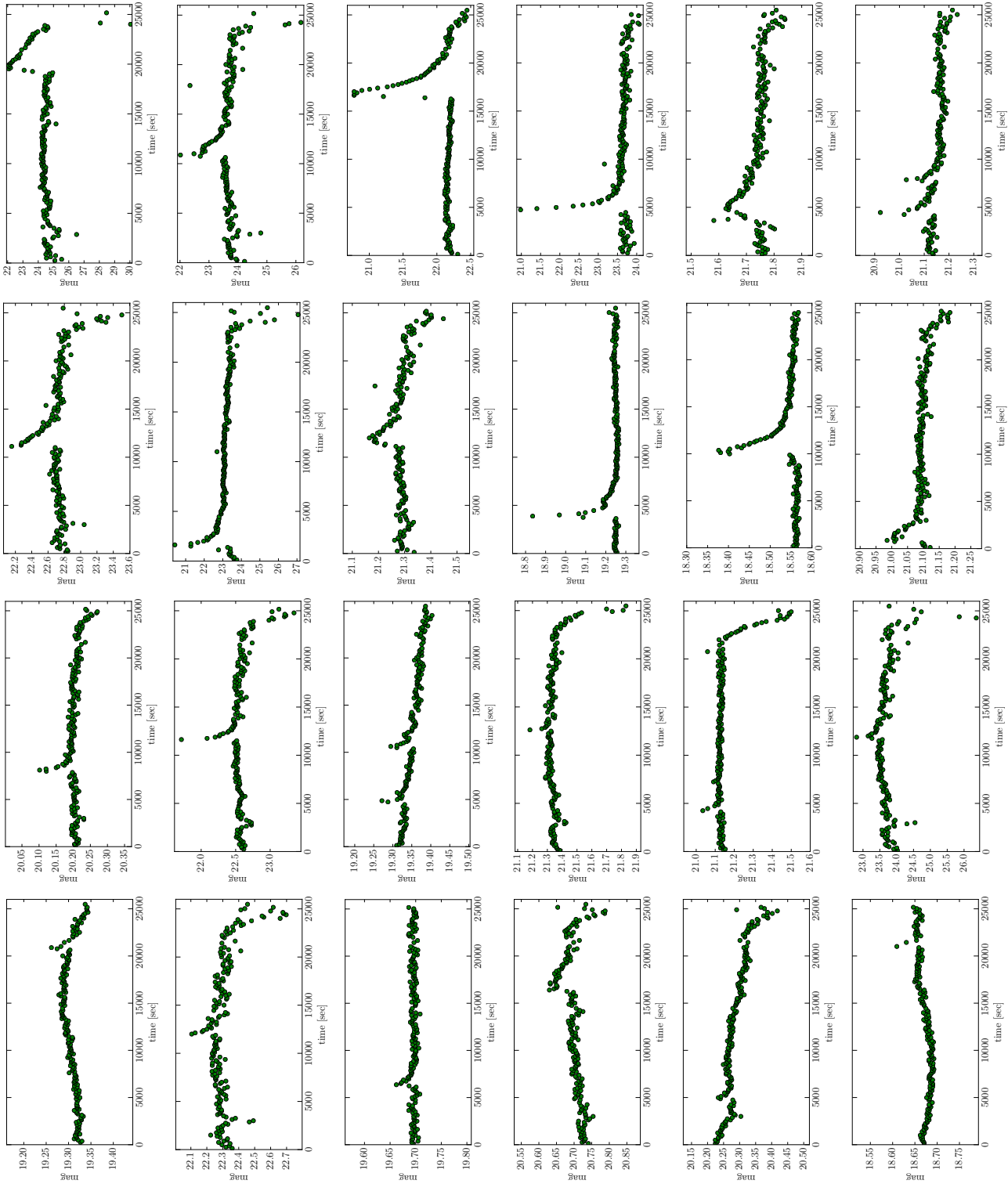


Figure C.7: Light curves of flare-star candidates.

C.8 Fake events with common light curves

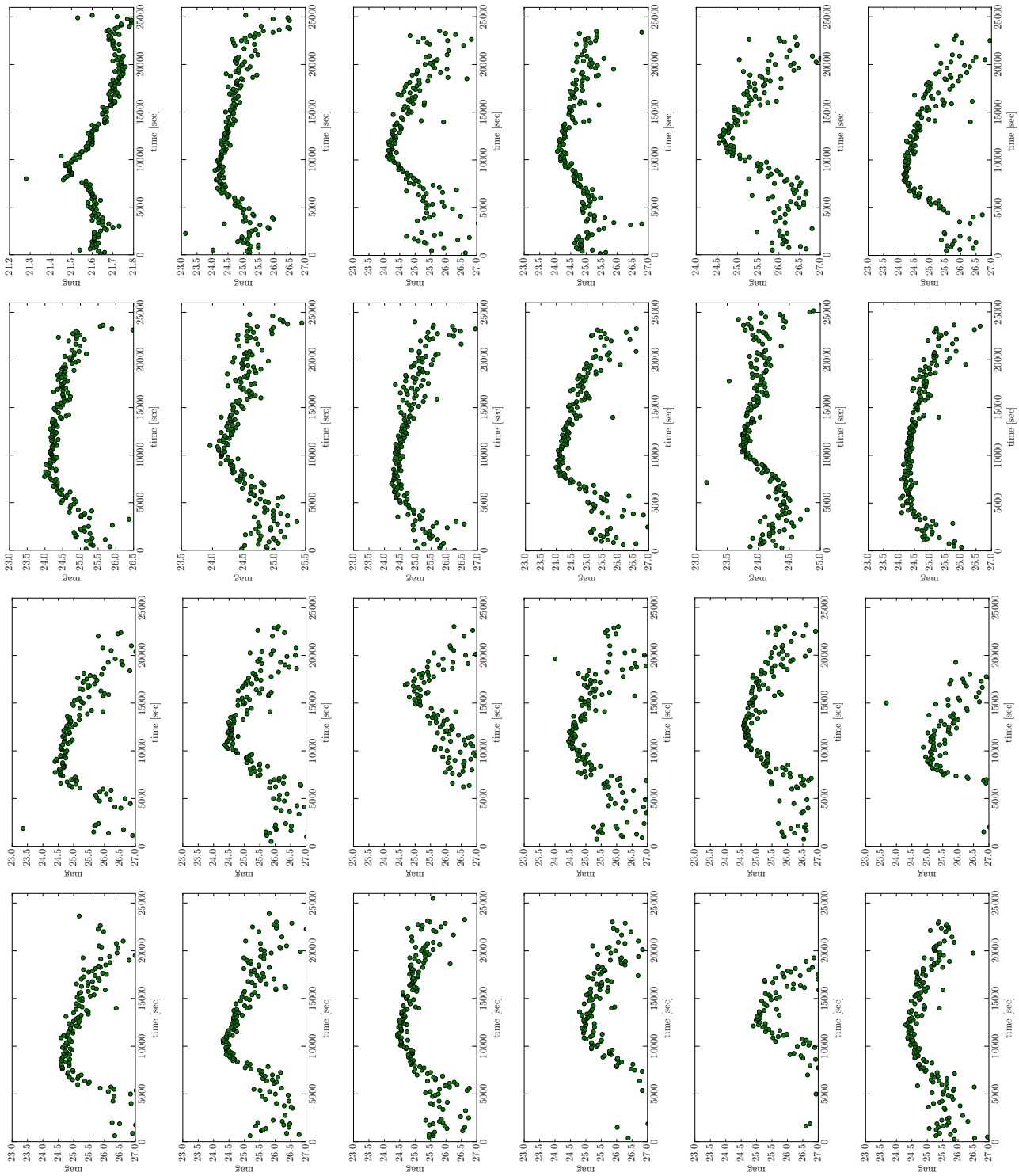


Figure C.8: Light curves of fake candidates which might contain RR-Lyrae variables.

Appendix D

Other constraints on the abundance of primordial black hole (PBH)

As shown in Fig. 3.30, the abundance of PBH is constrained for various mass range. In this section we overview these current constraints on PBH abundance other than HSC-M31 observation.

D.1 Hawking radiation

Primordial black hole (PBH) emits Hawking radiation at a rate inversely proportional to their mass, which encourages PBHs to evaporate (Hawking 1974). Thus the life time of PBH in mass range of $m_{\text{BH}} < 5 \times 10^{14} \text{g}$ is shorter than the age of the universe, and cannot exist as a candidate of dark matter today (Page & Hawking 1976). On the other hand, PBHs slightly heavier than this mass limit are expected to emit γ -ray around 100MeV. Thus the observation of from extra galactic γ -ray background can constrain the cosmic density of PBH. Current constraint is achieved from the Energetic Gamma Ray Experiment Telescope (EGRET) as $\Omega_{\text{PBH}} \leq 10^{-9}$ for $m_{\text{BH}} = 10^{15} \text{g}$ (Sreekumar et al. 1998; Carr et al. 2010). In summary, PBH of $m_{\text{BH}} \leq 10^{16} \text{g}$ cannot constitute dark matter more than 1%, and that of $m_{\text{BH}} \geq 7 \times 10^{16} \text{g}$ disappears due to Hawking radiation.

D.2 Femtolensing

Femtolensing is a type of gravitational lensing effect caused by PBH, named after the very small separation of lens images. As Schwarzschild radius of PBH is as large as the wavelength of photons, one needs to consider radiative electromagnetic properties in femtolensing regime, where interference patterns are expected to show up in the energy power spectrum of the lensed object. Therefore the abundance of PBHs can be constrained by the event rate of femtolensing effect, in the same way as we adopt for microlensing study. The current constraint described in Fig. 3.30 is derived from the search of femtolensing by compact objects, sensitive to PBH of $m_{\text{BH}} \geq 10^{19} - 10^{20} \text{g}$ by combing the Fermi satellite GRB data and redshift data (Barnacka et al. 2012).

D.3 Star formation

Dark matter is trapped by stars due to the adiabatic contraction during their star-formation epoch. If PBHs exist as kind of dark matter, they are also trapped by compact stars such as

white dwarf or neutron stars. As the matter accretion rate to PBH is expected to be very fast, compact stars including PBHs are in fate be destroyed (Kouvaris & Tinyakov 2011a; Kouvaris 2012; Kouvaris & Tinyakov 2011b). Therefore the capture process of PBH needs to be very small for the star remnant compacts, stars after the phase of white dwarf, to be observed up to data. The constraint of PBH abundance here is derived from the observation of globular clusters, where the density of dark matter is relatively high and have small velocity. By considering the scenario of destruction, the amount of PBH with typical mass is constrained by the dark matter distribution during the formation epoch of globular cluster; represented by the current number of compact stars. Thus one can put constraint on the abundance of PBHs as shown in Fig. 3.30 (Capela et al. 2013a).

D.4 Neutron stars in globular cluster

One can also apply the star formation scenario above for the current abundance of dark matter in globular clusters. As in the same scenario as described in D.3, the current amount of PBHs in compact objects is expected to be small enough to avoid the capture process. Strong constraint can be achieved in the dense core of globular clusters by comparing the direct capture mechanism of neutron stars with the corresponding numerical simulation. Fig. 3.30 shows constraint from Capela et al. (2013b), sensitive to PBH mass range of $3 \times 10^{18} \text{g} \leq m_{\text{BH}} \leq 10^{24} \text{g}$. On the other hand, the dark matter density derived from the model indicates that PBH for this mass range is less than 5%.

D.5 CMB (WMAP3, FIRAS)

Evaporation process due to Hawking radiation of PBH is expected to affect the signal from cosmic microwave background radiation. The distortion of spectrum can be described by chemical potential μ and Compton parameter y . By combining these parameters with the peak formation theory about the mechanism of PBH formation, one can put constraint on the power index of primordial perturbation n and PBH mass fraction β ; the index of primordial perturbation is constrained from the threshold amplitude of peaks to become PBHs, while the mass fraction can be calculated from the implication of density perturbation. The constraint displayed in Fig. 3.30 is given by WMAP3 and FIRAS experiment respectively (Tashiro & Suyama 2008; Carr et al. 2010).

D.6 Microlensing (MACHO, EROS, Kepler)

Two representative microlensing projects which have put constraint on the mass fraction of PBH are the EROS + MACHO collaboration and the Kepler mission (Alcock et al. 1998; Tisserand et al. 2006; Griest et al. 2014). They put constraint on the abundance of PBHs from the null detection of microlensing events of PBHs, in the same way as our observation adopts. The strongest constraint comes from the MACHO project, where they search for microlensing events with timescale longer than a few days in the Large Magellanic Cloud. The mission of Kepler satellite, on the other hand, targets at events with a-few-hour timescale in the Cygnus-Lyra region which have sensitivity to PBH DM in the mass range of $10^{-9} M_{\odot}$ to $10^{-7} M_{\odot}$. The Kepler mission and our HSC-M31 observation targets at PBH with similar mass range, but each has

different advantages; the comparison of Kepler and HSC mission indicates that the Kepler mission has large advantages on precise photometry, larger field-of-view and longer time-allocation. On the other hand, HSC-M31 observation is expected to be more competitive owing to the larger number of field stars in M31 and a larger coverage of 3D volume, or a more number of PBHs in the volume.

References

- Adhikari, S., Dalal, N. & Chamberlain, R. T. 2014, JCAP, 11, 19
- Alard, C., Lupton, R.H. 1998, ApJ, 503, 325
- Alcock, C. et al., 1998, ApJ, 499, 1
- Alcock, C. et al. (The MACHO Collaboration), 2000, ApJ, 542, 281
- Alcock, C. et al. (The MACHO Collaboration) 2001, ApJ, 550, 169
- Baltz, E.A., & Silk, J. ApJ, 530, 578
- Barnacka, A., Glicenstein, J.-F., & Moderski, R. 2012, Phys.Rev. D86, 043001
- Bartelmann, M. 1996, A&A, 313, 697
- Bartelmann, M. & Schneider, P. 2001, Physics Reports, 340, 291
- Becker, M. R. & Kravtsov, A. V. 2011, ApJ, 740, 25
- Bhattacharya, S., Habib, S., Heitmann, K. & Vikhlinin, A. 2013, ApJ, 766, 32
- Böhringer, H., et al. 2004, A&A, 425, 367
- Broadhurst, T., Takada, M., Umetsu, K., Kong, X., Arimoto, N., Chiba, M. & Futamase, T. 2005, ApJ, 619, L143
- Bullock, J. S., Kolatt, T. S., Sigad, Y., Somerville, R. S., Kravtsov, A. V., Klypin, A. A., Primack, J. R., & Dekel, A. 2001, MNRAS, 321, 559
- Caldwell, J. A. R., & Coulson, I. M.. 1986, MNRAS, 218, 223
- Capela, F., Pshirkov, M. & Tinyakov, P. 2013, Phys.Rev. D87, 023507
- Capela, F., Pshirkov, M. & Tinyakov, P. 2013, Phys.Rev. D87, 123524
- Carr, B., Kohri, K., Sendouda, Y., & Yokoyama, J. 2010, Phys.Rev. D81, 104019
- Clowe, D., Bradač, M., Gonzalez, A. H., Markevitch, M., Randall, S. W., Jones, C. & Zaritsky, D. 2006, ApJ, 648, L109
- Cusano, F., Garofalo, A., Clementini, G., Cignoni, M., Federici, L., Marconi, M., Musella, I., Ripepi, V., Speziali, R., Sani, E. & Merighi, R. 2015, ApJ, 806, 200
- Dalal, N., Lithwick, Y., & Kuhlen, M. 2010, ArXiv e-prints:1010.2539

Davis, M., Efstathiou, G., Frenk, C. S. & White, S. D. M. 1985, *ApJ*, 292, 371

de Jong, J.T.A. et al. (The MEGA collaboration) 2006, *A&A*, 446, 855

Demers, S., Battinelli, P., & Letarte, B., 2003, *AJ*, 125, 3037

Diemer, B. & Kravtsov, A. V. 2014a, *ArXiv e-prints:1407.4730* (DK14)

. 2014b, *ApJ*, 789, 1

Dodelson, S., “Modern Cosmology” 2003, Academic. Press

Duffy, A. R., Schaye, J., Kay, S. T., & Dalla Vecchia, C. 2008, *MNRAS*, 390, L64

Ebeling, H., Edge, A. C., Allen, S. W., Crawford, C. S., Fabian, A. C. & Huchra, J. P. 2000, *MNRAS*, 318, 333

Ebeling, H., Edge, A. C., Bohringer, H., Allen, S. W., Crawford, C. S., Fabian, A. C., Voges, W. & Huchra, J. P. 1998, *MNRAS*, 301, 881

Geehan, J. J., Fardal, M. A., Babul, A. & Guhathakurta, P. 2006, *MNRAS*, 366, 996

Golse, G. & Kneib, J.-P. 2002, *A&A*, 390, 821

Gondolo, P. 1999, *ApJ*, 510, 29

Gould, A., 1996, *ApJ*, 470, 201G

Griest, K., et al. (The MACHO Collaboration) 1991, *ApJ*, 372, 79

Griest, K., Cieplak, A.M. & Lehner, M J. 2014, *ApJ*, 786, 158

Hawking, S. 1974, *Nature* 248, 30.

Henry G. W. & Newsom M. S., 1996, *PASP*, 108, 242

Hu, W. & Kravtsov, A. V. 2003, *ApJ*, 584, 702

Johnston, D. E., et al. 2007, *ArXiv e-prints:0709.1159*

Kaiser, N. 1986, *MNRAS*, 222, 323

Klypin, A., Zhao, H., & Somerville, R S. 2002, *ApJ*, 573, 597K

Kneib, J.-P. et al. 2003, *ApJ*, 598, 804

Kodric, M. et al. 2013, *AJ*, 145, 106

Kouvaris, C. & Tinyakov, P. 2011, *Phys.Rev.Lett.* 107, 091301

Kouvaris, C., *Phys.Rev.Lett.* 2012, 108, 191301

Kouvaris, C., & Tinyakov, P. 2011, *Phys.Rev.* D83, 083512

Kurucz, R. 1993, CD-ROM No.13 (Cambridge, Mass.: Smithsonian Astrophysical Observatory),

- Lacy C. H., Moffett T. J. & Evans D. S., 1976, *ApJS*, 30, 85
- Leauthaud, A., et al. 2010, *ApJ*, 709, 97
- Mahdavi, A., Hoekstra, H., Babul, A., Bildfell, C., Jeltema, T. & Henry, J. P. 2013, *ApJ*, 767, 116
- Mamon, G. A., & Soneira, R. M. 1982, *ApJ*, 255, 181
- Mandelbaum, R., Slosar, A., Baldauf, T., Seljak, U., Hirata, C. M., Nakajima, R., Reyes, R. & Smith, R. E. 2013, *MNRAS*, 432, 1544
- Mandelbaum, R., Tasitsiomi, A., Seljak, U., Kravtsov, A. V. & Wechsler, R. H. 2005, *MNRAS*, 362, 1451
- Martino, R., Mazzotta, P., Bourdin, H., Smith, G. P., Bartalucci, I., Marrone, D. P., Finoguenov, A. & Okabe, N. 2014, *MNRAS*, 443, 2342
- Masaki, S., Hikage, C., Takada, M., Spergel, D. N. & Sugiyama, N. 2013, *MNRAS*, 433, 3506
- Meneghetti, M., Rasia, E., Merten, J., Bellagamba, F., Ettori, S., Mazzotta, P., Dolag, K. & Marri, S. 2010, *A&A*, 514, A93
- Meneghetti, M., et al. 2014, ArXiv e-prints:1404.1384
- Merten, J., et al. 2014, ArXiv e-prints:1404.1376
- Miyatake, H., et al. 2013, ArXiv e-prints:1311.1480
- Miyatake, H., More, S., Takada, M., Spergel, D. N., Mandelbaum, R., Rykoff, E. S. & Rozo, E. 2015, ArXiv e-prints: 1506.06135
- Miyazaki, S., et al. 2002, *PASJ*, 54, 833
- Mo, H., van den Bosch, F. & White, S. “Galaxy Formation and Evolution” 2010, Cambridge University Press
- Moffett T. J., 1974, *ApJS*, 29, 1
- Niikura, H., Takada, M., Okabe, N., Martino, R. & Takahashi, R. 2015, ArXiv e-prints:1504.01413
- Navarro, J. F., Frenk, C. S., & White, S. D. M. 1996, *ApJ*, 462, 563
- . 1997, *ApJ*, 490, 493
- Navarro, J. F., et al. 2004, *MNRAS*, 349, 1039
- Nesti, F. & Salucci, P. 2013, *JCAP*, 07, 016
- Newman, A. B., Treu, T., Ellis, R. S., Sand, D. J., Nipoti, C., Richard, J. & Jullo, E. 2013, *ApJ*, 765, 24
- Okabe, N., Smith, G. P., Umetsu, K., Takada, M., & Futamase, T. 2013, *ApJ*, 769, L35

- Okabe, N., Takada, M., Umetsu, K., Futamase, T. & Smith, G. P. 2010a, PASJ, 62, 811
- Okabe, N., Zhang, Y.-Y., Finoguenov, A., Takada, M., Smith, G. P., Umetsu, K. & Futamase, T. 2010b, ApJ, 721, 875
- Okabe, N., et al. 2014, PASJ, 66, 99
- Oguri, M., Bayliss, M. B., Dahle, H., Sharon, K., Gladders, M. D., Natarajan, P., Hennawi, J. F. & Koester, B. P. 2012, MNRAS, 420, 3213 title = "Combined strong and weak lensing analysis of 28 clusters from the Sloan Giant Arcs Survey",
- Oguri, M., & Takada, M. 2011, Phys. Rev. D, 83, 023008
- Oguri, M., Takada, M., Umetsu, K. & Broadhurst, T. 2005, ApJ, 632, 841
- Oguri, M. & Hamana, T. 2011, MNRAS, 414, 1851
- Oguri, M. 2002, Master thesis, "Resolving the Central Density Profile of Dark Matter Halos with Gravitational Lensing Statics",
- Oguri, M. 2004, Doctor thesis, "Strong Gravitational Lenses in a Cold Dark Matter Universe",
- O 'Meara, J. M., Tytler, D., Kirkman, D., Suzuki, N., Prochaska, J. X., Lubin, D. & Wolfe. A. M. 2001 ApJ, 552, 718
- Paczynski, B. 1986, ApJ, 304, 1
- Paczynski, B., Udalski, A., Szymanski, M., Kubiak, M., Pietrzynski, G., Soszynski, I., Wozniak, P. & Zebrun, K., 1999, Acta Astronomica, 49, 319
- Page, D. N. & Hawking, S. 1976, ApJ, 206, 1 .
- Penzias, A. A., & Wilson, R. W. ApJ, 142, 419
- Perlmutter, S. et al. (The Supernova Cosmology Project)
- Planck Collaboration et al. 2015, ArXiv e-prints
- Power, C., Navarro, J. F., Jenkins, A., Frenk, C. S., White, S. D. M., Springel, V., Stadel, J. & Quinn, T. 2003, MNRAS, 338, 14
- Riess, A. G. et al. Astronomical Journal, 1998, 116,1009
- Riffeser, A., Fliri, J., Seitz, S., & Bender, R. 2006, ApJS, 163, 225
- Riffeser, A., Seitz, S., & Bender, R. 2008, ApJ, 684, 1093
- Rozo, E., et al. 2009, ApJ, 699, 768
- . 2010, ApJ, 708, 645
- Schneider, P. 1996, IAUS, 168, 209

- Schneider, P. 2006, in Saas-Fee Advanced Course 33: Gravitational Lensing: Strong, Weak and Micro, ed. G. Meylan, P. Jetzer, P. North, P. Schneider, C. S. Kochanek, & J. Wambsganss, 1–89
- Mandelbaum, R., Hirata, C. M., Leauthaud, A., Massey, R. J. & Rhodes, J. 2011, SHERA: SHEar Reconvolution Analysis, Astrophysics Source Code Library
- Seitz, S. & Schneider, P. 1996, *A&A*, 305, 383
- Schneider, P., Ehlers, J. & Falco, E.E., 1992. Gravitational Lenses. Springer, Heidelberg.
- Smith, G. P., Kneib, J.-P., Smail, I., Mazzotta, P., Ebeling, H. & Czoske, O. 2005, *MNRAS*, 359, 417
- Smoot, G. F., Bennett, C. L., Kogut, A., Wright, E. L., Aymon, J., Boggess, N. W., Cheng, E. S., de Amici, G., Gulkis, S., Hauser, M. G., Hinshaw, G., Jackson, P. D., Janssen, M., Kaita, E., Kelsall, T., Keegstra, P., Lineweaver, C., Loewenstein, K., Lubin, P.; Mather, J., Meyer, S. S., Moseley, S. H., Murdock, T., Rokke, L., Silverberg, R. F., Tenorio, L., Weiss, R. & Wilkinson, D. T. *ApJ*, 1992, 396
- Springel, V. 2005, *MNRAS*, 364, 1105
- Springel, V., Yoshida, N. & White, S. D. M. 2001, *New Astron.*, 6, 79
- Sreekumar, P. et al. (EGRET Collaboration), 1998, *ApJ*, 494, 523
- Stanek, R., Rasia, E., Evrard, A. E., Pearce, F. & Gazzola, L. 2010, *ApJ*, 715, 1508
- Sumi, T., et al. 2003, *ApJ*, 591, 204
- Takada, M. & Jain, B. 2002, *MNRAS*, 340, 580
- Takada, M. & Spergel, D. N. 2014, *MNRAS*, 441, 2456
- Takahashi, R., Sato, M., Nishimichi, T., Taruya, A. & Oguri, M. 2012, *ApJ*, 761, 152
- Tashiro, H. & Sugiyama, N. 2008, *Phys.Rev. D*78, 023004
- P.Tisserand, et al. 2004, *A&A*, 424, 245
- Tyson, J. A. & Fischer, P. 1995, *ApJ*, 446, L55
- Umetsu, K., et al. 2014, ArXiv e-prints:1404.1375
- van den Bosch, F. C., More, S., Cacciato, M., Mo, H. & Yang, X. 2013, *MNRAS*, 430, 725
- von der Linden, A., et al. 2014, *MNRAS*, 439, 2
- Vikhlinin, A., et al. 2009, *ApJ*, 692, 1060
- Walsh, D., Carswell, R. F. & Weymann, R. J. 1979, *Nature*, 279, 381
- Walterbos, R. A. M. & Kennicutt, R. C., 1988, *A&A*, 198, 61

- Wechsler, R. H., Bullock, J. S., Primack, J. R., Kravtsov, A. V., & Dekel, A. 2002, *ApJ*, 568, 52
- Zhang, Y.-Y., et al. 2010, *ApJ*, 711, 1033
- Zhang, Y.-Y., Finoguenov, A., Böhringer, H., Kneib, J.-P., Smith, G. P., Kneissl, R., Okabe, N. & Dahle, H. 2011, *A&A*, 527, C3
- Zhao, D. H., Jing, Y. P., Mo, H. J., & Börner, G. 2009, *ApJ*, 707, 354
- Zhao, D. H., Mo, H. J., Jing, Y. P., & Börner, G. 2003, *MNRAS*, 339, 12
- Zitrin, A., et al. 2014, *ArXiv e-prints*:1411.1414
- Zwicky, F. 1937, *ApJ*, 86, 217